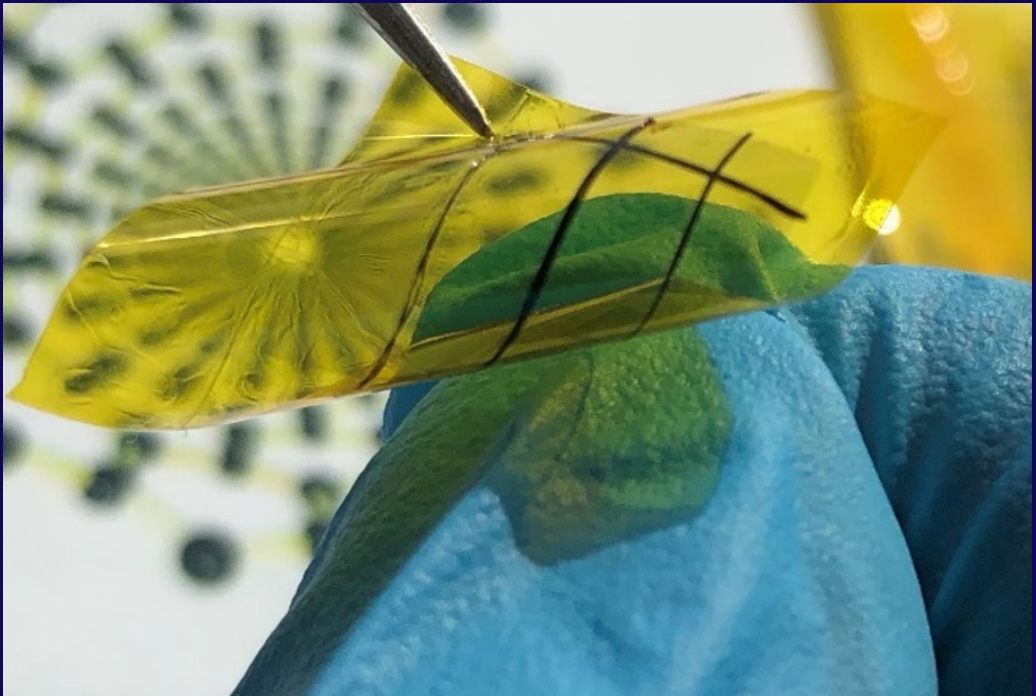


Center for Photonics and Quantum Materials,
Skolkovo Institute of Science and Technology

Department of Applied Physics,
Aalto University

Hybrid heterojunction solar cells using single-walled carbon nanotubes and amorphous silicon thin films

Pramod Mulbagal Rajanna



Skoltech
Skolkovo Institute of Science and Technology

A! Aalto University

DOCTORAL
DISSERTATIONS

Skolkovo Institute of Science and Technology / Doctoral Program in Physics
DOCTORAL THESIS

Hybrid heterojunction solar cells using single-walled carbon nanotubes and amorphous silicon thin films

Pramod Mulbagal Rajanna

Supervisors: Professor Albert G. Nasibulin,
Skolkovo Institute of Science and Technology, Russia
Professor Peter D. Lund,
Aalto University, Finland

Defense Jury: Professor Nikolay A. Gippius (Chairman),
Skolkovo Institute of Science and Technology, Russia
Professor Pavel Troshin,
Skolkovo Institute of Science and Technology, Russia
Professor Dmitry Paraschuk,
Moscow State University, Russia
Professor Aldo di Carlo,
University of Rome, Italy
Professor Anvar Zakhidov,
The University of Texas at Dallas, United States of America

Date & Time: 27 MAY 2020, 17:00 HRS
Venue: ONLINE DEFENSE FROM AALTO UNIVERSITY, FINLAND
(<https://aalto.zoom.us/j/63096711658>)

Hybrid heterojunction solar cells using single-walled carbon nanotubes and amorphous silicon thin films

Pramod Mulbagal Rajanna

A doctoral dissertation conducted under a convention for the joint supervision of thesis at Aalto University (Finland) and Skolkovo Institute of Science and Technology (Russia) for the degree of Doctor of Science (Technology) at Aalto University, to be defended, with the permission of the Aalto University School of Science, at a public examination held at the lecture hall N204 of the school on 27th May 2020 at 17:00.

Aalto University
School of Science
Department of Applied Physics
New Energy Technologies

Supervising professors

Professor Peter D. Lund, Aalto University, Finland

Professor Albert G. Nasibulin, Skolkovo Institute of Science and Technology, Russia

Preliminary examiners

Professor Aldo di Carlo, University of Rome "Tor Vergata", Italy

Professor Dmitry Paraschuk, Moscow State University, Russia

Opponent

Professor Anvar Zakhidov, University of Texas at Dallas, United States of America

Aalto University publication series

DOCTORAL DISSERTATIONS 79/2020

© 2020 Pramod Mulbagal Rajanna

ISBN 978-952-60-3892-6 (printed)

ISBN 978-952-60-3893-3 (pdf)

ISSN 1799-4934 (printed)

ISSN 1799-4942 (pdf)

<http://urn.fi/URN:ISBN:978-952-60-3893-3>

Unigrafia Oy

Helsinki 2020

Finland



Author

Pramod Mulbagal Rajanna

Name of the doctoral dissertation

Hybrid heterojunction solar cells using single-walled carbon nanotubes and amorphous silicon thin films

Publisher School of Science**Unit** Department of Applied Physics**Series** Aalto University publication series DOCTORAL DISSERTATIONS 79/2020**Field of research** Engineering Physics**Manuscript submitted** 6 May 2020**Date of the defence** 27 May 2020**Permission for public defence granted (date)** 5 May 2020**Language** English **Monograph** **Article dissertation** **Essay dissertation****Abstract**

Single-walled carbon nanotubes possess extraordinary optical, electrical, chemical, and mechanical properties. Thin films of randomly oriented SWCNTs have a great potential in many opto-electro-mechanical applications. Moreover, recent developments in photovoltaics have been largely contributed by SWCNTs as a p-type transparent conductor that fulfill the requirements for continuous, fast, and cheap film manufacturing process compatible with the roll-to-roll technology.

The scope of this thesis is the development of a conductive p-type SWCNT transparent conductor and its application in hybrid heterostructure solar cell based on amorphous silicon. For successful implementation of SWCNTs film in solar cells, it is very critical for the SWCNTs to have good physical contact with the material on which it is deposited. At first, quantitative measurements of the adhesion of SWCNT films with substrate materials in air and inert Ar atmosphere using atomic force microscopy was performed. It was found that adhesion of SWCNT films depends on the atmospheric conditions under which it is stored and deposited on a substrate material. The SWCNT film was measured to have higher adhesion in an inert atmosphere. With this understanding, a simple fabrication method of hybrid heterostructure solar cells was proposed in which the SWCNT-PEDOT:PSS composite p-type film forms a coupled continuous hybrid heterojunction with a-Si:H absorber. The optical and electrical properties of this composite was extensively characterized and further optimized by introducing multifunctional components like ultrathin MoO₃ and SWCNT fibers. A rationally designed p-type transparent conductor with a combination of SWCNTs-MoO₃-PEDOT:PSS-SWCNT fibers composite resulted in a state-of-the-art sheet resistance of 17 Ω/sq at 90% transmittance. Moreover, SWCNT fibers by itself can be used as replacement for traditional metal contacts as demonstrated here. This opens a new avenue in widespread energy technologies, where high hole conductivity and transparency of the material are prerequisites for their successful implementation.

Integrating the developed p-type transparent conductor as a window layer and top electrode on a-Si:H in a nip configuration resulted in a dramatic increase in its power conversion efficiency reaching up to 8.8%. The energy level alignment of these solar cells is carefully engineered at a-Si:H and SWCNTs interface by introducing a ultrathin MoO₃ layer that shows the carrier transport by means of band-to-band or trap-assisted tunneling.

Keywords single -walled carbon nanotubes, amorphous silicon, hybrid, heterojunction, thin, films, solar cells.**ISBN (printed)** 978-952-60-3892-6**ISBN (pdf)** 978-952-60-3893-3**ISSN (printed)** 1799-4934**ISSN (pdf)** 1799-4942**Location of publisher** Helsinki**Location of printing** Helsinki **Year** 2020**Pages** 133**urn** <http://urn.fi/URN:ISBN:978-952-60-3893-3>

Acknowledgements

I am deeply indebted to many people for their contributions towards this dissertation, and the quality of my life while working on it.

It has been a privilege to work with Prof. Albert Nasibulin, my supervisor at Skoltech. I am profoundly grateful for his persistent and patient mentoring, support, and friendship through my graduate career, starting from the day he offered me the opportunity to come to Skoltech. I especially appreciate his honest and supportive advice, and his attention to detail while helping me polish my talks and papers. I have learned a lot from my interactions with him, which has helped me to become a more competent researcher.

I am honoured to have worked with Prof. Peter Lund, my supervisor at Aalto University. I thank him for his supervision and examination of this thesis, and for the opportunity to work in his research group (New Energy Technologies). I am deeply grateful for his guidance, continuous support, encouragement, and interest in my work.

I am thankful to Prof. Mikhail Skvortsov, Prof. Alexei Buchachenko, Prof. Nikolay Gippius, and Prof. Pavel Troshin for serving on my committee and for constantly reviewing and evaluating my progress during this thesis.

I am also thankful to Prof. Aldo di Carlo, Prof. Anvar Zakhidov, and Prof. Dmitry Paraschuk for reading this thesis and serving as examiners for my defense.

This dissertation would not have been possible without my collaborators. I thank Dr. Oleg Sergeev and Dr. Hosny Meddeb at DLR institute of networked energy systems, Germany, for working with me on device fabrication and simulation, and Prof. Sergei Bereznev at Tallinn University of Technology for synthesizing organic conductive polymers. I am also thankful for the valuable collaboration with Dr. Olga Volubujeva for SEM, and Dr. Mati Danilson for XPS at Tallinn University of Technology. I would also like to extend my deepest gratitude to Konstantin Larionov and Prof. Pavel Sorokin of National University of Science and Technology MISIS, Moscow, for working with me on adhesion of SWCNT films simulation. I would like to thank Natalia Galochkina, and Natalia Kondrashova for their untiring help during the initial stages of my doctoral thesis with administrative matters.

My doctoral studies have been generously funded by the Ministry of Science and Education, Russian Federation under 'HORIZON 2020' ERA-NET RUS PLUS (RFMEFI61815X0003), the Russian Science Foundation (17-19-01787), a Doctoral Studies Internationalization Program Dora Plus activity 2.2 Fellowship financed by the European Regional Development Fund, an EDUFI Fellowship (# TM-19-11028) from Finnish National Agency for Education, and ASPIRE (Jane and Aatos Erkko foundation, Finland).

Finally, I appreciate the camaraderie and support of my current and former group-mates at Skoltech: Dr. Anastasia Goldt, Dr. Yury Gladush, Dr. Daria Kopylova, Dr. Fedor Fedorov, Dr. Dmitry Krasnikov, Dr. Alexey Tsapenko, Dr. Vsevolod Iakovlev, Dr. Evgenia Gilshteyn, Andrei Starkov (Engineer), Eldar Khabushev, Stepan Romanov, and Alena Alekseeva; and at Aalto: Dr. Imran Ashgar, Dr. Janne Halme, Dr. Kerttu Aitola, Aapo Poskela, and Dr. Lide Yao, without whose help, my work and life would not be smooth. I also sincerely thank Dr. Sergey Luchkin, and Dr. Sergey Tsarev from the Center for Energy Science and Technology, Skoltech for their help, support, and useful discussions during the course of my work. I also extend my deep gratitude to Prof. Tanja Kallio, Aalto University for helping me with ALD depositions.

On a more personal note, I am deeply indebted to my family for the opportunities and support that they provided me. My mother, Prabha and brother, Subodh have been loving and supportive presences, and learned early not to ask when the Ph.D. would be completed. Special thanks to my brother for taking care of the family during my physical absence in their hard times. My father, Rajanna has been an untiring source of sound guidance and advice, which has stood me in good stead. My grandmother, Radha Bai has been a pillar of strength, and has constantly amazed me with her dedication and discipline. Special thanks to my in-laws who have been very supportive and caring.

Finally, I am extremely indebted to my wife Shruthi whose steadfast dedication, help, care, support, and love throughout this journey has continuously amazed me. As I am penning down these words, we have just completed 4 years of our married life. We have blossomed in our relationship from complete strangers to being soul-mates.

My life has been enriched by innumerable people who I cannot begin to thank enough. Saint Tyagaraja's catch-all acknowledgment comes to my rescue: "endarO mahAnubhavulu antarIki vandanamu".

In the memory of my late grand father, Sri Appannachar!!

Espoo, 26 February 2020
Pramod Mulbagal Rajanna

Contents

Acknowledgements.....	9
List of Abbreviations and Symbols.....	13
List of chemicals and elements.....	16
List of Publications.....	17
Author's Contribution.....	18
1. Introduction.....	19
2. Hybrid solar cells & their components.....	22
2.1 Previous work and development.....	22
2.2 Amorphous silicon.....	23
2.3 SWCNT films.....	25
2.4 PEDOT:PSS.....	28
2.5 Molybdenum oxide.....	29
2.6 CNT fibers.....	29
3. Methods.....	31
3.1 UV-Vis-NIT spectroscopy.....	31
3.2 XPS measurements.....	32
3.3 4-point probe measurement.....	33
3.4 SEM and TEM.....	34
3.5 AFM and KPFM.....	35
3.6 I-V measurements.....	35
3.7 EQE measurements.....	37
4. Results and discussion.....	39
4.1 Adhesion of SWCNT films.....	39
4.2 SWCNT-PEDOT:PSS composite.....	43
4.2.1 Optical and electrical properties.....	43
4.2.2 Hybrid solar cell fabrication.....	45
4.2.3 Solar cell characterization.....	47

4.3	Rational design of p-type transparent conductor	54
4.3.1	TCF and solar cell fabrication.....	54
4.3.2	Opto-electro-mechanical properties	56
4.3.3	Solar cell characterization	60
5.	Conclusions and future work	64
	References	66
	Publications 1-5	75

List of Abbreviations and Symbols

a-Si:H	hydrogenated amorphous silicon
AFM	atomic force microscopy
AF	adhesion force
AR	anti-reflecting
AM	air mass
Al:ZnO	aluminum doped zinc oxide
BE	binding energy
B ₂ BT	band-to-band tunnelling
c-Si	crystalline silicon
CNTs	carbon nanotubes
CO	carbon monoxide
CO ₂	carbon dioxide
DOS	density of states
eV	electron-volt
EQE	external quantum efficiency
E _v	valence band edge
E _c	conduction band edge
FOM	figure of merit
FF	fill factor
FWHM	full-width at half maximum
HIT	heterojunction intrinsic thin layer
HSCs	hybrid solar cells
ITO	indium tin oxide
IEC	International Electrotechnical Commission

J_0	reverse saturation current density
J_{sc}	short-circuit current density
KE	kinetic energy
KPFM	kelvin probe force microscopy
MPP	maximum power point
MoO_3	molybdenum trioxide
MEH-PPV	Poly[2-methoxy-5-(2-ethylhexyloxy)-1,4-phenylene-vinylene]
$N(E)$	density of states
NIR	near infrared
NWs	nanowires
η	power conversion efficiency (PCE)
n	diode ideality factor
OCPs	organic conductive polymers
PV	photovoltaics
PCE	power conversion efficiency
PECVD	plasma enhanced chemical vapor deposition
PEDOT:PSS	poly(3,4-ethylenedioxythiophene) polystyrene sulfonate
P3HT	Poly(3-hexylthiophene)
PCBM	Phenyl-C61-butyric acid methyl ester
PCPTDBT	Poly[2,6-(4,4-bis-(2-ethylhexyl)-4H-cyclopenta [2,1-b;3,4-b']dithiophene)-alt-4,7(2,1,3-benzothiadiazole)]
PMMA	Poly(methyl methacrylate)
PI	polyimide
PDMS	polydimethylsiloxane
R_{sh}	sheet resistance
R_s / R_{sr}	series resistance
R_{sh} / R_p	shunt resistance
RH	relative humidity
RMS	root mean square
R	radius of curvature
SWCNTs	single-walled carbon nanotubes

SWE	Staebler-Wronski-Effect
SiO ₂	silicon dioxide
SAFD	surface adhesion force density
SEM	scanning electron microscopy
TCF	transparent conductive film
TEM	transmission electron microscopy
TAT	trap-assisted tunnelling
UV	ultraviolet
Vis	visible
V _{oc}	open-circuit voltage
V _{bi}	built-in voltage
W _f	work-function
XPS	X-ray photoelectron spectroscopy

List of Chemicals and Elements

Au	gold
Ag	silver
Al	aluminum
Ar	argon
Cu	copper
HAuCl ₄	chloroauric acid
HF	hydrofluoric acid
IPA	isopropanol
KOH	potassium hydroxide
Pt	platinum
ZrO ₂	zirconium oxide

List of Publications

This doctoral dissertation consists of a summary of the following publications which are referred to in the text by their numerals

1. Pramod M. Rajanna, Sergey Luchkin, Konstantin V. Larionov, Artem Grebenko, Zakhar I. Popov, Pavel B. Sorokin, Mati Danilson, Sergei Bereznev, Peter D. Lund, and Albert G. Nasibulin. Adhesion of Single-Walled Carbon Nanotube Thin Films with Different Materials. *J. Phys. Chem. Lett.* 2020, 11, 504–509.

2. Pramod M Rajanna, Evgenia P Gilshteyn, Timur Yagafarov, Alena K Alekseeva, Anton S Anisimov, Alex Neumüller, Oleg Sergeev, Sergei Bereznev, Jelena Maricheva, and Albert G Nasibulin. Enhanced efficiency of hybrid amorphous silicon solar cells based on single-walled carbon nanotubes and polymer composite thin film. *Nanotechnology* 29 (2018) 105404 (10 pp).

3. Alena K. Alekseeva, **Pramod Mulbagal Rajanna**, Anton S. Anisimov, Oleg Sergeev, Sergei Bereznev, and Albert G. Nasibulin. Synergistic Effect of Single-Walled Carbon Nanotubes and PEDOT:PSS in Thin Film Amorphous Silicon Hybrid Solar Cell. *Phys. Status Solidi B* 2018, 255, 1700557.

4. Pramod M. Rajanna, Hosni Meddeb, Oleg Sergeev, Alexey P. Tsapenko, Sergei Bereznev, Martin Vehse, Olga Volobujeva, Mati Danilson, Peter D. Lund, Albert G. Nasibulin. Rational design of highly efficient flexible and transparent p-type composite electrode based on single-walled carbon nanotubes. *Nano Energy* 67 (2020) 104183.

5. Pramod M. Rajanna, Peter D. Lund, Albert G. Nasibulin. Hybrid heterojunction solar cells based on single-walled carbon nanotubes and amorphous silicon thin film-a mini review. *Submitted, May 2020.*

Author's Contribution

Publication 1: Adhesion of Single-Walled Carbon Nanotube Thin Films with Different Materials.

The author is mainly responsible for this work. The author developed the idea, designed & conducted the experiments and measurements, and analysed the data. The author was responsible for writing the manuscript, communicating with the journal editor and answering to the reviewers' queries.

Publication 2: Enhanced efficiency of hybrid amorphous silicon solar cells based on single-walled carbon nanotubes and polymer composite thin film.

The author is mainly responsible for this work. The author designed & conducted the experiments, fabricated & measured the devices, and analysed the data. The author was responsible for writing the manuscript, communicating with the journal editor, and answering to the reviewers' questions.

Publication 3: Synergistic Effect of Single-Walled Carbon Nanotubes and PEDOT:PSS in Thin Film Amorphous Silicon Hybrid Solar Cell.

The author is mainly responsible for conceptualization of the idea, design of experiments, measurements, data analysis, and jointly writing the paper. The author was responsible for answering to the reviewers' questions.

Publication 4: Rational design of highly efficient flexible and transparent p-type composite electrode based on single-walled carbon nanotubes.

The author is mainly responsible for this work. The author designed & conducted the experiments, fabricated & measured the devices, and analysed the data. The author was responsible for writing the manuscript, and answering to the reviewers' questions.

Publication 5: Review: Hybrid heterojunction solar cells based on single-walled carbon nanotube and amorphous silicon thin films.

The author is mainly responsible for this work and writing the paper.

1. Introduction

The growing world population with its urbanization are increasing energy consumption [1,2], which is projected to double by 2050 and triple by 2100 [3]. Currently, most of the energy is still supplied by fossil fuels, which has led to severe environmental problems [3], notably climate change. Renewable energy technologies offer solutions to this problem and are expected to be the fastest-growing energy technologies in the coming years, with an expected average growth of 2.3% per year till 2040 [4]. Among renewable energy technologies, photovoltaics (PV) has seen a sharp growth in the last decade with a current generational capacity of 510 GW_p [5]. This is a result of achieving 'grid-parity' in most countries and decreased solar cell costs of over 85% between end of 2009 and first half of 2018 with a total investment of more than \$142 billion [6]. The establishment of grid-parity will further accelerate PV installations allowing it to become a leading contributor to world electricity production by 2040 [7].

Among PV devices, crystalline silicon (c-Si) solar cells have dominated the market with power conversion efficiencies (PCEs) exceeding 26% thanks to their heterojunction with intrinsic layer technology based on thin hydrogenated amorphous silicon (a-Si:H) passivating layers and on interdigitated back contacts on n-type silicon wafers [8,9]. However, as recent technologies are evolving into flexible, versatile and portable electronics, there is also demand for manufacturing solar cells in roll-to-roll processes. Such solar cells would be thin, flexible and could be directly incorporated into buildings, e.g. as roofing shingles. Thin film solar cells, including those made of a-Si:H are suitable materials for roll-to-roll production with the advantages of reduced fabrication costs, increased light absorptivity, and reduced solar cell thickness, thereby reducing material consumption and device weight [10]. Additionally, a-Si:H can be deposited on any foreign substrate by plasma enhanced chemical vapor deposition (PECVD) at close to room temperature [10]. However, as the carrier mobility of a-Si:H is low, an expensive transparent conducting layer as the top contact is needed, such as indium tin oxide (ITO) [11]. Therefore, ITO-free solar cells have become an important focus of research for next generation PV devices

[12,13,22,23,14–21]. Several studies have been reported combining inorganic Si, a-Si:H with organic conductive polymers (OCPs) [12,13,16,19,22,24]. Moreover, carbon-based materials such as carbon nanotubes (CNTs), in particular single-walled CNTs (SWCNTs), have made major contributions to solar cell development in recent years [25–29] and are termed as ‘hybrid solar cells (HSCs)’. Although, several attempts have been made to develop HSCs as a-Si/CNTs, a-Si/OCPs, and CNTs/OCPs, their PCEs have been too low for practical applications [16,30–32].

CNTs are promising materials for thin-film solar cells owing to a wide range of properties from conductors to semiconductors with variable bandgaps based on their atomic structure [33]. While CNTs can have multiple number of walls, SWCNTs exhibit excellent opto-electrical advantages over double and multi-walled CNTs [34]. For this reason, SWCNTs have been used extensively as electrodes in many solar cell devices, replacing brittle ITO, fluorine-doped tin oxide and expensive metal electrodes, especially in c-Si, polymer and more recently in perovskite-based solar cells [25,26]. Although SWCNTs have superior opto-electro-mechanical properties, solar cells based on SWCNTs have not yet matured for practical applications. Moreover, our understanding of the limitations of SWCNTs and solutions to optimize these for PV applications is limited.

This doctoral thesis therefore aims to investigate the underlying fundamental limitations of SWCNTs and provide necessary innovative solutions to allow their optimal usage in PV and other opto-electronic applications. The mechanisms affecting SWCNTs/a-Si:H heterostructures like physical contact or adhesion of SWCNTs with a-Si:H, the opto-electrical properties and inter-tube resistance of SWCNTs, and carrier transport and collection at the interface of a-Si:H and SWCNTs are studied. An energy efficient, environmentally friendly and low cost process technology is developed for fabrication of hybrid thin film solar cells combining a-Si:H and SWCNT films by eliminating boron-doped a-Si:H, transparent conductive layers like ITO, and other traditional metal layers like Au, Ag, Al, and Cu. SWCNTs are proposed as a window layer p-type transparent conductive film (TCF), a potential replacement for all the aforementioned layers and processes, thereby resulting in a less energy-consuming process technology, minimizing material consumption and reducing the net cost.

Despite the relatively short time for development of HSCs based on a-Si:H and SWCNT films the results achieved in this project were motivating. However, their relevant working principles have scarcely been investigated or

are limited to SWCNTs as an electrode. The excellent conductivity and transparency make the SWCNTs material an excellent choice for this task. It has high conductivity with semi-metallic characteristics and is doped to its p-type state. The main highlights of this thesis are the first quantitative evaluation of the adhesion of SWCNT films to some common substrates, development of a rational design for a state-of-the-art p-type TCF using multifunctional component layers to form a single composite layer based on SWCNTs and the establishment of a-Si:H/SWCNTs HSC design with a state-of-the-art PCE of 8.8%.

This thesis is based on the five original publications listed in the List of Publications and divided into five chapters. It is organized as follows: Chapter 1 gives an overview as well as the outline of the thesis. Chapter 2 comprises the brief background of HSCs as well as materials used in this thesis as thin films of a-Si:H, SWCNTs, PEDOT:PSS, molybdenum oxide, and CNT fibers. A short review of a-Si:H and SWCNT HSCs is given. Chapter 3 presents details of the experimental methods for optical and electrical measurements, chemical composition, surface morphology, and solar cell characterization. Chapter 4 presents the main results on the influence of adhesion of SWCNT films to common substrates, introduction of PEDOT:PSS into SWCNT films and its opto-electrical properties, HSC fabrication and characterization, a rational design of a TCF using a combination of SWCNT film, transition metal oxide, PEDOT:PSS and SWCNT fibers carefully matched to form a state-of-the-art p-type TCF, opto-electro-mechanical properties of p-type TCF, fabrication of HSCs based on a-Si:H and TCF, and characterization of HSCs. Chapter 5 summarizes this thesis.

2. Hybrid solar cells and their components

“Hybrid” solar cells combine inorganic and organic materials that are matched for desired physical and opto-electrical properties, functionalization of surfaces or organic/inorganic heterostructures [35]. Device performance is heavily influenced by their electronic structure [35]. The approach in this work is to combine a-Si:H and SWCNT with PEDOT:PSS thin films as a highly efficient hybrid heterostructure solar cell. As SWCNT films are predominantly p-type, they are combined with hole transport PEDOT:PSS as a composite to form p-type TCFs. The current is mainly generated in the a-Si:H absorber layer. Furthermore, these hybrid solar cells are manufactured using a simple fabrication process that is detailed in this thesis.

2.1 Previous work and development

During the last decade, the development of HSCs utilizing thin-film a-Si:H, SWCNTs and OCPs like PEDOT:PSS, P₃HT, PCBM, MEH-PPV, PCPDTBT and polypyrrole has gained increasing interest thanks to their low fabrication cost, large area and the ability to produce mechanically flexible photovoltaic devices at a low processing temperature [12,13,16,17,19,36]. A large body of work has reported a-Si:H/OCPs with PCEs up to 3%. Further, carbon nanomaterials and especially SWCNTs have also been employed owing to their exceptional properties forming heterostructure solar cells with OCPs and a-Si:H, respectively [30–32,37–39]. SWCNTs have also made a major contribution to heterostructure solar cell development with C-Si and more recently with perovskites [26,29].

However, significant progress and the breakthroughs required for the use of CNTs/OCPs and CNTs/a-Si:Hs in real applications have not been achieved. Some reasons for this include the poor opto-electronic properties of SWCNTs, highly unstable OCPs, non-conformity and poor physical contact, large interface resistance, a high Schottky barrier causing band-offsets, and the high tube-tube resistance of SWCNTs. These issues have led to very modest device performance with low currents and high junction recombination [26,40].

There is hence significant potential for the improvement of these materials to allow them to be contenders for flexible and wearable electronic applications. In this work, each of the problems is systematically studied to provide solutions to overcome the limitation of HSC efficiency. The material combines abundance and high transparency with good electrical properties and non-destructive techniques are used for its fabrication.

2.2. Amorphous Thin-Film Silicon

Thin-film a-Si is a well-studied material that has long range disorder and can be deposited by silane as a precursor gas in a CVD process. In this form, however a-Si has a high defect density (10^{19} cm^{-3}) of dangling bonds. They act as primary recombinations centers that reduce the carrier lifetime, diffusion and drift lengths, and pin the Fermi energy such that the material cannot be effectively n- or p-type doped, and hence is not electronically useful. However, it was shown that incorporation of about 10% hydrogen during the deposition process greatly reduces the density of these defects to about 10^{15} cm^{-3} , and that this hydrogenated material can be either n- or p-type doped [41]. The a-Si:H has a larger mobility gap and optical absorption coefficient than c-Si. Unlike c-Si, the edges of the valence and conduction bands are not well defined, and exhibit a continuous distribution of density of states. The energy states in which the charge carriers can be considered as free carriers are described by wave functions that extend over the whole atomic structure. These states are nonlocalized and are called extended states. The disorder in a-Si:H causes the wave functions of the tail and defect states to become localized within the atomic network. These states are called localized states. Consequently, mobility that characterizes the transport of carriers through the localized states is strongly reduced. This feature of a sharp drop in the mobility of carriers in the localized states in comparison to the extended states is used to define the bandgap in a-Si:H. This bandgap is denoted by the term mobility gap, E_{mob} , because the presence of a considerable density of states in the mobility gap is in conflict with the classical concept of a bandgap without any allowed energy states. The energy levels that separate the extended states from the localized states in a-Si:H are called the valence band, E_v , and the conduction band, E_c , mobility edges. This is shown in Figure 2-1 [11,42]. The mobility gap of a-Si:H is larger than the bandgap of single crystal silicon and has a typical value between 1.7 eV and 1.8 eV [11]. Therefore, just 1 μm thickness of a-Si:H is sufficient to absorb virtually all of the incident light that is \geq mobility gap [11].

Hence, a-Si:H has played a crucial role in solar cells as intrinsic absorber layers with doped layers for building PIN and NIP junctions, and an increasingly important role in combination with c-Si in HIT solar cells [11,41,43]. The advancement of thin-film electronics and in particular solar cells has been credited largely to a-Si:H. It has the distinct advantage of cost-effective deposition from the gas phase by PECVD at relatively low temperatures (<100 °C), thereby enabling its deposition onto temperature-sensitive and low cost substrates such as polymers [44]. Besides a variety of designs of the plasma reactor (diode, triode configurations), a range of frequencies from radio frequencies to ultrahigh frequencies is applied. Modifications like remote plasma reactors, where dissociation is spatially separated from deposition, or dissociation by an electron cyclotron resonance reactor or a hot wire CVD, have an influence on film quality. More detailed information on the material and its processes can be found in the literature [11,41,44].

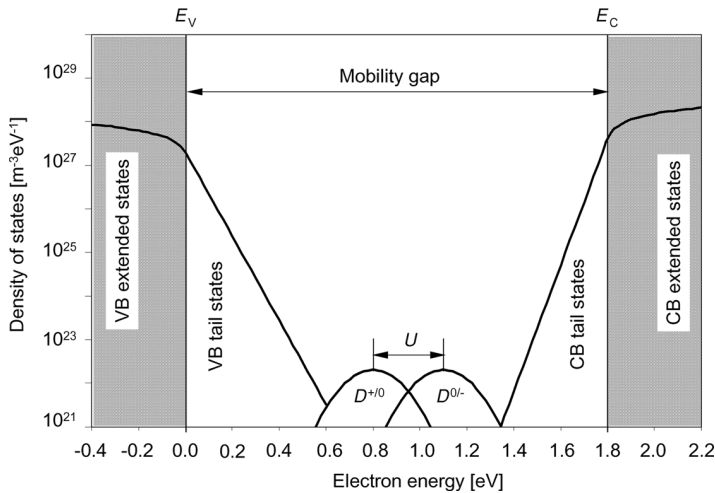


Figure 2-1. Electronic structure in amorphous silicon described by the density of states as function of energy $N(E)$ [11,42].

In general, three types of states can be identified: (1) extended band-like states (shaded grey area in Figure 2-1), similar to the conduction and valence band in c-Si, resulting from overlapping electronic wavefunctions of non- or only slightly distorted bonds in the network. Charge carriers can move freely in these states [45]. (2) Localized band-like states or tail states, resulting from more strongly distorted and thus weak bonds, where no overlap of wavefunctions occurs. At room temperature, charge carriers in these states are frequently excited to the conduction band and recaptured, resulting in a reduced mobility. Consequently, mobility edges are defined at the transition from localized to extended states, as indicated in Figure 2-1. In between the mobility

edges, the mobility gap serves as an equivalent to the band gap in crystalline silicon. As the edge from extended to localized states is not abrupt, the value for the mobility gap depends on its definition or evaluation, impeding a direct comparison of absolute values. (3) Localized defect states resulting from highly distorted or mostly non-saturated bonds, so-called dangling bonds. These build up a distribution of defect states inside the band gap, which act as recombination centres for charge carriers and thus reduce the lifetime of excess carriers [41,45].

The a-Si:H stability was examined by Staebler and Wronski in 1977, who deduced that the conductivity of a-Si:H films is reduced upon illumination [46]. This so-called Staebler-Wronski effect (SWE) is due to an increased defect density resulting from broken Si-H bonds under sample illumination [47]. This in turn results in a deterioration of solar cell performance, which stabilizes after a certain illumination time. The effect is metastable and initial efficiencies of solar cells can nearly be retrieved upon annealing at temperatures below the deposition temperature, typically at 160 °C for deposition temperatures of 180-200 °C [11].

2.3 SWCNT films

SWCNTs have rapidly been incorporated into the development of new types of solar cells comprising SWCNT films, graphene or a polymer and silicon or more recently perovskites [25,26,28,29]. They have the advantages of a simple structure and fabrication, low-cost and promising performance.

SWCNTs are hollow cylinders that can be visualized as having been formed by rolling-up a graphene sheet which is an extended planar hexagonal lattice of purely sp²-bonded carbons [48]. This unique structure has high flexibility, surface area, carrier mobility, chemical stability and optoelectronic properties. Owing to its direct sub-band gaps, tunable photoabsorption from the NIR to the UV range and high conductivity, thin SWCNT films can be used not only as perfect p-type window layers to collect holes in solar cells, but also as transparent conductive electrodes [26,40]. Among SWCNT production techniques, thin films produced by aerosol CVD have been the most successful in heterojunction solar cells [25]. In this section, SWCNT films produced by the aerosol CVD technique are briefly discussed. More information on the material and its processes can be found in the literature [25,33,48].

Aerosol CVD synthesis. Among the various synthesis approaches, the aerosol CVD (floating catalyst) method has proven to be a reliable technique

to produce high-quality SWCNT films with tunable parameters. The main advantages of this method are the high purity and uniformity of the product, a high-yield process completely free from liquid phase or surfactant cleaning, reduced bundle formation and flexibility in terms of substrate selection. All the SWCNTs film used in this thesis were synthesized by the aerosol (floating catalyst) method and consist of 1/3 metallic and 2/3 semiconducting nanotubes; therefore they have a certain bandgap and chirality, that influences its electrical and optical properties [49]. The statistical fractioning of randomly oriented SWCNTs in films limits the conductivity by the introduction of Schottky barriers between the nanotube contacts, which leads to contact resistance that cannot be overcome without further modification process [49].

Briefly, the synthesis is based on catalyst thermal decomposition and a CO disproportionation reaction on a catalyst particle surface. During this process, catalyst particle formation and subsequent SWCNT growth take place directly in the reactor flow (Figure 2-2a). The reactor consists of a quartz tube placed in a furnace (hot zone), a precursor cartridge (filled with ferrocene/silicon dioxide mixture) and a gas supply system (Figure 2-2a). Catalyst precursor (ferrocene) vapor is delivered into the reactor hot zone by passing a gas stream (CO) through the pre-heated cartridge at 60 °C. Additionally, the flow of CO and CO₂ mixture passes through the reactor. Here, CO₂ increases the catalyst lifetime as it preserves the catalyst from deactivation [50,51]. The addition of CO₂ helps to control the output parameters of produced SWCNTs (for instance, longer nanotubes can be yielded at long catalyst lifetimes) as well as other synthesis conditions. The typical synthesis temperature range is from 750 to 1100 °C. Therefore, after partial ferrocene decomposition and catalyst particle formation in the hot zone, catalytic CO disproportionation takes place along with the decomposition of hydrocarbon and ferrocene, which eventually lead to the dissolution of carbon into nanoparticles. This results in nanoparticles saturation by carbon and carbon layer formation on the catalyst particle surface (SWCNTs are formed in cases when catalyst particle size is less than or equal to 5 nm). The SWCNTs film is then collected on a nitrocellulose filter. The surface morphology of randomly oriented SWCNTs is shown in Figure 2-2b and c.

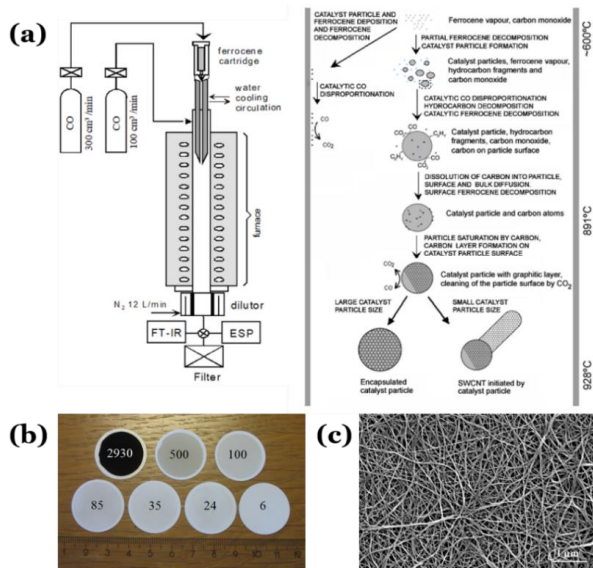


Figure 2-2. (a) Typical SWCNT aerosol-synthesis reactor (left) and SWCNT formation scheme during the synthesis process (right) [49,51,52]; (b) SWCNT films collected on nitrocellulose filters with different thicknesses [53]; (c) Surface morphology of randomly oriented SWCNTs.

Doping: SWCNT films reveal various outstanding optical and electronic properties but still have an issue with the reduction of Schottky barrier between semiconducting and metallic nanotubes. This has led to several processing methods to increase their optoelectronic characteristics. The techniques are based on the shift of the Fermi level (E_F for metallic (M) or semiconducting (S) nanotubes) position. In pristine nanotubes the E_F is usually located in the middle of density of states (DOS). Therefore, if the electrons or holes are added to SWCNTs, the E_F is shifted upward (n-type doping) or downward (p-type doping), compared to the initial position (Figure 2-3a and b), and conductivity increases. Normally, due to the presence of oxygen in the atmosphere, nanotubes become p-type doped, which is again related to the shift of E_F under ambient conditions.

Among several key strategies to modify the charge carrier type (substitutional doping, doping in an electrostatic field, work function change ($\Delta\Phi$) when connected to the metal, ambipolarity, etc.), the adsorption doping has numerous advantages [54,55]. The feasibility reason for this method is the exposure of all carbon atoms of SWCNTs to the environment. In this way, any atom/molecule put on a SWCNT causes charge transfer between the atom/molecule and a nanotube [56,57]. Thus, the selection of an appropriate chemical

dopant that will be put on the SWCNTs is highly important to achieve the desired conductivity. Chloroauric acid (HAuCl_4) and gold chloride (AuCl_3) are the chemical dopants used in this study as reported [54,56].

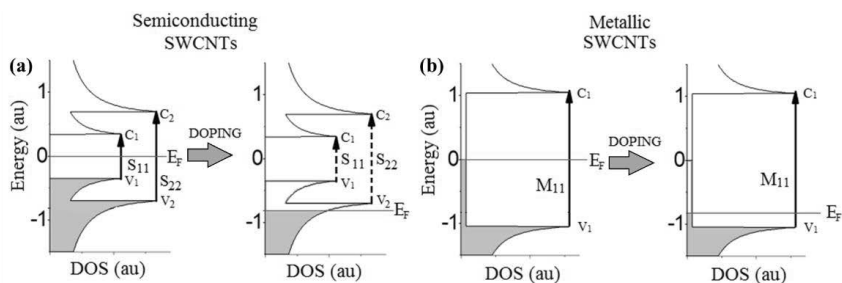


Figure 2-3. Density of states (DOS) of pristine and doped **(a)** semiconducting; and **(b)** metallic SWCNTs, respectively.

2.4. PEDOT:PSS

PEDOT:PSS (Figure 2-4), one of the most classic OCPs, is the most widely used material for fabricating existing PVs as hole transport layers, displays and transistors and various sensing electronics including strain, pressure-, temperature-, humid-, and biosensors, because of its optical transparency in the visible range, tunable electrical conductivity and W_f , high flexibility, stretchability, etc. [58]. PEDOT:PSS is a polymer electrolyte incorporating conducting conjugated PEDOT with positive charges and insulating PSS with negative charges. Oxidized PEDOT is highly conductive, but is insoluble in water; whereas insulating PSS facilitates the dispersion of PEDOT in water and enables a stabilized PEDOT configuration by Columbic attractions. As-cast PEDOT:PSS films have an inherent direct current electrical conductivity (σ) of no more than 1.0 S cm^{-1} ; whereas the modified films are able to show a substantial improvement in conductivity to 2–3 orders of magnitude (the best values reach 4000 S cm^{-1}) through the modification of polar solvents, strong acids, and ionic liquids [59]. Additionally, the films have a typical W_f : 4.8–5.4 eV that is favored for charge transfer and injection with fast kinetics, and the films are preferably used in opto-electronic devices as a p-type contact layer [58]. In this study, PEDOT:PSS was used from the pre-mix of commercially available 5 ml PEDOT:PSS (1.3 wt.%; Sigma-Aldrich) aqueous suspension with 120 μl of glycerin, 250 μl of N-methylpyrrolidone, and 6.25 ml of isopropyl alcohol (IPA).

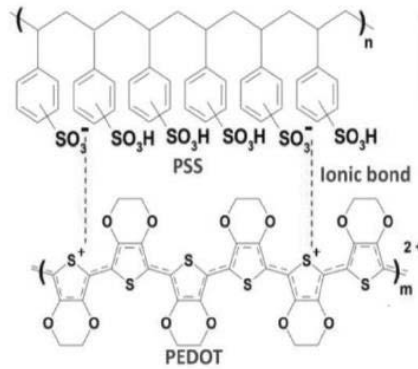


Figure 2-4. Chemical structures and features of PEDOT:PSS [59].

2.5 Molybdenum oxide

The use of metal oxide layers such as MoO_3 in solar cells has recently been in focus [29,60–62]. In the past few years, the high work-function of MoO_3 (6.5 to 6.8 eV) commonly deposited by thermal evaporation, sputtering, and atomic layer deposition has been successfully used as a hole-injection and –extraction material in solar cells which creates a large built-in voltage [18,61–64]. Park *et al.* replaced the conventional p-type a-Si:H and hydrogenated amorphous silicon carbide with MoO_3 [60]. In a recent report, a c-Si solar cell with a MoO_3 layer between a SWCNT film and Au anode was fabricated [29]. The PCE increased to 14.2% with the MoO_3 layer compared to 11.5% for the pristine SWCNTs/Si solar cell with a reduced reflection, indicating AR properties of MoO_3 [29]. Recently MoO_3 nanoparticles have been incorporated into PEDOT:PSS solution to form a composite which is an efficient hole transport layer in perovskite solar cells [65].

2.6 CNT fibers

In traditional p-n or p-i-n junction solar cell structures, either fine metal grids with Au, Ag, Al, Cu, or Ag NWs are deposited, or sputtered ITO as a transparent conductive oxide film is used [66]. However, when using a SWCNT film, which is a randomly oriented porous network of interconnected nanotubes, it is possible that metals will penetrate through the porous network and get into contact with the active layers underneath to form undesired metal-semiconductor junctions during deposition. Jeong *et al.* deposited gold grids on PEDOT:PSS/Si solar cells which resulted in a reduced current density (J_{sc}) from 35.6 to 31.0 mA/cm^2 [67]. To overcome this problem, Li *et al.* used a high density and low porous network of SWCNT films in their SWCNT/C-Si solar cell with spin-coating of Ag NWs [66]. In a recent report, CNT strips have been used

on top of transparent CNT films to fabricate a heterojunction CNT/Si solar cell. The authors showed that the CNT strips not only decrease the series resistance of the CNT thin film, but they also helped to form a better junction with the underlying Si resulting in an improved PCE [28].

3. Methods

This section details the basics of all the experimental measurement techniques used in this work: the optical properties of SWCNT films, PEDOT:PSS, SWCNTs-PEDOT:PSS composite, and SWCNT fibers were measured using UV-Vis-NIR spectroscopy; the chemical composition of the SWCNT film, MoO₃ and depth profile of HSC were measured using XPS; the electrical properties of SWCNT films, PEDOT:PSS, SWCNTs-PEDOT:PSS composite, and SWCNT fibers were measured using the linear 4-probe method; the structural analysis and surface morphology of the SWCNT films and the SWCNT-PEDOT:PSS composite were measured using TEM and SEM, and the cross-section of HSC was also measured using SEM; the surface morphology, RMS roughness and surface potential for work-function of the SWCNT films and the SWCNT-PEDOT:PSS were measured using AFM and KPFM; and all the fabricated HSCs were measured for their performance using J-V and EQE measurements.

3.1 UV-Vis-NIR spectroscopy

UV-Vis-NIR spectroscopy is a common and robust technique to study the optical properties of SWCNTs when used as TCFs that depend on the transmittance value at 550 nm (T_{550}). In addition to that, the film thickness can be easily estimated when the absorbance is known as following: Thickness (nm) = $417 \times \text{Absorbance}_{550 \text{ nm}}$ [68]. The typical set-up consists of a white light source, diffraction mirrors enabling wavelength selection and detectors, covering the studied wavelength range. In **Publication 1**, the absorbance was recorded by a Perkin-Elmer Lambda 1050 spectrometer with a wavelength ranging from 175 to 3200 nm, the aerosol synthesized SWCNT thin film is dry-transferred [53] onto optically transparent quartz (20×25×1 mm). In **Publication 3**, optical transmittance was recorded by a Perkin-Elmer Lambda 1050 spectrometer with a wavelength ranging from 175 to 3200 nm, total reflectance was measured using a Bentham PVE 300 (300-800 nm). Both the equipment were first calibrated without samples and reference. After calibration the measurements were conducted by placing the sample in the beamline center and using a bare

quartz substrate as a reference. In **Publication 4**, total transmittance was recorded using a Bentham PVE 300 (300-800 nm).

3.2 XPS measurements

XPS is a surface analysis technique which provides both elemental and chemical state information virtually without restriction on the type of material analyzed. The sample is illuminated with X-rays - monochromatic or unfiltered Al K α or Mg K α - and photoelectrons are emitted from the surface. The kinetic energy of these emitted electrons is characteristic of the element from which the photoelectron originated. The position and intensity of the peaks in an energy spectrum provide the desired chemical state and quantitative information [69]. The chemical state of an atom alters the BE of a photoelectron which results in a change in the measured KE. The BE is related to the measured photoelectron KE by the simple equation; $BE = hv - KE$, where hv is the photon (x-ray) energy. The chemical or bonding information of the element is derived from these chemical shifts [69].

In **Publications 1, 3 and 4**, a Kratos Analytical Axis Ultra DLD spectrometer equipped with a monochromatic Al K α X-ray source and an achromatic Mg K α / Al K α dual anode X-ray source was used to measure the elemental composition of ZrO₂ and a-Si:H cantilever tips, SWCNT film, and MoO₃, respectively. The monochromatic Al K α anode (1486.6 eV) was operated at 150 W and 15 kV. The 180° hemispherical energy analyzer with an average radius of 165 mm was operated using a hybrid lens mode at a pass energy of 160 eV for survey spectra and 20 eV for regions spectra. Additionally, in **Publication 4**, 40 eV pass energy was used for depth profile of the TCF₃ hybrid solar cell. XPS spectra were recorded at a takeoff angle of 90° from the surface of the sample holder using an aperture slot of 300 × 700 μm^2 . Samples were mounted on a stainless-steel sample bar (130 × 15 mm²). The binding energy values were calculated on the basis of the C 1s peak at 284.6 eV. The relative atomic concentrations of the elements were determined from the appropriate integrated peak areas at the core level and the sensitivity factors provided by the original analysis Kratos Vision 2.2.10 software. The Shirley background subtraction was used to calculate relative atomic concentrations. For surface cleaning and the bulk composition information, Minibeam I ion (Ar⁺) source (2 keV, 10 mA, 30 s per cycle) was used.

3.3 Four-point probe measurement

The most common method for measuring the sheet resistance of any semiconductor material is the 4-point probe. It is well-known that for a regular three-dimensional conductor, the resistance R follows [70]

$$R = \rho \frac{L}{A} = \rho \frac{L}{W \cdot t} = \frac{\rho}{t} \cdot \frac{L}{W} = R_S \cdot \frac{L}{W}$$

where ρ is the resistivity, L is the length, A is the cross-section, W is the width and t is the thickness of thin film.

For the 4-point probe, the linear method is used throughout this thesis (Jandel RM3000), the sheet resistance, R_S and corresponding conductivity, σ is evaluated in the following way:

$$R_S = \frac{\rho}{t} = \frac{\pi}{\ln 2} \cdot \frac{V_{probe}}{I_{probe}} \Omega/\square \text{ and } \sigma = \frac{1}{\rho} \text{ S/cm.}$$

The idea of the linear 4-point probe is to use four electrodes, which are linearly placed close to each other and far from the sample edges as shown in Figure 3-1. Two electrodes are used to apply current (outer electrodes), while the other two register the voltage (inner electrodes). The separation of current and voltage electrodes eliminates the lead and contact resistance from the measurement. Since the measured resistance of the film depends on its thickness, usually two more characteristics are calculated, which can be used to compare different materials – the FoM and equivalent sheet resistance (R_{90}) for a film with R_S and light absorbance at 550 nm (A_{550}) [53]:

$$FoM = \frac{1}{R_S \cdot A_{550}}; R_{90} = \frac{R_S \cdot A_{550}}{\log(10/9)}$$

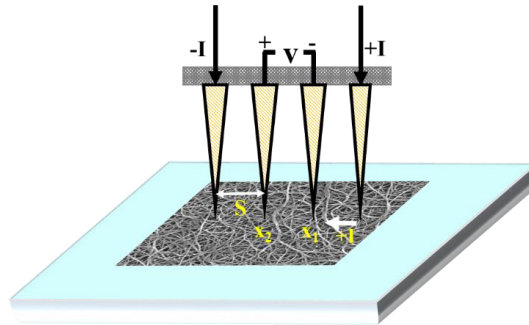


Figure 3-1. Schematic of 4-point probe measurement [70].

3.4 SEM and TEM

Electron microscopy techniques are powerful tools for the characterization of individual SWCNTs as well as the film morphology. In this work, we used SEM to observe the surface morphology and cross-section of the SWCNT film and hybrid solar cells; and TEM to analyze the nanoscale structure of SWCNT film.

In **Publication 1**, the SEM measurements were performed using a JEOL JIB-4700F Multi Beam system for the surface morphology and cross-section of the SWCNT film. Prior to ion milling, a 1 μm thick Pt layer was deposited to avoid gallium ion beam damage to the nanotube film. For coarse and fine milling, the probe currents were set to 3 nA and 300 pA at 30 kV, respectively. The final polishing was performed by a 30 pA probe current and 5 kV accelerating voltage. In **Publication 2**, a Carl Zeiss NEON 40 EsB field emission SEM combining a GEMINI lens design with an advanced Canion FIB column (equipped with Gallium liquid metal ion source) was used (installed at DLR Institute of Networked Energy Systems, Oldenburg, Germany) for measuring the cross-section of the hybrid solar cell. Prior to investigation, the sample was coated with a thin metal contrast layer. The cross-section was formed with focused ion beam at 2 mA emission current, 30 kV acceleration voltage and 10 nA milling current. Multi-step polishing was performed at milling currents from 200 to 20 pA. The SEM image was obtained at 20 kV acceleration voltage using in-lens secondary electron detectors. In **Publication 3**, a FEI Helios Nanolab 660 SEM was used with a maximum accelerating voltage of 30 kV to investigate the morphology of SWCNT film and SWCNT/a-Si solar cell cross-section. In **Publication 4**, surface morphology and film thickness were measured with a high-resolution HR-SEM Zeiss Merlin (installed at Tallinn University of Technology) equipped with an In-Lens SE detector for topographic imaging. Measurements were made at an operating voltage of 2 kV.

TEM measurements were performed on SWCNT films in **Publication 3 and 4** by simply transferring the films onto a Lacey carbon-coated TEM-grid. A double aberration-corrected high-resolution TEM FEI Tecnai G2 F20 (HR-TEM) was used to investigate the structure and geometry of the nanotubes. The microscope was operated at an accelerating voltage of 80 kV (**Publication 3**) and 200 kV (**Publication 4**) and with the minimal electron illumination time possible.

3.5 AFM and KPFM

AFM is a well-known technique that can be used to visualize and measure surface structure with unprecedented resolution and accuracy [71]. It is also used to measure force-distance curves, which provide valuable information on local material properties such as elasticity, hardness, Hamaker constant, adhesion and surface charge densities [72]. It can be operated in contact- and non-contact-mode. KPFM is an AFM based tool to measure the local contact potential difference between a conducting AFM tip and the sample, thereby mapping the work function or surface potential of the sample at a high spatial resolution. KPFM has been used extensively to characterize the nano-scale electronic/electrical properties of metal/semiconductor surfaces and semiconductor devices [73].

In **Publication 1**, adhesion force experiments were performed in air using a Bruker MultiMode V8 AFM operating in peak force quantitative nanomechanical mapping mode. Experiments in the inert argon (Ar) environment were performed with Cypher ES AFM (Asylum Research). Prior to each measurements, the probes were calibrated to determine the exact spring constant and displacement in nm. The force-distance curves were collected using each probe on the SWCNT substrate over a grid of 256×256 points² in air and 32×32 points² in Ar on a $10 \times 10 \mu\text{m}^2$ area with the maximum applied force ranging from 5 to 200 nN. From these maps, average adhesion force and deformation were extracted. In **Publications 2 and 3**, KPFM from Asylum Research—Cypher ES was used to test the work function of the SWCNTs, PEDOT:PSS and SWCNTs-PEDOT:PSS composite film. We used Budget Sensors ElectriMulti75-G tips with a spring constant of 1.43 N m^{-1} and the first resonance frequency of 62.081 kHz. The measurements were conducted in an Ar atmosphere glovebox in two pass amplitude modulated-KPFM with the second pass lift height at 35 nm. Highly oriented pyrolytic graphite ZYA was used for calibration prior to the actual measurements.

3.6 Current density-Voltage (J - V) measurements

The performance of a solar cell device is evaluated by its current density-voltage (J - V) curve under illumination [11]. In Figure 3-2, a typical J - V curve of a solar cell is shown. The short-circuit current density J_{SC} is the maximum current density and is obtained in short-circuit condition at $V = 0$. In the ideal case, it should equal the photo-generated current density J_{ph} , assuming that the dark current at short-circuit conditions can be neglected (close to zero in absence of light). The open-circuit voltage V_{OC} is the maximum voltage

generated by the solar cell and is obtained at $J = 0$, when no net current is flowing. At any point on the J - V curve, the power density that is delivered by the solar cell is defined by $P = V \times J$. The point where the power reaches its maximum P_{max} is called the maximum power point (MPP) with its corresponding current density, J_m , and voltage V_m . The fill factor FF is defined as the ratio of the maximum output power (density) of the solar cell to the product of the short-circuit current (density) J_{sc} times the open-circuit voltage V_{oc} [11]: $FF = \frac{P_{max}}{J_{sc} \times V_{oc}} = \frac{J_m \times V_m}{J_{sc} \times V_{oc}}$ which corresponds to the ratio of the shaded rectangle to the rectangle with the dashed border in Figure 3-2. The fill factor FF is linked to the series and shunt resistance R_s and R_{sh} of the solar cell that are calculated from the slope dV/dJ at $V = V_{oc}$ and $V = 0$, respectively. The R_s represents ohmic resistance in the connection wires up to the solar cell and other ohmic resistances within the solar cell between the external connection point and the actual active device; R_{sh} identifies the actual ohmic shunts, and also symbolizes the recombination losses within the solar cell [11]. In principle, for any solar cell the R_s and R_{sh} resistances arise from losses that occur in different regions of the solar cell, and R_s should be as low as possible and R_{sh} is high as possible. FF is a very sensitive experimental indication of the quality of a solar cell and it should be used as a complimentary quantity, in addition to the open-circuit voltage V_{oc} to characterize solar cell quality [11]. Finally, the power conversion efficiency (PCE) η is defined as the ratio of maximum power, P_{max} , provided by the solar cell to the power of the incident light P_{ill} , and can be calculated from, $\eta = \frac{P_{max}}{P_{ill}} = \frac{J_{sc} \times V_{oc} \times FF}{P_{ill}}$. Solar cells in this work are characterized by four parameters: J_{sc} , V_{oc} , FF , and η .

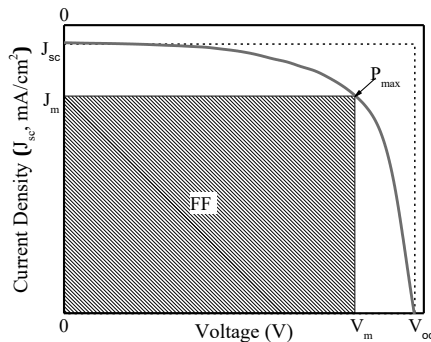


Figure 3-2. Current density-voltage, J - V curve of a solar cell and the parameters that can be evaluated: short-circuit current density J_{sc} , open-circuit voltage V_{oc} , current density and voltage at the MPP J_M and V_M , respectively.

The nature of a J-V curve depends on the environmental conditions under which it has been measured. Therefore, standard measurement and reporting conditions have been agreed by the IEC for determining the PCE of the solar cell: an illumination spectrum called Air Mass 1.5G (AM1.5G) with an input power P_{ill} of $1,000 \text{ Wm}^{-2}$ and temperature of $25 \text{ }^\circ\text{C}$ as in IEC 60904-1 and IEC-60904-3 [74,75]. These are referred as 1Sun conditions. The AM1.5G spectrum cannot be completely achieved, hence it is approximated by using a solar simulator in the laboratory [11]. Throughout this thesis, the solar cells are measured using Oriel Sol3A Class AAA, Newport Corporation coupled with a source-meter unit Keithley 2400.

3.7 EQE measurements

A J - V curve measurement yields information on the absolute value of the J_{sc} produced in a solar cell. However, this simple measurement does not yield information on the loss mechanisms that are responsible for the fact that not every photon in the solar spectrum contributes to J_{sc} . In the ideal case, every photon with a suitable energy $E > E_g$, where E_g is the band gap of the absorber material, would lead to one electron-hole pair being collected at the terminals of the solar cell. However, in reality this is not the case due to the following reasons: parasitic absorption of the photon themselves, through part of the photons not being absorbed at all within the solar cell, or finally through the recombination of electron-hole pairs. Therefore, we are interested in exploring the reasons for these losses. The EQE method sheds light on this problem through spectral measurement of the J_{scEQE} . The EQE is defined as the number of electrons collected per photon incident on the solar cell according to [11] $EQE = \frac{J_{sc}^{EQE\lambda}}{q \times \phi(\lambda)}$ where $\phi(\lambda)$ is the incident photon flux per time and unit area of the incident light for a certain wavelength and q is the elementary charge. The measurement is performed by illuminating a solar cell with monochromatic light and measuring the photo-generated current for a given wavelength. The measurements are performed in short-circuit conditions. In order to improve the signal-to-noise ratio, the probe light was chopped and changes in photocurrent were detected using a lock-in amplifier.

The EQE of the solar cells in this thesis was measured using a Bentham PVE300 spectral response measurement system. This system used two sources of 75W xenon (300–700 nm) and 100W quartz halogen (700–1800 nm) coupled with a monochromator with a $1.85 \times 1.85 \text{ mm}^2$ slit at the output, which provides an approximately $2 \times 2 \text{ mm}^2$ monochromatic probe beam on the working plane of a calibrated solar cell. To correct the signal from the lamp

spectrum, calibration was performed on a monocrystalline-Si sample. By integrating the EQE curve over the investigated wavelength range (300 – 800 nm) between λ_1 and λ_2 , the current density $J_{sc}^{EQE\lambda}$ of the solar cell can be calculated, with the assumption that the $J_{sc}^{EQE\lambda}$ without light bias will be equal to the J_{sc} from J - V curve [76]: $J_{sc}^{EQE\lambda} = -q \int_{\lambda_2}^{\lambda_1} EQE(\lambda) \phi_{ph,\lambda}^{AM1.5} d\lambda$ where q is the elementary charge and $\phi_{ph,\lambda}^{AM1.5}$ the photon flux density of the AM1.5G solar spectrum.

4. Results and discussion

Each of the following sections describes the main results obtained in Publications 1-4.

In this section, the results obtained in the development of a conductive p-type SWCNT transparent conductor and its application in hybrid heterostructure solar cell based on amorphous silicon are discussed. At the beginning, the results obtained for quantitative measurements of the adhesion of SWCNT films with substrate materials in air and inert Ar atmosphere using atomic force microscopy is presented. It is found that adhesion of SWCNT films depends on the atmospheric conditions under which it is stored and deposited on a substrate material. Following this, a simple fabrication method of hybrid heterostructure solar cells is proposed in which the SWCNT-PEDOT:PSS composite p-type film forms a coupled continuous hybrid heterojunction with a-Si:H absorber. The opto-electrical properties of this composite is extensively characterized and further optimized by introducing multifunctional components like ultrathin MoO₃ and SWCNT fibers. Finally, a rationally designed p-type transparent conductor is proposed with a state-of-the-art sheet resistance of 17 Ω /sq at 90% transmittance. Integrating the developed p-type transparent conductor as a window layer and top electrode on a-Si:H in a nip configuration resulted in a dramatic 16% increase in its power conversion efficiency reaching up to 8.8%.

4.1 Adhesion of SWCNT films (Publication 1)

This section focuses on the systematic investigation of the adhesion properties of SWCNT films with various substrate materials, including SiO₂, ITO, c-Si, a-Si:H, ZrO₂, Pt, PDMS, and SWCNTs for self-adhesion, using atomic force microscopy in air and an inert atmosphere. The results outlined here enable a fundamental understanding of the parameters governing SWCNT film adhesion, and provide a mechanism to improve the adhesion for its efficient usage in opto-electronic devices.

In this work, aerosol synthesized SWCNTs [77,78] are dry-transferred from a nitrocellulose filter [79] to a Si wafer. The film was investigated in an

atomic force microscope by collecting force-distance (F-D) curves between the SWCNT thin film sample and cantilevers coated by a given material, as shown in Figure 4-1.

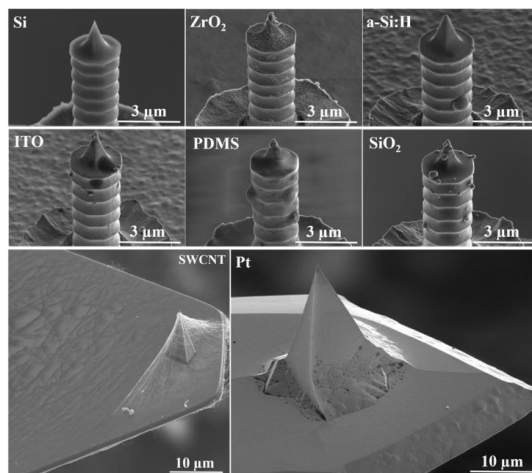


Figure 4-1. Cantilever tips covered with different materials: Si, ZrO₂, a-Si:H, ITO, PDMS, SiO₂, SWCNT, and Pt. Reprinted and adapted with permission from (J. PHYS. CHEM. LETT. 2020, 11, 2, 504-509) under a CC-BY license. Copyright (2020) American Chemical Society.

Collected maps of F-D curves (averaged over 65, 536 measurements in air and 1024 measurements in inert Ar atmosphere) were analyzed by the microscope software. The sample deformation, adhesion force, and peak force values were extracted from F-D curves [80] as shown in Figure 4-2a and 2b. Peak force, or maximum force load, is a predefined set point parameter that is controlled by a microscope feedback loop system.

In order to determine and compare the intrinsic adhesion parameters between SWCNTs and a given material, the measured adhesion force was normalized by the tip-CNT contact area, which is governed by aforementioned force load and tip radius. The Hertz model [81] was used to estimate the tip-surface contact area at the extremum applied force as $S = \pi \times R_{tip} \times h$, where R_{tip} is the tip apex radius and h is the deformation. Within this model it is assumed that the tip apex is a rigid sphere of a certain radius R_{tip} , which was measured on the dimpled aluminum substrate [82], the CNT surface is elastic half space, and the strain is in the elastic limit. The surface roughness is neglected. Despite the fact that in the Hertz model the contact is nonadhesive, it can be accurately applied to adhesive contacts when the adhesive force is small relative to the applied force. The maximum applied force is limited due to the fact that the probe may

drop through a meshy SWCNT surface under a high force loading. As a result, the tip-sample contact area sharply increased due to side contacts of the tip with surrounding CNTs, leading an augmented adhesion force (e.g. Figure 4-2c shows the change in the slope of adhesion force with deformation for ZrO_2 at a peak force of 50 nN as in the inset). With this assumption the moment of the tip drop is inferred from the slope break in the plots shown in Figure 4-2c. With increasing applied force, the adhesion force demonstrates a gradual linear growth. Applying a force of 50 nN resulted in a steep gain in the adhesion force and in some cases cutback of the deformation as shown in Figure 4-2c and corresponding F-D curves in Figure 4-2b. The measured AF as described above [72,80,83] and the calculated SAFD, which is the adhesion force normalized to the contact area, are represented in Figure 4-2d.

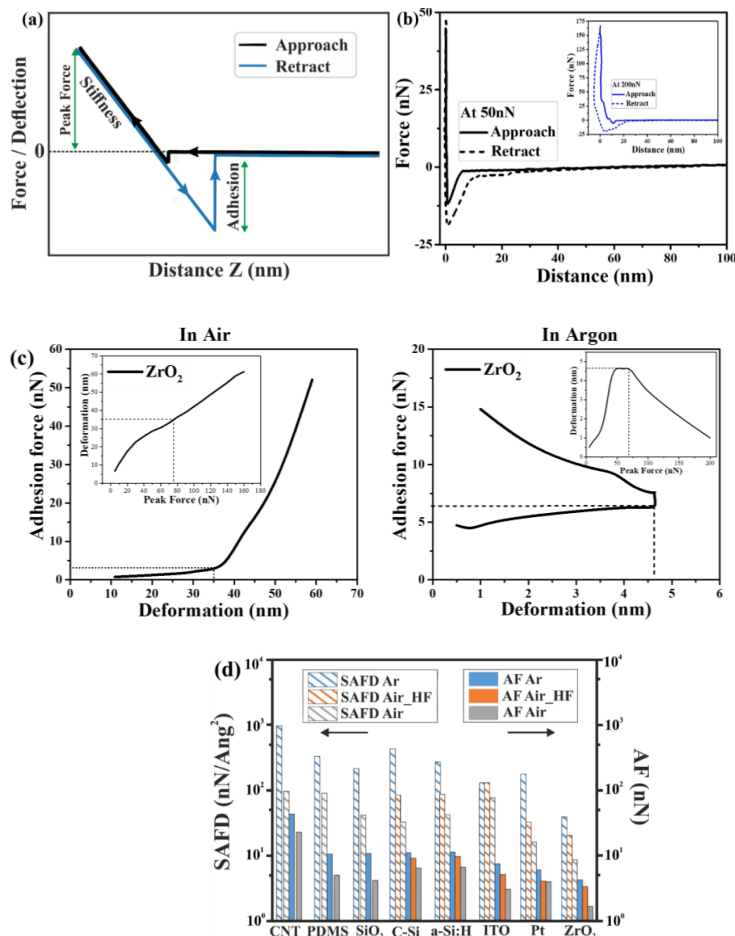


Figure 4-2. (a) Schematic F-D curve; (b) Force-distance curves of SWCNT and ZrO_2 at a peak force of 50 nN and 200 nN captured in an inert Ar atmosphere; (c) Adhesion force *versus* deformation measured in air and inert Ar atmospheres between a SWCNT film and ZrO_2 ; and (d) Adhesion force (AF) (right

axis, solid bars) and surface adhesion force density (SAFD) (left axis, dashed bars) of SWCNT thin films with various materials. Reprinted and adapted with permission from (J. PHYS. CHEM. LETT. 2020, 11, 2, 504-509) under a CC-BY license. Copyright (2020) American Chemical Society.

For all the studied materials, the normalized adhesion force (adhesion force density) in the inert Ar atmosphere was higher than in ambient air, which can be explained by the difference in the ambient humidity and its influence on SWCNTs as shown by Shandakov *et al.* [84]. RH can affect adhesive properties, especially at the nanoscale, due to the formation of a capillary bridge when RH exceeds a threshold value of roughly 25% [85–87]. The capillary force strongly depends on the sample's local curvature, which affects capillary bridge geometry resulting in a higher adhesion force for a concave surface and a lower adhesion force for a convex surface [85,88]. On hydrophilic surfaces, increasing humidity results an increased pull-off force, whereas on hydrophobic surfaces humidity has a negligible effect [89,90]. Since SWCNTs are hydrophobic [91] and possess a convex surface geometry, the capillary bridge effect is likely to be negligible. Instead, the smaller adhesion force in air is better explained by the reduction of the VdW forces in a polar water medium between the tip and the SWCNT thin film [92,93].

The experimentally measured adhesion force shown in Figure 4-2d can explain the following observations: SWCNT thin films are easily dry-transferred onto a-Si:H, Si, SiO₂, and PDMS in air, while under the same conditions their transfer onto ITO and Pt is complicated and completely failed on ZrO₂. However, the same SWCNT thin films are easily dry-transferred onto all the materials in an inert atmosphere.

To verify that the adhesion force is strongly dependent on the humidity, the a-Si:H, C-Si, ZrO₂, ITO, and Pt coated tips were fluorinated (HF-treated). The process of fluorination (HF-treatment) is well-known to alter the surface properties of materials without changing the bulk characteristics of the pristine material [94,95]. The altered properties may include wettability, adhesion, chemical stability, permeation, electrical conductivity, bio-compatibility, grafting, mechanical behavior, and several others [94]. Dry process fluorination was used, which proceeds spontaneously at room temperature by exposing the samples to HF vapor for 60 seconds. Each tip was calibrated again immediately after HF treatment and the adhesion force measurements were conducted on the same SWCNT thin films in air at a peak force of 50 nN. The measured adhesion forces were recorded for the HF treated tips as illustrated in Figure 4-

2d showing that the adhesion force increased for all HF treated tips. This trend is similar to the adhesion force measurements conducted in the inert atmosphere. Moreover, after the fluorination process SWCNT films can be easily dry-transferred even onto problematic materials, such as ITO, Pt, and ZrO₂.

To summarize, through experimental observations it can be stated that the adhesion is greatly influenced by the environmental conditions and surface functionalization. It is observed that the SWCNT films have a better adhesion in an inert Ar atmosphere. However, the adhesion affected by storing the samples under ambient conditions can be greatly improved by a simple HF-treatment. This provides new insight into the physical mechanisms of SWCNT thin film adhesion that will be useful for its successful implementation in carbon nanotube based devices.

4.2 SWCNT-PEDOT:PSS (Publication 2)

The goal of this section is to utilize the knowledge of SWCNT film adhesion and introduce the synergistic effect of SWCNT film and conductive polymer PEDOT:PSS as effective p-type window layer and electrode in hybrid thin film solar cells using a-Si:H. The results outlined here enable a fundamental understanding of the opto-electrical properties of SWCNT films and composite (SWCNT-PEDOT:PSS) films, and the fabrication of SWCNT/a-Si:H, PEDOT:PSS/a-Si:H, and SWCNT-PEDOT:PSS/a-Si:H hybrid thin film solar cells (HSCs), and introduce PMMA as an effective AR layer.

4.2.1 Optical and electrical properties

Aerosol synthesized SWCNT films [77,79,96] of various transmittance values were characterized for their thickness and sheet resistance. The calculated thickness for a film with a transmittance of $T = 90\%$ was about 18 nm (as described in section 3.1) and the measured thickness from AFM was about 19 ± 1 nm. They were dry-transferred [77] onto cleaned micro glass slide (1×1 cm²) and Si wafer (1×1 cm²) to measure their sheet resistance and thickness, respectively. The SWCNTs film transferred on Si wafer was densified using isopropanol and allowed to dry till the solvent evaporation. A scratch was made on the SWCNTs film surface to measure the thickness using AFM. The thickness was averaged over 50 measured points. Figure 4-4 shows the dependence of thickness and sheet resistance on the transmittance at 550 nm. As transmittance increased from 44.4% to 93.5% the sheet resistance increased from 45 ± 2 to 360 ± 2 Ω/\square respectively. In addition, a simple drop-cast of

PEDOT:PSS (2 μl) on the SWCNT films led to a decrease in the sheet resistance by nearly half to 23.4 ± 3.0 and $187.2 \pm 4.0 \text{ } \Omega/\square$ for the SWCNT films with transmittances of $T = 44.4\%$ and $T = 93.5\%$, respectively.

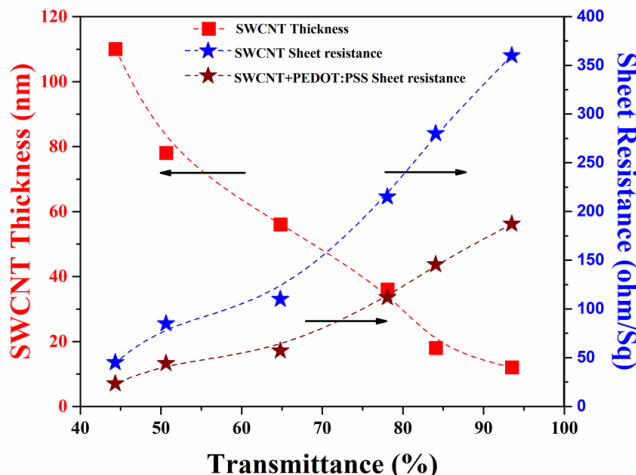


Figure 4-4. Dependence of SWCNT film thickness and sheet resistance on transmittance at 550 nm. Reprinted and adapted with permission from (NANOTECHNOLOGY 29 (2018) 105404 (10PP)) under a CC-BY license. Copyright (2018) IOP Publishing Ltd.

KPFM was used to better understand the decrease in the sheet resistance of SWCNTs with PEDOT:PSS. Three SWCNT film samples with different thicknesses (CNT10, CNT20, and CNT100) were measured with and without PEDOT:PSS. For comparison, a single PEDOT:PSS film was also measured separately. The values of the work function were calculated from KPFM surface potential measurements for the pristine SWCNTs ($4.50 \pm 0.05 \text{ eV}$), composite film ($4.95 \pm 0.05 \text{ eV}$), and PEDOT:PSS ($5.30 \pm 0.05 \text{ eV}$). Fan *et al.* reported similar values of work functions measured by ultraviolet photoemission spectroscopy [97].

The decrease in the sheet resistance of the SWCNT-PEDOT:PSS (composite) film and the increase in its work function compared to the pristine SWCNT film can account for the fact that every single carbon atom are on the surface exposed to the environment. Therefore, any atom/molecule put on a SWCNT cause changes in their electronic structure and charge transfer between the atom/molecule and a nanotube. Therefore, when PEDOT:PSS is injected it filled micropores in the SWCNT film and, that the holes in the PEDOT:PSS patches can transfer to the interconnected SWCNT network consequently, doping the SWCNTs [56,57,97]. As can be seen from Figure 4-5a and 5b, the surface of the composite film is flat and the SWCNT bundled network cannot be

observed clearly from the top of the composite film. This is confirmed by the AFM surface roughness measurements, wherein the pristine SWCNT films showed a RMS roughness of 20 nm, while the composite film RMS roughness was 7 nm. The effect of SWCNT doping can be clearly seen as the work function of the composite film is higher than that of the pristine SWCNTs. Although PEDOT:PSS is less conductive and has a low carrier mobility, the continuous SWCNT network serves as a carrier transport bridge due to its high carrier mobility. Moreover, the net effect of conductivity enhancement is observed to be more pronounced for thinner SWCNT films with PEDOT:PSS. This is probably due to more even distribution of the conducting polymer in the network of SWCNT bundles [97]. This results in a homogeneous coating throughout the thickness of thinner SWCNT films.

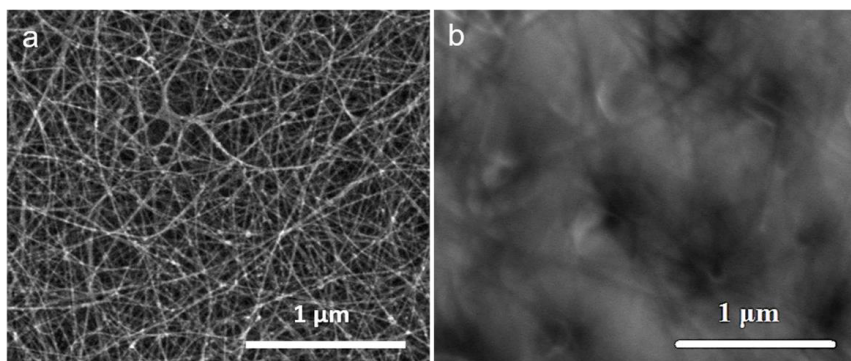


Figure 4-5. Surface morphological SEM image of **(a)** the randomly oriented pristine SWCNT films; **(b)** uniformly coated composite film (PEDOT:PSS - SWCNT film). Reprinted and adapted with permission from (NANOTECHNOLOGY 29 (2018) 105404 (10PP)) under a CC-BY license. Copyright (2018) IOP Publishing Ltd.

4.2.2 Hybrid solar cell fabrication

Figure 4-6a schematically illustrates the HSCs fabrication procedure. The initial layers were fabricated on Corning Eagle XG glass. First, Al:ZnO layers were deposited by DC-sputtering as a transparent back contact for bifacial solar cells. Then, n-doped (30 nm) and intrinsic (i) a-Si:H (300 nm) layers were grown using PECVD using silane, hydrogen and phosphine on top of the Al:ZnO [98]. The i-a-Si:H surface was treated with HF vapor for 140 seconds to remove the native oxide from the surface. Initially, three types of solar cells were fabricated under the same conditions: SWCNT/a-Si:H, PEDOT:PSS/a-Si:H and PEDOT:PSS-SWCNT/a-Si:H.

The SWCNT film was dry-transferred onto an HF-treated i-a-Si:H surface and densified by drop-cast of IPA to ensure a better contact and adhesion to form an SWCNT/a-Si:H HSC. The samples were further heated to 75 °C in air for 5 minutes to remove the residual solvent.

An electrically conductive PEDOT:PSS polymer, was chosen for application in PEDOT:PSS/i-a-Si:H HSC due to its high hole mobility and environmental stability. PEDOT:PSS was drop-cast or spin coated on top of the i-a-Si:H structures for 90 seconds at 3000 rpm with an acceleration speed of 800 rpm/second from the mixture of aqueous suspension of 5 ml PEDOT:PSS (1.3 wt % Sigma-Aldrich) with glycerine, N-methylpyrrolidone and IPA in a ratio of 1:2:19 respectively. Lastly, to evaporate residues from the solvent and to activate the acceptor states of the polymer [99] the devices were annealed on a hot plate at a temperature of 160° C for 10 minutes.

Subsequent to annealing rectangular shaped front contacts were made at the edges using silver paste on SWCNT/a-Si:H and PEDOT:PSS/a-Si:H HSC structures, respectively. To harden the front contacts the devices were annealed at 160° C for 5 minutes on the hot plate. The active area of the SWCNT/a-Si:H and PEDOT:PSS/a-Si:H HSCs was around 0.5 cm².

Further, a series of pristine SWCNT films with varying thicknesses (10 nm, 20 nm, 40 nm, 60 nm, 80 nm, and 100 nm) was dry-transferred onto an HF treated i-a-Si:H surface under ambient conditions [77]. A thin PEDOT:PSS layer with a thickness of 50±5 nm was deposited by a simple drop-cast technique to form PEDOT:PSS-SWCNT/a-Si:H HSCs. It was heated on a hot plate in air at 160 °C for 10 minutes. A thin strip of silver paste was marked at the edges on four sides forming an active HSC area of 0.3 cm².

The back contact Al:ZnO was reached locally by wet chemical etching of both silicon layers (330 nm) using 6 M KOH solution. Prior to the etching, the samples were heated to 160 °C in air on a hot plate for 20 minutes. A small volume of 1 µl KOH solution was drop-cast at the edge of the heated samples of the a-Si:H structure. The chemical reaction occurred immediately and the samples were removed from the hot plate after 5 seconds and then rinsed with deionized water. The samples were flushed with nitrogen gas and then heated to 70 °C in air for 5 minutes to ensure water evaporation. The Al:ZnO resistivity was measured to be 16 Ωcm. The completed architecture of the SWCNT/a-Si:H solar cell device is shown in Figure 4-6b.

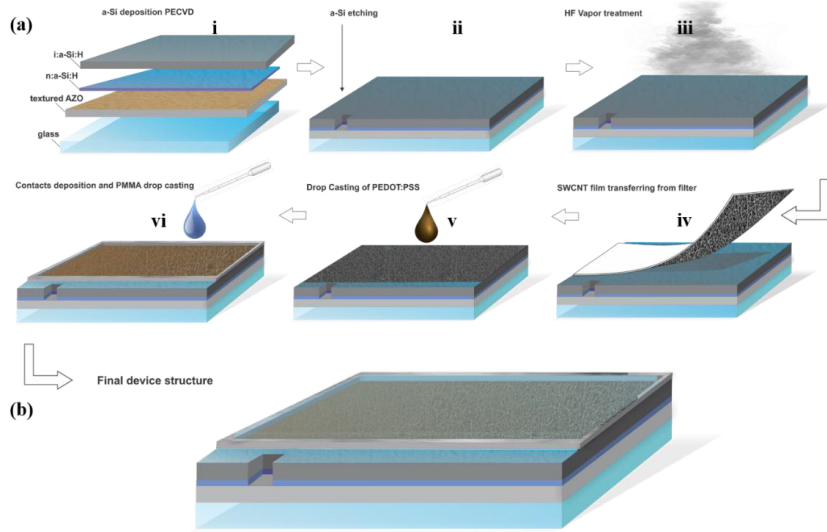


Figure 4-6. (a) Fabrication steps of the HSC process flow: (i) Obtained structure with a-Si:H absorber; (ii) Chemical local etching of a-Si:H to reach Al:ZnO back contact with KOH; (iii) HF vapor treatment of a-Si:H surface for 140 seconds to etch the native oxide; (iv) Dry transfer of SWCNTs onto a HF-treated a-Si:H surface at ambient conditions; (v) Drop-cast of PEDOT:PSS at ambient conditions; (vi) Bordering active area of HSC with silver (silver paste) and final device structure of HSC; and (b) Fabricated SWCNT/a-Si:H HSC device. Reprinted and adapted with permission from (NANOTECHNOLOGY 29 (2018) 105404 (10PP)) under a CC-BY license. Copyright (2018) IOP Publishing Ltd.

4.2.3 Solar cell characterization

Synergistic effect of SWCNT-PEDOT:PSS. The J - V characteristics of the three types of hybrid solar cells: PEDOT:PSS-SWCNT/a-Si:H, PEDOT:PSS/a-Si:H and SWCNT/a-Si:H were measured in the dark (Figure 4-7a) and under illumination (Figure 4-7b). The J - V characteristics of the best performing HSCs measured in the dark clearly reveal the diode properties of all the three types. Analyzing the dark J - V curve for all three types of solar cells showed the, PEDOT:PSS-SWCNT/a-Si:H solar cell to exhibit a higher reverse saturation current density (J_0) than the other two solar cells, while their R_{Sh} , R_s and n were nearly the same. The calculated values for the PEDOT:PSS-SWCNT/a-Si:H solar cell were $J_0 = 3.40 \pm 0.01 \times 10^{-4}$ mA/cm², $R_p = 75.0 \pm 0.5$ M Ω /cm², $R_s = 30.0 \pm 0.5$ k Ω /cm² and $n = 1.05 \pm 0.05$.

J - V curve shifts under illumination showed a typical photovoltaic behavior for all the three hybrid solar cells. However, solar cells with

PEDOT:PSS-SWCNTs and a-Si:H showed more desirable J - V characteristics than those with only PEDOT:PSS or SWCNT film. The PEDOT:PSS-SWCNT/a-Si:H solar cell exhibited a better performance: a short-circuit current-density of $J_{sc} = 3.56 \pm 0.10$ mA/cm², an open-circuit voltage of $V_{oc} = 0.803 \pm 0.003$ V, a fill factor of $FF = 54 \pm 3\%$ and a efficiency of $\eta = 1.57 \pm 0.03\%$. Whereas, for the PEDOT:PSS/a-Si:H and SWCNTs/a-Si:H solar cells the equivalent values were $J_{sc} = 3.03 \pm 0.10$ and 2.80 ± 0.10 mA/cm², $V_{oc} = 0.710 \pm 0.003$ and 0.700 ± 0.003 V, $FF = 40.4 \pm 3.0\%$ and $45.2 \pm 3.0\%$, and $\eta = 1.03 \pm 0.03\%$ and $1.10 \pm 0.03\%$, respectively (Table 4-1). It is worth noting that the fill factor and open circuit voltage of the PEDOT:PSS-SWCNT/a-Si:H hybrid solar cell exceeded that of amorphous silicon hybrid solar cells using either SWCNTs or conductive polymer [16,17,19,30,31,100]. This can be explained by the introduction of PEDOT:PSS which fills the micropores of the SWCNT film and forms a continuous contact with i-a-Si:H. This leads to the formation of coupled heterojunctions between SWCNT/i-a-Si:H and PEDOT:PSS/i-a-Si:H rather than the usual single-heterojunction between SWCNT/i-a-Si:H, as has been previously reported. Thus, in the PEDOT-SWCNT/i-a-Si:H solar cell, beyond the heterojunctions formed by PEDOT:PSS and SWCNT individually, their combined effect is more important.

EQE measurements of all the three types of hybrid solar cells are shown in Figure 4-7c. The EQE spectrum for PEDOT:PSS-SWCNT/a-Si:H shows a higher EQE saturation value of 24% than for the other two solar cells. Additionally, the SWCNT/a-Si:H solar cell shows a strong blue-shift which may arise from the strong absorbance of SWCNTs near 250 nm [54], phase shift of incident wavelength caused by stack of different refractive index materials in the solar cell. Moreover, in Figure 4.7c for SWCNTs/a-Si:H HSC, the SWCNTs film have a non-uniform contact with underneath a-Si:H creating voids, which are filled with the insertion of PEDOT:PSS in the SWCNTs network (as shown in surface morphological SEM Figure 4-5). This results in a continuous junction with improved interface and reduced recombination. This is clearly noted in Table 4-1, with higher V_{oc} values for PEDOT:PSS-SWCNT/a-Si:H HSC when compared to SWCNTs/a-Si:H or PEDOT:PSS/a-Si:H. However, all three EQE spectra of the hybrid solar cells resemble those of standard a-Si:H solar cell at wavelengths of 300-800 nm. The current densities from the EQE and J - V curves match closely for all three solar cells. The sharp decrease in the EQE beyond 700 nm can be attributed to the a-Si:H mobility gap (1.7 eV).

Combining the J - V parameters and EQE, the PEDOT:PSS-SWCNT/a-Si:H fabricated solar cell was found to exhibit a state-of-the-art fill factor and

open circuit voltage; while its current density was lower due to an increased absorption of incident photons at the PEDOT:PSS-SWCNT layer (p-layer). Hence, the p-layer needs to be optimized in order to increase absorption and photo-generation of charge carriers in the i-a-Si:H. This will potentially lead to a higher photo-generated current density and efficiency.

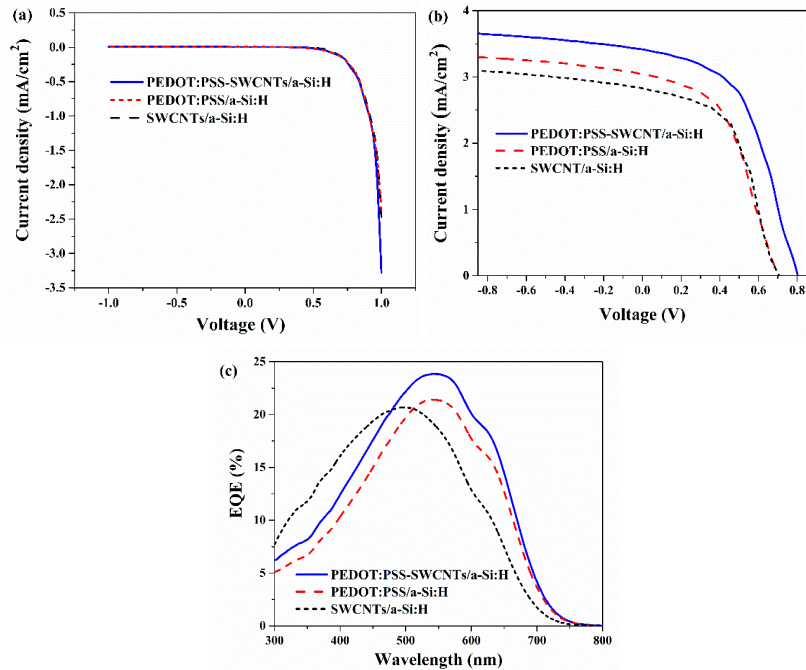


Figure 4-7. (a) dark; and (b) photo J - V characteristics of PEDOT:PSS-SWCNT/a-Si:H, PEDOT:PSS/a-Si:H and SWCNT/a-Si:H hybrid solar cells; and (c) EQE spectrum. Reprinted and adapted with permission from (PHYS. STATUS SOLIDI B 2018, 255, 1700557) under a CC-BY license. Copyright (2017) WILEY-VCH Verlag GmbH & Co. KGaA, Weinheim.

Table 4-1. J - V parameters of the fabricated solar cells: V_{oc} , J_{sc} , FF , and PCE (η).

Sample Name	V_{oc} (V)	J_{sc} (mA/cm ²)	FF (%)	η (%)
PEDOT:PSS-SWCNT/a-Si:H	0.803	3.56	54.0	1.57
PEDOT:PSS/a-Si:H	0.710	3.03	40.4	1.03
SWCNT/a-Si:H	0.700	2.80	45.2	1.10

Optimization of SWCNT-PEDOT:PSS. The J - V characteristics of HSCs fabricated with pristine SWCNTs of different thicknesses (10 nm, 20 nm, 40 nm, 60 nm, 80 nm, and 100 nm samples named CNT10, CNT20, CNT40,

CNT60, CNT80, and CNT100, respectively) are shown in Figure 4-8a and tabulated in Table 4-2. A PCE of $\eta = 2.7 \pm 0.3\%$ with a FF of $41.5 \pm 3\%$ was achieved for CNT20. As shown in Figure 4-8a, a pristine SWCNT thickness of 19 ± 1 nm was found to be the best in combination with PEDOT:PSS (50 ± 5 nm). A J_{sc} of 7.9 ± 0.1 mA/cm² and V_{oc} of 0.82 ± 0.04 V was measured. Analysis of the dark state curve shown in Figure 4-8a, resulted in $J_0 = 6.05 \pm 0.01 \times 10^{-4}$ mA/cm², the $R_p = 106.0 \pm 0.5$ M Ω /cm², the $R_s = 30 \pm 2$ k Ω /cm², and the $n = 1.10 \pm 0.05$. The high shunt resistance value together with a very low value of reverse saturation current density and series resistance led to a high PCE of the SWCNT/a-Si:H HSCs. For these measurements, the light was illuminated from the SWCNT side. Moreover, from the J - V parameters in Table 4-2, the current density was found to increase from 3.90 ± 0.02 mA/cm² for CNT10 to 7.9 ± 0.1 mA/cm² for CNT20; then to decrease for all the subsequent HSC devices with SWCNT films above 19 nm in thickness. The low current density for CNT10 can be explained by the high resistance of the SWCNTs and PEDOT:PSS. A further increase in the thickness of the SWCNT film beyond 19 nm with PEDOT:PSS yielded a lower current density induced by the decrease in transmittance of SWCNT films. It must be taken into account that the back reflection and the carrier collection on backside were provided with only an Al:ZnO layer and not with a back metal contact. This significantly deteriorated the cell efficiency.

Figure 4-8b shows the experimental EQE spectra corresponding to various SWCNT thicknesses in HSCs. It can be observed that the EQE value decreases with increase in the SWCNT films thickness, with a maximum EQE value of 42% at 514 nm obtained for CNT20. This is caused by lower absorption in the composite film (p-layer) and reduced recombination at the a-Si:H/SWCNT interface in CNT20 compared with any other sample. The current density was calculated from EQE (as described in section 3.7) for all the fabricated solar cells. The current density values of all the solar cells from the J - V curve and EQE match closely. For CNT10, CNT40, CNT60, and CNT80 the EQE dramatically decreases for wavelengths shorter than 350 nm indicating a strong surface recombination at the i:a-Si:H/SWCNT interface. A sharp fall in the EQE for all SWCNT film thickness beyond 700 nm can be attributed to the a-Si:H energy gap (1.7 eV). This spectral behavior resembles that of a-Si:H *nip* solar cells, indicating that the photo generation process goes on mainly within the i:a-Si:H.

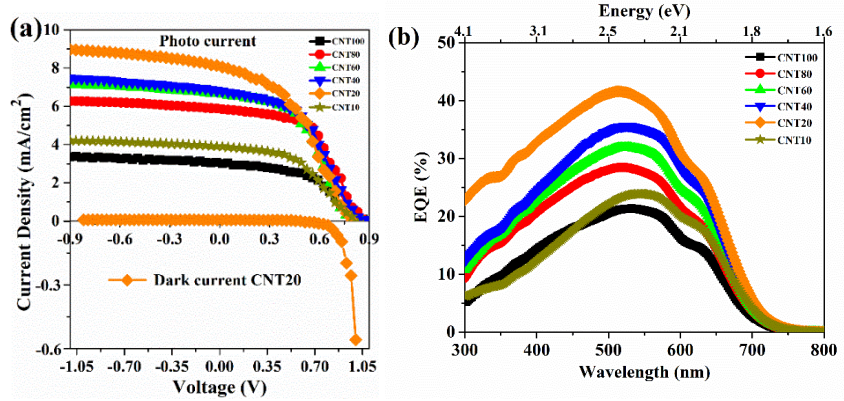


Figure 4-8. Characteristics of HSCs fabricated with SWCNT films of different thicknesses: (a) J - V curves of the photo and dark current response for CNT20; (b) EQE spectra. Reprinted and adapted with permission from (NANOTECHNOLOGY 29 (2018) 105404 (10PP)) under a CC-BY license. Copyright (2018) IOP Publishing Ltd.

Table 4-2. Comparison of J - V parameters: V_{oc} , J_{sc} , FF , and η of HSCs fabricated with SWCNT films of different thicknesses.

Sample Name	V_{oc} (V)	J_{sc} (mA/cm ²)	FF (%)	η (%)
CNT10	0.828	3.90	46.9	1.5
CNT20	0.820	7.90	41.5	2.7
CNT40	0.904	6.80	44.1	2.7
CNT60	0.896	5.90	52.3	2.8
CNT80	0.860	5.70	45.4	2.6
CNT100	0.872	3.04	48.0	1.3

The high current density of CNT20 can also account for the inherent Schottky behavior of SWCNTs due to metallic and semiconducting tubes within its network. Semiconducting SWCNTs have a work function of 4.5 eV with a band gap of 0.5 eV [53] and metallic SWCNTs with a zero bandgap [101] have a work function of nearly 5.0 eV. On forming a composite film with PEDOT:PSS, the SWCNTs network is doped thereby increasing the work function of semiconducting SWCNTs [97]. This is confirmed by the KPFM measurements of the composite film with a work function of 4.95 eV, which is close to the work function of metallic SWCNTs. When this composite film is in contact with i:a-Si:H (Fermi level position of 4.70 eV) [102], the Schottky barrier is reduced across the a-Si:H/SWCNT interface. Moreover, once the thickness of the SWCNT film increases beyond 19 nm, the transmittance decreases, which leads

to a lower absorption and reduced photo generated carriers in the i:a-Si:H. In addition, as the SWCNT film thickness increases, PEDOT:PSS is not evenly distributed along the thickness of the SWCNTs. This possibly results in two recombination centers at the SWCNTs/PEDOT:PSS and SWCNTs/a-Si:H interfaces. Thus, the concentration of the generated hole carriers is lower for CNT40, CNT60, CNT80, and CNT100. It is worth mentioning that in our approach, the optimized composite film of PEDOT:PSS and SWCNT not only increases the effective contact area of a-Si by forming a continuous heterojunction, but also stimulates the holes in PEDOT:PSS to be transferred to the interconnected SWCNT network due to the higher charge carrier mobility and low sheet resistance of SWCNTs along with their one-dimensional axis [103,104]. Thus, PEDOT:PSS and SWCNT together facilitate hole transport from a-Si as shown above in a synergistic effect of SWCNT-PEDOT:PSS. Compared to all the previously reported work [30–32], the combined effect of SWCNTs and PEDOT:PSS was utilized to attain a better and higher J-V characteristics of HSC. This also explains the state-of-the-art performance of the HSCs fabricated in our work.

PMMA as an AR layer. PMMA was used to protect the device from any surface modification under ambient conditions. PMMA has a transmittance close to 100% over a wide wavelength, where a-Si:H generates photo-induced carriers. The fabrication process shown in Figure 6 was modified and the last step of PMMA was added by drop-cast (Figure 4-6a – step vi). 2 μ l of PMMA solution was drop-cast onto the fabricated CNT20 device, so that the active area of the cell was uniformly coated. The device was placed on a hot plate at 90 °C for 20 minutes to ensure solvent evaporation.

Comparison of the J-V characteristics of a CNT20 HSC device with PMMA and without PMMA is shown in Figure 4-9a and tabulated in Table 4-3. Compared to the values reported in Table 4-2, the sample CNT20 with PMMA resulted in $\eta = 3.36 \pm 0.30\%$, $FF = 41.8 \pm 3\%$, $J_{sc} = 8.99 \pm 0.10$ mA/cm², and $V_{oc} = 0.896 \pm 0.040$ V. 10% increase in PCE, J_{sc} , and V_{oc} were observed with PMMA. The dark state curve shown in Figure 9a gives the $J_0 = 8.04 \pm 0.01 \times 10^{-4}$ mA/cm², the $R_p = 350 \pm 1$ M Ω /cm², the $R_s = 21 \pm 2$ k Ω /cm², and $n = 1.06 \pm 0.03$, i.e close to the ideal diode factor, hinting at a reduced carrier recombination. The EQE curves of CNT20 with and without PMMA are shown in Figure 4-9b. The EQE value saturates at 47.1% demonstrating an increase of almost 10%, compared to the device without PMMA. The EQE response is significantly enhanced for a wavelength range from 320 to 640 nm. A sharp increase in the EQE value with

PMMA from 24% at 318 nm to 47% at 500 nm indicates an enhanced light absorption and photo generation in the i-a-Si:H.

Furthermore, the use of PMMA as an AR coating and encapsulant has been a topic of interest and several works have focused on the use of a PMMA layer acting as a broad band ARC over Si-CNT solar cells [105–107]. Hence, diffuse reflectance measurements were carried out to test the effect of PMMA as an ARC in our solar cell. The reflectance spectra of plain a-Si:H, a-Si:H with SWCNTs, a-Si:H with PEDOT:PSS, HSC without PMMA, and HSC with PMMA are shown in Figure 4-9c. The a-Si:H surface with textures exhibits about 20% minimum reflectance ranging from 500–800 nm. The reflection minima of the HSC without PMMA are slightly lower than those of plain a-Si:H, at about 16% in the visible region. The minimum reflectance of a-Si:H with PEDOT:PSS and a-Si:H with SWCNTs is lower than that of plain a-Si:H and is similar to the reflectance of HSC without PMMA. Further, HSC with PMMA shows a reduction to about 4.5% reflectance in the visible region. Consequently, PMMA as an effective ARC increases the light trapping efficiency, producing more photogenerated carriers and thus increasing the current density and HSC efficiency.

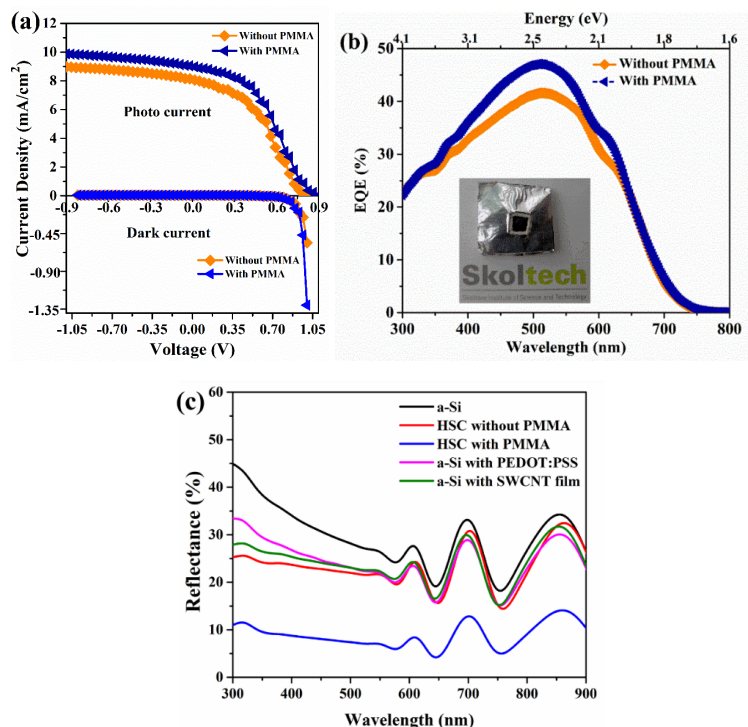


Figure 4-9. Characteristics of HSCs fabricated with CNT20 sample: **(a)** *J-V* curve comparison without and with PMMA for photo and dark current response; **(b)** EQE spectra comparison without and with PMMA; and **(c)** Reflectance spectra of plain a-Si:H, HSC without PMMA, HSC with PMMA, a-

Si:H with PEDOT:PSS, and a-Si:H with SWCNT film. Reprinted and adapted with permission from (NANOTECHNOLOGY 29 (2018) 105404 (10PP)) under a CC-BY license. Copyright (2018) IOP Publishing Ltd.

Table 4-3. Comparison of J - V parameters of HSC fabricated with CNT20 sample without and with PMMA.

Conditions	V_{oc}	J_{sc}	FF	η
	(V)	(mA/cm²)	(%)	(%)
without PMMA	0.820	7.90	41.5	2.70±0.01
with PMMA	0.896	8.99	41.8	3.40±0.01

4.3 Rational design of p-type transparent conductor (Publication 4)

The goal of this section is to utilize the findings of Section 4.2 on the SWCNT-PEDOT:PSS composite and design a novel p-type TCF using MoO₃, doping of the SWCNT film and to introduce SWCNT fibers as potential replacement for traditional metal contacts. This results in a state-of-the-art TCF in a systematic comparison of the optical, electrical, and mechanical properties of different TCF configurations. Finally, HSCs are fabricated introducing a buffer layer between i-a-Si:H/SWCNT-PEDOT:PSS composite and using different TCF configurations: TCF1, TCF2, TCF3, and TCF4.

4.3.1 TCF and solar cell fabrication

Aerosol synthesized SWCNT films were utilized for this work. The doping of SWCNT films was performed using spin-casting of a 15 mM HAuCl₄ solution in ethanol [54]. Thin MoO₃ interlayers of about 4 nm were deposited using a thermal evaporation technique in a vacuum at room temperature. Furthermore, a SWCNTs-PEDOT:PSS composite was formed by spin-casting of an electrically conductive PEDOT:PSS on SWCNT films as detailed in Section 4.2. PMMA solution (4 wt.%) in anisole was spin-casted on SWCNT fibers to form the AR layer as detailed in Section 4.2.3.

SWCNT fibers. To utilize the exceptional electrical properties of SWCNTs, the original films were transformed to form self-similar top fiber electrodes. SWCNT films were dry-transferred onto a cleaned glass surface. A drop of IPA was drop-cast on the SWCNT films. The wet film was carefully lifted to make long and narrow SWCNT fibers. Solvent evaporation shrinks the film into a dense fiber (fabrication process is shown in Figures 4-10a-d with a width of 60 to 100 μm after being placed on top of SWCNTs-MoO₃-PEDOT:PSS composite film in a wet-state as shown in Figure 4-10e-f. SWCNTs utilized for

fibers and films were synthesized under the same conditions. Then the wet fiber was placed onto the composite surface and dried to make a conformal contact to the underlying SWCNTs-MoO₃-PEDOT:PSS composite film as seen from Figure 4-10e-f. This flattened shape builds a strong van der Waals interaction between the SWCNT fibers and the composite film, induced by their self-similar structure, thereby completing the TCF.

Solar cell fabrication. For solar cell fabrication, 10×10 cm² commercial glass substrates coated with 700 nm textured Al:ZnO as the back contact were used. Both an n-doped a-Si:H layer and intrinsic i-a-Si:H absorber were subsequently grown over the Al:ZnO layer in a multichamber PECVD system von Ardenne CS-400PS at 13.56 MHz as detailed in Section 4.2 [98,108]. After that the substrate was cut into 2.5×2.5 cm² individual samples for device fabrication. SWCNT films and fiber top electrodes on a-Si:H (i) define the working area (1 cm²) of the individual cells. The reference sample was fabricated with a conventional 10 nm p-a-Si window layer and a 90 nm ITO front electrode. The SWCNT/a-Si:H hybrid solar cells were fabricated as described in detail in Section 4.2.2. In brief, partially fabricated a-Si:H thin film solar cells till intrinsic layer were utilized. Ultra-thin MoO₃ (4 nm) was thermally evaporated on a-Si:H (i). Different configurations of developed TCFs (TCF1, TCF2, TCF3 and TCF4) were deposited onto MoO₃ under ambient conditions as a p-type window layer and front electrode to complete the device architecture shown in Figure 4-10e.

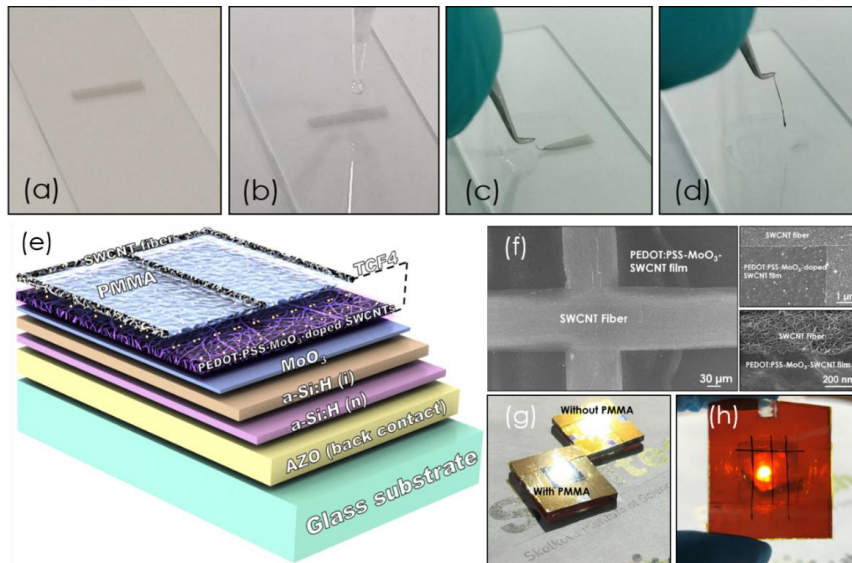


Figure 4-10. SWCNT fiber fabrication process using wet-pulling technique: **(a)** Dry transferred SWCNT film on glass surface; **(b)** Drop-cast of isopropyl alcohol (IPA); **(c)** Self-shrinking of SWCNT film; **(d)** SWCNT fiber formation under the IPA evaporation; **(e)** Solar cell architecture with newly developed transparent electrode TCF4 (from bottom to top): Glass/Al:ZnO/a-Si:H (n)/a-Si:H (i)/MoO₃/SWCNT doped-MoO₃-PEDOT:PSS/SWCNT fibers doped/PMMA; **(f)** SEM images of SWCNT fibers showing a cross point of two fibers on a cell surface, the PEDOT:PSS-MoO₃-doped SWCNTs composite film and good contact between the composite film and fiber crossed on the cell surface uniformly; **(g)** Fabricated solar cells (with and without PMMA) exposed to sun showing the anti-reflective effect with PMMA coating; and **(h)** Photograph of the fabricated solar cell on a-Si using developed TCF showing its transparency. Reprinted and adapted with permission from (NANO ENERGY 67 (2020) 104183) under a CC-BY license. Copyright (2019) ELSEVIER Ltd.

4.3.2 Optical, electrical, and mechanical properties

All the ingredients utilized to build the p-type multilayer TCFs are listed in Table 4-4. SWCNT films were created using a dry-transfer technique [53], the SWCNT fibers were wet pulled from the film as described above. For doping of the SWCNT films and fibers, H₂AuCl₄ ethanol solution was used. PEDOT:PSS layer was deposited onto SWCNT by a spin-casting technique. MoO₃ was deposited by a thermal evaporation method. The PMMA layer was spin casted onto the surface of the SWCNT fibers.

The surface morphologies of the pristine SWCNT, MoO₃-SWCNT, SWCNTs-MoO₃-PEDOT:PSS and SWCNTs doped -MoO₃-PEDOT:PSS films are shown in Figures 4-11a-d. When deposited onto porous SWCNTs, PEDOT:PSS impregnates the film, which leads to the formation of a homogeneous composite material with a smooth surface. Each successive component added to the composite affected both its optical and electrical properties as shown in Table 4-4. The original SWCNT films had a transmittance of 87% at 550 nm (Figure 4-11e), whereas that of the fiber shrunk from the same SWCNT film was much lower (~2.0%). The reason for the difference is that during the process of being picked up and layed down, the film condensed into a narrow dense fiber with overlapping nanotube bundles depleting most of the incident light (Figure 4-11). Also, for comparison, the optical transmission of PMMA, doped SWCNT film and fiber, SWCNT-MoO₃ and different TCFs (TCF1, TCF2, TCF3 and TCF4 as in Table 4-4) are shown in Figure 4-11. The conductivities (σ in S cm⁻¹) of the SWCNT film and SWCNT fiber were 0.15±0.02 S cm⁻¹ and 62.00±7.20 S cm⁻¹ respectively, demonstrating the excellent conductivity of the SWCNT fiber. The doped SWCNT films and SWCNT fibers showed a substantial increase in conductivity to 0.51±0.06 S cm⁻¹ and 100.00±11.60 S cm⁻¹, respectively. The equivalent sheet resistance (at a transmittance of 90%) [109] of pristine SWCNT film was 364 Ω/sq. Doping of the SWCNT film by HAuCl₄ reduced the transmittance value by 2.6%, but also decreased the equivalent sheet resistance to 104 Ω/sq. Similarly, spin casting of PEDOT:PSS on top of the SWCNTs led to a decrease in both the transmittance and sheet resistance of the resulted film. A composite structure containing doped SWCNTs, MoO₃ and PEDOT:PSS revealed a transmittance of 81.2% with an equivalent sheet resistance of 65 Ω/sq. Enhanced optoelectrical properties were observed after SWCNT fibers were added on top of the composite (in a 3 bus bar (3BB) configuration with a distance between parallel fibers of 3 mm as shown in Figures 4-10 and 4-11f), lowering the equivalent sheet resistance to 28 Ω/sq for the non-doped stack SWCNTs-PEDOT:PSS/SWCNT fibers (TCF1). This highlights the fact that SWCNT fibers can also be substituted for traditional metal contacts owing to their high conductivity and simple deposition process as demonstrated here. The deposition of MoO₃ onto the SWCNT surface (TCF2) before adding PEDOT:PSS dropped the value to 22 Ω/sq. A similar observation was reported in several studies indicating that MoO₃ is a stable dopant to SWCNTs [110–112]. A record equivalent sheet resistance of 17 Ω/sq was achieved for a complete structure consisting of HAuCl₄ doped SWCNTs with MoO₃ and PEDOT:PSS covered by doped SWCNT fibers (TCF3). To the best of our knowledge, this is

the state-of-the-art equivalent sheet resistance for a transparent electrode based on randomly oriented SWCNT films and for any transparent p-type conductors [113].

Mechanical properties of TCF. The developed transparent p-type conductor showed a high degree of mechanical flexibility in an in-house developed bending setup. The TCF3 on a PI substrate was subjected to 50 000 bending cycles (at bending angles of 20°, 45°, 90° and 180°, which corresponded to radii of curvature of 10, 6.5, 4.5 and 1.6 mm⁻¹). The resistance of the electrodes increased to 0.65 – 5.15%, respectively, and became stable after 23 000 – 40 000 cycles as shown in Figure 4-11g.

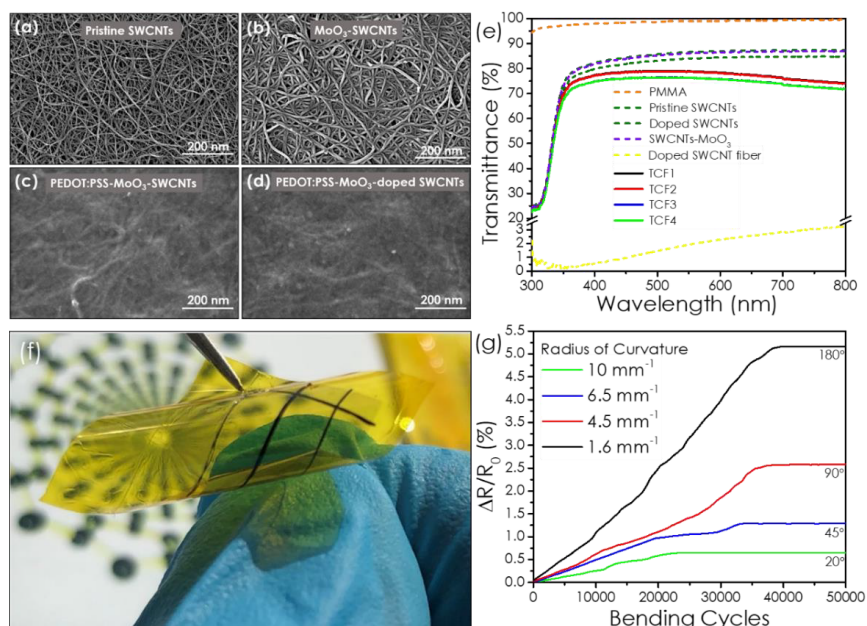


Figure 4-11. Surface morphology of various types of electrodes: **(a)** Pristine SWCNTs; **(b)** MoO₃-SWCNTs; **(c)** PEDOT:PSS-MoO₃-SWCNTs composite; and **(d)** PEDOT:PSS-MoO₃-doped SWCNTs composite. **(e)** Optical transmittance of individual components for the TCFs: pristine and doped SWCNT films, SWCNT+MoO₃, PMMA, and different types of TFCs: TCF1, TCF2, TCF3 and TCF4. For comparison the transmittance spectra of SWCNT fiber and SWCNT fiber doped are also presented; **(f)** A photograph of TCF3 on a polyimide substrate; and **(g)** TCF4 resistance change during 50 000 bending cycles at angles of 20°, 45°, 90° and 180° with the radii of curvature from 10 to 1.6 in mm⁻¹. Reprinted and adapted with permission from (NANO ENERGY 67 (2020) 104183) under a CC-BY license. Copyright (2019) ELSEVIER Ltd.

Table 4-4. Description and comparison of transmittance (%), conductivity, σ ($S\text{ cm}^{-1}$), sheet resistance R_s (Ω/sq) and equivalent sheet resistance R_{90} (Ω/sq) of pristine SWCNT film, doped SWCNT film, SWCNT-MoO₃, SWCNT-PEDOT:PSS, SWCNT-MoO₃-PEDOT:PSS, SWCNT-MoO₃-PEDOT:PSS, SWCNT doped-MoO₃-PEDOT:PSS, SWCNT fiber, doped SWCNT fiber, TCF1, TCF2, TCF3 and TCF4.

Sample Name	Structure description	T (%)	σ ($S\text{ cm}^{-1}$)	R_{sh} (Ω/sq)	R_{90} (Ω/sq)
SWCNT film	Thin film of SWCNTs	86.6	0.15 ± 0.02	128 ± 5.0	364
Doped SWCNT film	Spin-casting of HAuCl ₄ on SWCNT film.	84.0	0.51 ± 0.06	37 ± 2.0	104
SWCNT-MoO ₃	Thermal evaporation of MoO ₃ on SWCNT film.	86.2	0.21 ± 0.02	112 ± 3.0	312
SWCNT-PEDOT:PSS	Spin-casting of PEDOT:PSS	84.6	0.59 ± 0.07	76 ± 3.5	205
SWCNT-MoO ₃ -PEDOT:PSS	Composite structure	83.8	1.00 ± 0.11	49 ± 2.2	123
SWCNT doped-MoO ₃ -PEDOT:PSS	CNT doped composite structure	81.2	1.82 ± 0.20	27 ± 1.1	65
SWCNT fiber	Narrow fibers from SWCNT film	2.0	62.00 ± 7.20	-	-
Doped SWCNT fiber	Fibers doped with HAuCl ₄	1.9	100.0 ± 11.6	-	-
TCF1	SWCNTs-PEDOT:PSS/SWCNT fibers	78.9	12.42 ± 1.37	12.0 ± 0.8	28
TCF2	SWCNTs-MoO ₃ -PEDOT:PSS/SWCNT fibers	78.7	14.90 ± 1.64	10.0 ± 0.4	22
TCF3	SWCNTs doped with HAuCl ₄ -MoO ₃ -PEDOT:PSS/SWCNT fibers doped with HAuCl ₄	76.3	24.83 ± 2.73	6.0 ± 0.3	17
TCF4	SWCNTs doped with HAuCl ₄ -MoO ₃ -PEDOT:PSS/SWCNT fibers doped/PMMA	76.3	24.83 ± 2.73	6.0 ± 0.3	17

4.3.3 Solar cell characterization

To demonstrate the applicability of the developed TCFs, the material was tested as a p-type window layer and a front electrode in hybrid solar cells based on amorphous silicon (the fabricated device picture and the schematics are shown in Figures 4-10). Furthermore, for better extraction of charge carriers and alignment of bands in the solar cell layers, a supplemental ultra-thin MoO₃ layer was added on the a-Si:H(i) surface as both a passivation buffer layer and high work function hole selective contact. The J - V characteristics of four different cell types under AM 1.5 and dark conditions are shown in Figures 4-12a and tabulated in Table 4-5. Typical photovoltaic behavior was observed for all types with good correlations between experiments and numerical simulations carried out using AFORS-HET (automat for simulation of heterostructures) software. The TCF1 solar cell J - V curve exhibited S-shape behavior with improved short-circuit current density of $J_{sc} = 11.93 \text{ mA cm}^{-2}$ compared to a solar cell without MoO₃ (Figure 4-12b), open-circuit voltage of $V_{oc} = 0.795 \text{ V}$, and fill factor of $FF = 41.3\%$, resulting in $PCE = 3.9\%$.

Subsequently, the TCF2 configuration with MoO₃ on the SWCNT film exhibited $J_{sc} = 12.63 \text{ mA cm}^{-2}$, $V_{oc} = 0.800 \text{ V}$, and $FF = 51.1\%$ ($PCE = 5.1\%$) with no S-shape and elevated photo and dark currents (Figure 4-12a) indicating lower junction and TCF2 resistance (Table 4-4 and Table 4-6).

TCF3 cell showed an ideal J - V curve with $J_{sc} = 12.83 \text{ mA cm}^{-2}$, improved $V_{oc} = 0.870 \text{ V}$ and significantly increased $FF = 67.4\%$, resulting in $PCE = 7.5\%$. In the TCF3, doping of the SWCNT films and fibers increases the conductivity of the electrode owing to the reduced Schottky barrier between semiconducting and metallic SWCNTs [56] and increase in the hole concentration, which yields a significant improvement in the short-circuit current and a drop in series resistance (Table 4-5 and 4-6).

Finally, TCF4 devices demonstrated improved characteristics of $J_{sc} = 14.11 \text{ mA cm}^{-2}$, $V_{oc} = 0.907 \text{ V}$, and $FF = 68.0\%$, leading to a record $PCE = 8.3\%$ with a diode ideality factor $n = 1.02$ (Table 4-6). The increase in the short-circuit current is mainly due to the AR effect of PMMA leading to higher photo-generation current in the a-Si:H layer. Introducing a plain aluminum coated reflective mirror on the back side of the TCF4 solar cell further increased the current density to $J_{sc} = 15.03 \text{ mA cm}^{-2}$ (Figure 4-12c) and exceeded the state-of-the-art $PCE = 8.8\%$, proving that internal reflection from the back reflector to the cell core further contributes into the increase in absorption by the a-Si:H layer. For comparison, the J - V curves of the latter device and the standard reference solar cell (with boron-doped a-Si:H p-type layer and metal contacts)

are shown in Figure 4-12d. A 16% (a net 1.4%) efficiency improvement was seen after integrating the newly developed transparent electrode into the nip-configured a-Si:H solar cell instead of the conventional p-a-Si / TCO front window layer stack. It is to be noted that the reference cells are produced at substrate temperatures less than 200 °C, without any back reflector, texturing and other special processes as carried out for record a-Si:H solar cells.

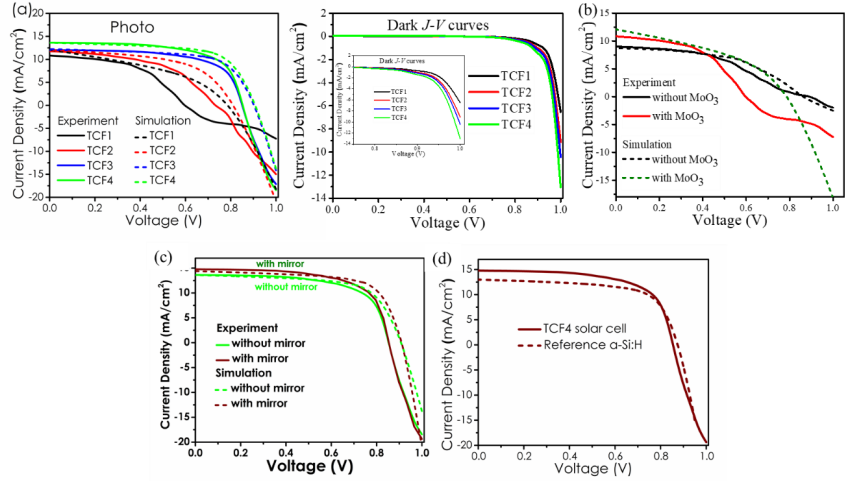


Figure 4-12. Comparison of experimental data and simulations of **(a)** photo and dark J-V curves; **(b)** photo J-V curves with and without MoO₃; **(c)** photo J-V curves with and without Mirror; and **(d)** J-V curves of TCF4 solar cell and standard reference a-Si:H solar cell. Reprinted and adapted with permission from (NANO ENERGY 67 (2020) 104183) under a CC-BY license. Copyright (2019) ELSEVIER Ltd.

Table 4-5. Comparison of experimental J-V parameters of the fabricated solar cells with different TFCs, the standard reference a-Si:H solar cell and the solar cell without MoO₃: V_{oc} , J_{sc} , FF, and η of the fabricated solar cells.

Sample	V_{oc} (V)	J_{sc} (mA/cm ²)	FF (%)	η (%)
TCF1	0.795 ± 0.024	11.93 ± 0.36	41.3 ± 1.2	3.90 ± 0.2
TCF2	0.800 ± 0.024	12.63 ± 0.38	51.1 ± 1.5	5.10 ± 0.2
TCF3	0.870 ± 0.026	12.83 ± 0.39	67.4 ± 2.0	7.50 ± 0.2
TCF4	0.907 ± 0.027	14.11 ± 0.42	68.0 ± 2.0	8.30 ± 0.3
TCF4 with mirror	0.909 ± 0.027	15.03 ± 0.45	68.2 ± 2.0	8.80 ± 0.3
Reference a-Si:H	0.874 ± 0.020	12.90 ± 0.32	66.5 ± 1.5	7.50 ± 0.1
Without MoO ₃	0.820 ± 0.023	7.90 ± 0.33	41.5 ± 0.9	2.70 ± 0.1

Table 4-6. Calculated n , device R_{sr} and R_{sh} of the fabricated solar cells.

Sample	N	R_{sr} ($\Omega \text{ cm}^2$)	R_{sh} ($\Omega \text{ cm}^2$)
TCF1	1.10	10.0 \pm 1.5	175 \pm 30
TCF2	1.04	6.0 \pm 1.0	500 \pm 85
TCF3	1.03	3.0 \pm 0.5	1000 \pm 171
TCF4	1.02	3.0 \pm 0.5	1120 \pm 192
TCF4 with mirror	1.02	3.0 \pm 0.5	1120 \pm 192

The EQE of all solar cell types was measured. Figure 4-13a shows that the EQE value saturated at 75% for the TCF1 and nearly 80% for the TCF2 and TCF3 solar cells in the range from 300 to 800 nm, corresponding to the a-Si:H light absorption wavelength range. This results in an increase in the absolute EQE value by 30% compared to a solar cell without a MoO₃ layer (Figure 4-13b). Increased EQE indicates a reflection drop in the window layer [29], leading to enhanced photocurrent generation (Table 4-7). Moreover, MoO₃ work function (6.5 eV) is higher than that of SWCNTs (4.45 eV), which might lead to additional p-type doping [114]. A drop in the series resistance from 10 $\Omega \text{ cm}^2$ (TCF1) to 6 and 3 $\Omega \text{ cm}^2$ (for TCF2 and TCF3, respectively) proves the rise of the hole concentration in the SWCNTs coated by MoO₃ (Table 4-6 and Table 4-4). In contrast, the TCF4 solar cell with PMMA exhibited an increase in the EQE value saturated at around 90%, indicating a reduced reflection. Introducing a reflective rear mirror on the back side of a TCF4 solar cell results in broader EQE spectra for wavelengths over 500 nm as shown in Figure 4-13c, clearly demonstrating increased absorption and better optical control in the a-Si:H layer. Also, for comparison the EQE spectra of a standard a-Si:H reference and TCF4 solar cells with reflective mirror is shown in Figure 4-13d. The J_{sc} calculated from EQE spectra and J - V parameters for all the solar cell types are in very good agreement with the experiment as shown in Table 4-7, thus validating the performance of all solar cells with the developed transparent conductors.

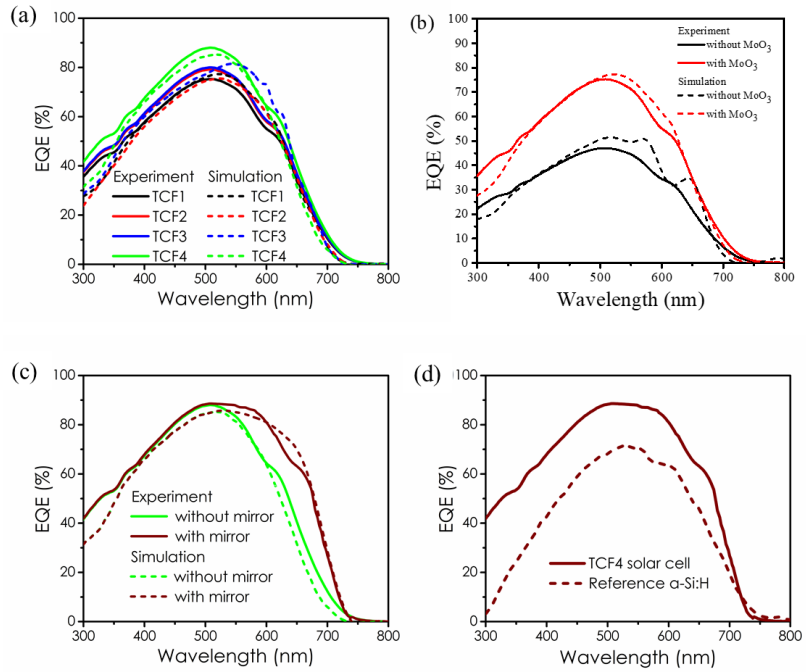


Figure 4-13. Comparison of experimental data and simulations of (a) EQE spectra of respective TCF solar cells; (b) EQE spectra of without and with MoO₃; (c) EQE spectra of without and with mirror; and (d) EQE spectra of TCF4 solar cell and standard reference a-Si:H solar cell. Reprinted and adapted with permission from (NANO ENERGY 67 (2020) 104183) under CC-BY license. Copyright (2019) ELSEVIER Ltd.

Table 4-7. Comparison of J_{sc} from J - V and EQE curves of the fabricated TCF solar cells and the standard reference a-Si:H solar cell.

Sample	J_{sc} (mA/cm ²) from J - V curves	J_{sc} (mA/cm ²) from EQE
TCF1	11.93 ± 0.36	11.80 ± 0.36
TCF2	12.63 ± 0.38	12.55 ± 0.38
TCF3	12.83 ± 0.39	12.77 ± 0.39
TCF4	14.11 ± 0.42	14.09 ± 0.42
TCF4 with mirror	15.03 ± 0.45	14.97 ± 0.45
Reference a-Si:H	12.90 ± 0.32	11.90 ± 0.32

5. Conclusion and future work

This thesis focusses on the fabrication of hybrid solar cells using SWCNTs film and a-Si:H. The work commenced by investigating the major factors that influence SWCNT film adhesion to various substrate materials. A quantitative evaluation of the SWCNT film adhesion force in air and inert Ar atmospheres with various materials including SiO₂, ITO, Si, a-Si:H, ZrO₂, Pt, PDMS, and SWCNTs for self-adhesion deposited directly on the AFM tips was measured. Quantitative values were derived for the adhesion force from the force-distance curves by estimating the tip-surface contact area according to the Hertz model. Adhesion was found to be greatly influenced by environmental conditions and by surface functionalization. SWCNT thin films have better adhesion in an inert atmosphere. A simple fluorination process greatly improves adhesion, which is affected by sample storage and deposition in ambient air.

This improved understanding of SWCNT film adhesion prompted us to combine it with PEDOT:PSS thus forming a SWCNTs-PEDOT:PSS composite. The PEDOT:PSS not only filled the micropores but also improved the surface roughness of the SWCNTs. This resulted in a low cost and environmentally friendly fabrication method for hybrid solar cells using SWCNT films and a-Si:H. The window layer and top electrode of this solar cell resulted from the synergistic effect of SWCNTs and PEDOT:PSS forming a composite p-type by simple dry-transfer and spin-casting techniques. The SWCNT-PEDOT:PSS composite p-type with enhanced conductivity provided a continuous hybrid heterojunction with a-Si:H. HSC efficiency increased slightly from 1.6% to 2.7%. A further increase upto 3.4% was recorded by introducing PMMA as an anti-reflective layer. Although significant progress was made in terms of SWCNTs/a-Si:H hybrid solar cell performance, their diode characteristics were still not ideal due to the low conductivity of the SWCNTs-PEDOT:PSS composite and poor p/i interface. This prompted further optimization of the SWCNTs-PEDOT:PSS composite film as a p-type transparent conductor.

Finally, a rational design was proposed for a novel highly efficient flexible transparent p-type conductor, combining the superior properties of doped SWCNTs with PEDOT:PSS, MoO₃ and SWCNT fiber grids into a single

composite material. The use of thin multicomponent layers and the introduction of high-conductive SWCNT fibers resulted in a dramatic improvement of nearly 58% in sheet resistance compared to the previous state-of-the-art in p-type TCF development. As demonstrated here, SWCNT fibers can be used to replace traditional metal contacts due to their high conductivity and simple deposition process. A configuration of SWCNTs-MoO₃-PEDOT:PSS/SWCNT fibers resulted in a record equivalent sheet resistance of R_{sq} of 17 Ω/sq with a transmittance of 90%, and superior bendability. As a demonstration, the TCFs were used as a combined window layer and front electrode to form hybrid thin film solar cells with an amorphous silicon absorber. An outstanding current of $J_{\text{sc}} = 15.03 \text{ mA}/\text{cm}^2$ and a record PCE = 8.8% for such thin film solar cells led to an effective 18% improvement over a conventional nip-configured a-Si:H solar cells.

These results are among the best thin film HSCs achieved for SWCNT film and a-Si:H, providing strong evidence that SWCNT-MoO₃-PEDOT:PSS composite p-type films with SWCNT fibers are potential as hole transport window layers and transparent electrodes. It is envisaged that the outcomes of this work will secure the future development of novel p-type TCFs in combination with the use of pure high quality semiconducting or metallic SWCNTs that are aligned with better passivation, improved doping stability of SWCNTs, light trapping schemes and nanostructuring that can potentially improve future photovoltaic devices. Nevertheless, the applications of the novel p-type composite material are not limited to solar cells. Rational design and room-temperature processing broaden the horizon for transparent and flexible electrode implementation in diverse applications in other fields of science and technology.

References

- [1] United Nations. World Population Prospects 2019. 2019.
- [2] World Urbanization Prospects: The 2018 Revision. 2019. <https://doi.org/10.18356/b9e995fe-en>.
- [3] Energy Information Administration. International Energy Outlook. Outlook 2019. <https://doi.org/https://www.eia.gov/outlooks/ieo/pdf/ieo2019.pdf>.
- [4] IRENA. Renewable Energy Statistics 2019. 2019.
- [5] REN 21 Renewables Now. Renewables Global Status Report 2019. 2019.
- [6] Louw A, Boyle R, Strahan D, Collins B, Kimmel M, Giannakopoulou E, et al. Global Trends in Renewable Energy Investment 2018. Bloom New Energy Financ 2018. <https://doi.org/10.3928/00220124-20081201-03>.
- [7] OECD/IEA. World Energy Outlook 2018: Electricity. 2018.
- [8] Green MA, Dunlop ED, Hohl-Ebinger J, Yoshita M, Kopidakis N, Ho-Baillie AWY. Solar cell efficiency tables (Version 55). Prog Photovoltaics Res Appl 2020. <https://doi.org/10.1002/pip.3228>.
- [9] Yoshikawa K, Kawasaki H, Yoshida W, Irie T, Konishi K, Nakano K, et al. Silicon heterojunction solar cell with interdigitated back contacts for a photoconversion efficiency over 26%. Nat Energy 2017. <https://doi.org/10.1038/nenergy.2017.32>.
- [10] Stuckelberger M, Biron R, Wyrsh N, Haug FJ, Ballif C. Review: Progress in solar cells from hydrogenated amorphous silicon. Renew Sustain Energy Rev 2017. <https://doi.org/10.1016/j.rser.2016.11.190>.
- [11] Shah AV. Thin-film silicon solar cells. 2010. <https://doi.org/10.1201/b16327>.
- [12] Williams EL, Jabbour GE, Wang Q, Shaheen SE, Ginley DS, Schiff EA. Conducting polymer and hydrogenated amorphous silicon hybrid solar cells. Appl Phys Lett 2005. <https://doi.org/10.1063/1.2136409>.
- [13] Gowrishankar V, Scully SR, McGehee MD, Wang Q, Branz HM. Exciton splitting and carrier transport across the amorphous-silicon/ polymer solar cell interface. Appl Phys Lett 2006. <https://doi.org/10.1063/1.2408641>.
- [14] Avasthi S, Lee S, Loo YL, Sturm JC. Role of majority and minority carrier barriers silicon/organic hybrid heterojunction solar cells. Adv Mater 2011. <https://doi.org/10.1002/adma.201102712>.
- [15] Jeong S, Garnett EC, Wang S, Yu Z, Fan S, Brongersma ML, et al. Hybrid silicon nanocone-polymer solar cells. Nano Lett 2012. <https://doi.org/10.1021/nl300713x>.
- [16] Pei Z, Thiyagu S, Jhong MS, Hsieh WS, Cheng SJ, Ho MW, et al. An amorphous silicon random nanocone/polymer hybrid solar cell. Sol Energy Mater Sol Cells 2011. <https://doi.org/10.1016/j.solmat.2011.04.021>.
- [17] Yun MH, Jang JH, Kim KM, Song HE, Lee JC, Kim JY. A hybrid solar cell

- fabricated using amorphous silicon and a fullerene derivative. *Phys Chem Chem Phys* 2013. <https://doi.org/10.1039/c3cp53493f>.
- [18] Liu R, Lee ST, Sun B. 13.8% Efficiency Hybrid Si/Organic Heterojunction Solar Cells with MoO₃ Film as Antireflection and Inversion Induced Layer. *Adv Mater* 2014. <https://doi.org/10.1002/adma.201402076>.
- [19] Schaefer S, Albrecht S, Neher D, Schulze TF, Conrad E, Korte L, et al. Electric Field Distribution in Hybrid Solar Cells Comprising an Organic Donor Polymer and Amorphous Silicon. *Org Photonics Photovoltaics* 2014. <https://doi.org/10.2478/oph-2014-0004>.
- [20] Angmo D, Krebs FC. Flexible ITO-free polymer solar cells. *J Appl Polym Sci* 2013. <https://doi.org/10.1002/app.38854>.
- [21] Kim J, Hong Z, Li G, Song T Bin, Chey J, Lee YS, et al. 10.5% efficient polymer and amorphous silicon hybrid tandem photovoltaic cell. *Nat Commun* 2015. <https://doi.org/10.1038/ncomms7391>.
- [22] Tan H, Furlan A, Li W, Arapov K, Santbergen R, Wienk MM, et al. Highly Efficient Hybrid Polymer and Amorphous Silicon Multijunction Solar Cells with Effective Optical Management. *Adv Mater* 2016. <https://doi.org/10.1002/adma.201504483>.
- [23] Lu S, Sun Y, Ren K, Liu K, Wang Z, Qu S. Recent development in ITO-free flexible polymer solar cells. *Polymers (Basel)* 2017. <https://doi.org/10.3390/polym10010005>.
- [24] Jäckle S, Liebhaber M, Gersmann C, Mews M, Jäger K, Christiansen S, et al. Potential of PEDOT:PSS as a hole selective front contact for silicon heterojunction solar cells. *Sci Rep* 2017. <https://doi.org/10.1038/s41598-017-01946-3>.
- [25] Jeon I, Xiang R, Shawky A, Matsuo Y, Maruyama S. Single-Walled Carbon Nanotubes in Emerging Solar Cells: Synthesis and Electrode Applications. *Adv Energy Mater* 2019. <https://doi.org/10.1002/aenm.201801312>.
- [26] Jeon I, Matsuo Y, Maruyama S. Single-Walled Carbon Nanotubes in Solar Cells. *Top Curr Chem* 2018. <https://doi.org/10.1007/s41061-017-0181-0>.
- [27] Jariwala D, Sangwan VK, Lauhon LJ, Marks TJ, Hersam MC. Carbon nanomaterials for electronics, optoelectronics, photovoltaics, and sensing. *Chem Soc Rev* 2013. <https://doi.org/10.1039/c2cs35335k>.
- [28] Xu W, Wu S, Li X, Zou M, Yang L, Zhang Z, et al. High-Efficiency Large-Area Carbon Nanotube-Silicon Solar Cells. *Adv Energy Mater* 2016. <https://doi.org/10.1002/aenm.201600095>.
- [29] Wang F, Kozawa D, Miyauchi Y, Hiraoka K, Mouri S, Ohno Y, et al. Considerably improved photovoltaic performance of carbon nanotube-based solar cells using metal oxide layers. *Nat Commun* 2015. <https://doi.org/10.1038/ncomms7305>.
- [30] Schriver M, Regan W, Loster M, Zettl A. Carbon nanostructure-aSi:H photovoltaic cells with high open-circuit voltage fabricated without dopants. *Solid State Commun* 2010;150:561-3.

- <https://doi.org/10.1016/j.ssc.2010.01.013>.
- [31] Del Gobbo S, Castrucci P, Scarselli M, Camilli L, De Crescenzi M, Mariucci L, et al. Carbon nanotube semitransparent electrodes for amorphous silicon based photovoltaic devices. *Appl Phys Lett* 2011;98:1–4. <https://doi.org/10.1063/1.3588352>.
- [32] Funde AM, Nasibulin AG, Syed HG, Anisimov AS, Tsapenko A, Lund P, et al. Carbon nanotube-amorphous silicon hybrid solar cell with improved conversion efficiency. *Nanotechnology* 2016. <https://doi.org/10.1088/0957-4484/27/18/185401>.
- [33] Publications B, A Jorio; G Dresselhaus; M S Dresselhaus. *Topics in Applied Physics Volume 111*. vol. 111. 2008.
- [34] Iijima S, Ichihashi T. Single-shell carbon nanotubes of 1-nm diameter. *Nature* 1993. <https://doi.org/10.1038/363603a0>.
- [35] Wright M, Uddin A. Organic-inorganic hybrid solar cells: A comparative review. *Sol Energy Mater Sol Cells* 2012. <https://doi.org/10.1016/j.solmat.2012.07.006>.
- [36] Alet P-J, Palacin S, Roca I Cabarrocas P, Kalache B, Firon M, de Bettignies R. Hybrid solar cells based on thin-film silicon and P3HT. *Eur Phys J Appl Phys* 2006. <https://doi.org/10.1051/epjap:2006145>.
- [37] Kymakis E, Amaratunga GAJ. Solar cells based on composites of donor conjugated polymers and carbon nanotubes. *Org. Photovoltaics Mech. Mater. Devices*, 2017. <https://doi.org/10.1201/9781420026351>.
- [38] Landi BJ, Raffaele RP, Castro SL, Bailey SG. Single-wall carbon nanotube-polymer solar cells. *Prog. Photovoltaics Res. Appl.*, 2005. <https://doi.org/10.1002/pip.604>.
- [39] Kymakis E, Klapsis G, Koudoumas E, Stratakis E, Kornilios N, Vidakis N, et al. THE EUROPEAN PHYSICAL JOURNAL Carbon nanotube/PEDOT:PSS electrodes for organic photovoltaics. *J Appl PhysNp Nanoparticles Polym* 2007. <https://doi.org/10.1051/epjap:2006148>.
- [40] Hu X, Hou P, Liu C, Cheng H. Carbon nanotube/silicon heterojunctions for photovoltaic applications. *Nano Mater Sci* 2019;1–17. <https://doi.org/10.1016/j.nanoms.2019.03.001>.
- [41] Street RA. Hydrogenated Amorphous Silicon. 1991. <https://doi.org/10.1017/cbo9780511525247>.
- [42] Luque A, Hegedus S. *Handbook of Photovoltaic Science and Engineering*. 2011. <https://doi.org/10.1002/9780470974704>.
- [43] DeWolf S, Descoeurdes A, Holman ZC, Ballif C. High-efficiency silicon heterojunction solar cells: A review. *Green* 2012. <https://doi.org/10.1515/green-2011-0018>.
- [44] Matsuda A. Thin-film silicon - Growth process and solar cell application. *Japanese J Appl Physics, Part 1 Regul Pap Short Notes Rev Pap* 2004. <https://doi.org/10.1143/JJAP.43.7909>.
- [45] Rockett A. *The materials science of semiconductors*. 2008.

- <https://doi.org/10.1007/978-0-387-68650-9>.
- [46] Staebler DL, Wronski CR. Reversible conductivity changes in discharge-produced amorphous Si. *Appl Phys Lett* 1977. <https://doi.org/10.1063/1.89674>.
- [47] Stutzmann M, Jackson WB, Tsai CC. Light-induced metastable defects in hydrogenated amorphous silicon: A systematic study. *Phys Rev B* 1985. <https://doi.org/10.1103/PhysRevB.32.23>.
- [48] Proctor JE, Armada DAM, Vijayaraghavan A. An introduction to graphene and carbon nanotubes. 2017. <https://doi.org/10.1201/9781315368191>.
- [49] Moisala A, Nasibulin AG, Brown DP, Jiang H, Khriachtchev L, Kauppinen EI. Single-walled carbon nanotube synthesis using ferrocene and iron pentacarbonyl in a laminar flow reactor. *Chem Eng Sci* 2006. <https://doi.org/10.1016/j.ces.2006.02.020>.
- [50] Liao Y, Hussain A, Laiho P, Zhang Q, Tian Y, Wei N, et al. Tuning Geometry of SWCNTs by CO₂ in Floating Catalyst CVD for High-Performance Transparent Conductive Films. *Adv Mater Interfaces* 2018. <https://doi.org/10.1002/admi.201801209>.
- [51] Anisimov AS, Nasibulin AG, Jiang H, Launois P, Cambedouzou J, Shandakov SD, et al. Mechanistic investigations of single-walled carbon nanotube synthesis by ferrocene vapor decomposition in carbon monoxide. *Carbon N Y* 2010. <https://doi.org/10.1016/j.carbon.2009.09.040>.
- [52] Nasibulin AG, Moisala A, Brown DP, Jiang H, Kauppinen EI. A novel aerosol method for single walled carbon nanotube synthesis. *Chem Phys Lett* 2005. <https://doi.org/10.1016/j.cplett.2004.12.040>.
- [53] Kaskela A, Nasibulin AG, Timmermans MY, Aitchison B, Papadimitratos A, Tian Y, et al. Aerosol-synthesized SWCNT networks with tunable conductivity and transparency by a dry transfer technique. *Nano Lett* 2010. <https://doi.org/10.1021/nl101680s>.
- [54] Tsapenko AP, Goldt AE, Shulga E, Popov ZI, Maslakov KI, Anisimov AS, et al. Highly conductive and transparent films of HAuCl₄-doped single-walled carbon nanotubes for flexible applications. *Carbon N Y* 2018. <https://doi.org/10.1016/j.carbon.2018.01.016>.
- [55] Tsapenko AP, Romanov SA, Satco DA, Krasnikov D V., Rajanna PM, Danilson M, et al. Aerosol-Assisted Fine-Tuning of Optoelectrical Properties of SWCNT Films. *J Phys Chem Lett* 2019. <https://doi.org/10.1021/acs.jpcclett.9b01498>.
- [56] Ki KK, Jung JB, Hyeon KP, Soo MK, Geng HZ, Kyung AP, et al. Fermi level engineering of single-walled carbon nanotubes by AuCl₃ doping. *J Am Chem Soc* 2008. <https://doi.org/10.1021/ja8038689>.
- [57] Kim KK, Yoon SM, Park HK, Shin HJ, Kim SM, Bae JJ, et al. Doping strategy of carbon nanotubes with redox chemistry. *New J Chem* 2010. <https://doi.org/10.1039/conj00138d>.
- [58] Elschner A, Kirchmeyer S, Lövenich W, Merker U, Reuter K. PEDOT: Principles and applications of an intrinsically conductive polyme. 2010.

- <https://doi.org/10.1201/b10318>.
- [59] Fan X, Nie W, Tsai H, Wang N, Huang H, Cheng Y, et al. PEDOT:PSS for Flexible and Stretchable Electronics: Modifications, Strategies, and Applications. *Adv Sci* 2019. <https://doi.org/10.1002/advs.201900813>.
- [60] Il Park S, Jae Baik S, Im JS, Fang L, Jeon JW, Su Lim K. Towards a high efficiency amorphous silicon solar cell using molybdenum oxide as a window layer instead of conventional p-type amorphous silicon carbide. *Appl Phys Lett* 2011. <https://doi.org/10.1063/1.3624591>.
- [61] Battaglia C, Yin X, Zheng M, Sharp ID, Chen T, McDonnell S, et al. Hole selective MoOxcontact for silicon solar cells. *Nano Lett* 2014. <https://doi.org/10.1021/nl404389u>.
- [62] Gerling LG, Mahato S, Morales-Vilches A, Masmitja G, Ortega P, Voz C, et al. Transition metal oxides as hole-selective contacts in silicon heterojunctions solar cells. *Sol Energy Mater Sol Cells* 2016. <https://doi.org/10.1016/j.solmat.2015.08.028>.
- [63] Guo Y, Robertson J. Origin of the high work function and high conductivity of MoO₃. *Appl Phys Lett* 2014. <https://doi.org/10.1063/1.4903538>.
- [64] Schulz P, Tiepelt JO, Christians JA, Levine I, Edri E, Sanehira EM, et al. High-work-function molybdenum oxide hole extraction contacts in hybrid organic-inorganic perovskite solar cells. *ACS Appl Mater Interfaces* 2016. <https://doi.org/10.1021/acsami.6b10898>.
- [65] Jiang Y, Li C, Liu H, Qin R, Ma H. Poly(3,4-ethylenedioxythiophene):poly(styrenesulfonate)(PEDOT:PSS)-molybdenum oxide composite films as hole conductors for efficient planar perovskite solar cells. *J Mater Chem A* 2016. <https://doi.org/10.1039/c6ta03658a>.
- [66] Li X, Jung Y, Huang JS, Goh T, Taylor AD. Device area scale-up and improvement of SWNT/Si solar cells using silver nanowires. *Adv Energy Mater* 2014. <https://doi.org/10.1002/aenm.201400186>.
- [67] Jeong S, Garnett EC, Wang S, Yu Z, Fan S, Brongersma ML, et al. Hybrid silicon nanocone-polymer solar cells. *Nano Lett* 2012. <https://doi.org/10.1021/nl300713x>.
- [68] Mikheev GM, Nasibulin AG, Zonov RG, Kaskela A, Kauppinen EI. Photon-Drag Effect in Single-Walled Carbon Nanotube Films. *Nano Lett* 2012;12:77–83. <https://doi.org/10.1021/nl203003p>.
- [69] Watts JF, Wolstenholme J. *An Introduction to Surface Analysis by XPS and AES*. 2019. <https://doi.org/10.1002/9781119417651>.
- [70] Sze SM, Ng KK. *Physics of Semiconductor Devices: Third Edition*. 2006. <https://doi.org/10.1002/9780470068328>.
- [71] Eaton P, West P. *Atomic Force Microscopy*. 2010. <https://doi.org/10.1093/acprof:oso/9780199570454.001.0001>.
- [72] Butt HJ, Cappella B, Kappl M. Force measurements with the atomic force microscope: Technique, interpretation and applications. *Surf Sci Rep*

- 2005;59:1–152. <https://doi.org/10.1016/j.surfrep.2005.08.003>.
- [73] Melitz W, Shen J, Kummel AC, Lee S. Kelvin probe force microscopy and its application. *Surf Sci Rep* 2011. <https://doi.org/10.1016/j.surfrep.2010.10.001>.
- [74] Wohlgemuth JH. Standards for pv modules and components – Recent developments and challenges. 27th Eur Photovolt Sol Energy Conf Exhib 2012.
- [75] IEC. IEC 60904-3 Edition 2.0 Part 3: Measurement principles for terrestrial photovoltaic (PV) solar devices with reference spectral irradiance data. 2008. <https://doi.org/10.3403/01776181>.
- [76] Abou-Ras D, Kirchartz T, Rau U. *Advanced Characterization Techniques for Thin Film Solar Cells: Second Edition*. 2016. <https://doi.org/10.1002/9783527699025>.
- [77] Nasibulin AG, Kaskela A, Mustonen K, Anisimov AS, Ruiz V, Kivistö S, et al. Multifunctional free-standing single-walled carbon nanotube films. *ACS Nano* 2011. <https://doi.org/10.1021/nn200338r>.
- [78] Moisala A, Nasibulin AG, Brown DP, Jiang H, Khriachtchev L, Kauppinen EI. Single-walled carbon nanotube synthesis using ferrocene and iron pentacarbonyl in a laminar flow reactor. *Chem Eng Sci* 2006. <https://doi.org/10.1016/j.ces.2006.02.020>.
- [79] Kaskela A, Nasibulin AG, Timmermans MY, Aitchison B, Papadimitratos A, Tian Y, et al. Aerosol-synthesized SWCNT networks with tunable conductivity and transparency by a dry transfer technique. *Nano Lett* 2010. <https://doi.org/10.1021/nl101680s>.
- [80] Cappella B, Baschieri P, Frediani C, Miccoli P, Ascoli C. Force-distance curves by AFM. *IEEE Eng Med Biol Mag* 1997;16:58–65. <https://doi.org/10.1109/51.582177>.
- [81] Meyer E, Gyalog T, Overney RM, Dransfeld K. Nanoscience: Friction and Rheology on the Nanometer Scale. 2012. <https://doi.org/10.1142/3026>.
- [82] Dremov V, Fedoseev V, Fedorov P, Grebenko A. Fast and reliable method of conductive carbon nanotube-probe fabrication for scanning probe microscopy. *Rev Sci Instrum* 2015. <https://doi.org/10.1063/1.4921323>.
- [83] Adam Moser, Kevin Range and DMY. Adhesion Force Measurements Using an Atomic Force Microscope Upgraded with a Linear Position Sensitive Detector. *Bone* 2008;23:1–7. <https://doi.org/10.1038/jid.2014.371>.
- [84] Shandakov SD, Lomakin M V., Nasibulin AG. The effect of the environment on the electronic properties of single-walled carbon nanotubes. *Tech Phys Lett* 2016. <https://doi.org/10.1134/S1063785016110080>.
- [85] Paaanen M, Katainen J, Pakarinen OH, Foster AS, Lahtinen J. Experimental humidity dependency of small particle adhesion on silica and titania. *J Colloid Interface Sci* 2006. <https://doi.org/10.1016/j.jcis.2006.09.017>.
- [86] Weeks BL, Vaughn MW, Deyoreo JJ. Direct imaging of meniscus formation in atomic force microscopy using environmental scanning electron microscopy. *Langmuir* 2005. <https://doi.org/10.1021/la0512087>.

- [87] Xiao X, Qian L. Investigation of humidity-dependent capillary force. *Langmuir* 2000. <https://doi.org/10.1021/la000770o>.
- [88] Sirghi L, Nakagiri N, Sugisaki K, Sugimura H, Takai O. Effect of sample topography on adhesive force in atomic force spectroscopy measurements in air. *Langmuir* 2000. <https://doi.org/10.1021/la000392n>.
- [89] Jones R, Pollock HM, Cleaver JAS, Hodges CS. Adhesion forces between glass and silicon surfaces in air studied by AFM: Effects of relative humidity, particle size, roughness, and surface treatment. *Langmuir* 2002. <https://doi.org/10.1021/la0259196>.
- [90] Fukunishi A, Mori Y. Adhesion force between particles and substrate in a humid atmosphere studied by atomic force microscopy. *Adv Powder Technol* 2006. <https://doi.org/10.1163/156855206778440552>.
- [91] Kyakuno H, Fukasawa M, Ichimura R, Matsuda K, Nakai Y, Miyata Y, et al. Diameter-dependent hydrophobicity in carbon nanotubes. *J Chem Phys* 2016. <https://doi.org/10.1063/1.4960609>.
- [92] McLachlan a. D. Retarded Dispersion Forces in Dielectrics at Finite Temperatures. *Proc R Soc A Math Phys Eng Sci* 1963. <https://doi.org/10.1098/rspa.1963.0115>.
- [93] Leite FL, Bueno CC, Da Róz AL, Ziemath EC, Oliveira ON. Theoretical models for surface forces and adhesion and their measurement using atomic force microscopy. *Int J Mol Sci* 2012. <https://doi.org/10.3390/ijms131012773>.
- [94] Tressaud A, Durand E, Labrugère C, Kharitonov AP, Kharitonova LN. Modification of surface properties of carbon-based and polymeric materials through fluorination routes: From fundamental research to industrial applications. *J Fluor Chem* 2007. <https://doi.org/10.1016/j.jfluchem.2006.12.015>.
- [95] Liang T, Neumann CN, Ritter T. Introduction of fluorine and fluorine-containing functional groups. *Angew Chemie - Int Ed* 2013. <https://doi.org/10.1002/anie.201206566>.
- [96] Tian Y, Timmermans MY, Kivistö S, Nasibulin AG, Zhu Z, Jiang H, et al. Tailoring the diameter of single-walled carbon nanotubes for optical applications. *Nano Res* 2011. <https://doi.org/10.1007/s12274-011-0137-6>.
- [97] Fan Q, Zhang Q, Zhou W, Xia X, Yang F, Zhang N, et al. Novel approach to enhance efficiency of hybrid silicon-based solar cells via synergistic effects of polymer and carbon nanotube composite film. *Nano Energy* 2017. <https://doi.org/10.1016/j.nanoen.2017.02.003>.
- [98] Neumüller A, Bereznev S, Ewert M, Volobujeva O, Sergeev O, Falta J, et al. Carrier collection losses in interface passivated amorphous silicon thin-film solar cells. *Appl Phys Lett* 2016. <https://doi.org/10.1063/1.4959995>.
- [99] Vitoratos E, Sakkopoulos S, Paliatsas N, Emmanouil K, Choulis SA. Conductivity Degradation Study of PEDOT: PSS Films under Heat Treatment in Helium and Atmospheric Air. *Open J Org Polym Mater* 2012.

- <https://doi.org/10.4236/ojopm.2012.21002>.
- [100] Dosenovicova D, Maricheva J, Neumüller A, Sergeev O, Volobujeva O, Nasibulin AG, et al. Selective photoelectrochemical deposition of polypyrrole onto hydrogenated a-Si for optoelectronic applications. *Mater Sci Semicond Process* 2017. <https://doi.org/10.1016/j.mssp.2017.05.028>.
- [101] Deslippe J, Spataru CD, Prendergast D, Louie SG. Bound excitons in metallic single-walled carbon nanotubes. *Nano Lett* 2007. <https://doi.org/10.1021/nl070577f>.
- [102] Schropp REI, Zeman M. Amorphous and Microcrystalline Silicon Solar Cells: Modeling, Materials and Device Technology. 1998. <https://doi.org/10.1007/978-1-4615-5631-2>.
- [103] Fuhrer MS, Kim BM, Dürkop T, Brintlinger T. High-Mobility Nanotube Transistor Memory. *Nano Lett* 2002. <https://doi.org/10.1021/nl025577o>.
- [104] Snow ES, Campbell PM, Ancona MG, Novak JP. High-mobility carbon-nanotube thin-film transistors on a polymeric substrate. *Appl Phys Lett* 2005. <https://doi.org/10.1063/1.1854721>.
- [105] Li R, Di J, Yong Z, Sun B, Li Q. Polymethylmethacrylate coating on aligned carbon nanotube-silicon solar cells for performance improvement. *J Mater Chem A* 2014. <https://doi.org/10.1039/c3ta14625a>.
- [106] Li X, Yu X, Han Y. Polymer thin films for antireflection coatings. *J Mater Chem C* 2013. <https://doi.org/10.1039/c2tc00529h>.
- [107] Yu LP, Tune DD, Shearer CJ, Shapter JG. Implementation of antireflection layers for improved efficiency of carbon nanotube-silicon heterojunction solar cells. *Sol Energy* 2015. <https://doi.org/10.1016/j.solener.2015.06.014>.
- [108] Neumüller A, Sergeev O, Heise SJ, Bereznev S, Volobujeva O, Salas JFL, et al. Improved amorphous silicon passivation layer for heterojunction solar cells with post-deposition plasma treatment. *Nano Energy* 2018. <https://doi.org/10.1016/j.nanoen.2017.11.053>.
- [109] Anoshkin I V., Nasibulin AG, Tian Y, Liu B, Jiang H, Kauppinen EI. Hybrid carbon source for single-walled carbon nanotube synthesis by aerosol CVD method. *Carbon N Y* 2014. <https://doi.org/10.1016/j.carbon.2014.06.057>.
- [110] Jeon I, Cui K, Chiba T, Anisimov A, Nasibulin AG, Kauppinen EI, et al. Direct and Dry Deposited Single-Walled Carbon Nanotube Films Doped with MoO_x as Electron-Blocking Transparent Electrodes for Flexible Organic Solar Cells. *J Am Chem Soc* 2015. <https://doi.org/10.1021/jacs.5b03739>.
- [111] Esconjauregui S, D'Arسيé L, Guo Y, Yang J, Sugime H, Caneva S, et al. Efficient Transfer Doping of Carbon Nanotube Forests by MoO₃. *ACS Nano* 2015. <https://doi.org/10.1021/acsnano.5b04644>.
- [112] Çolak F, Dalkiliç Z, Tabatabaei A, Atlibatur R, Çolak, Arici E, et al. MoO_x doped single-walled carbon nanotube films as hole transport layer for organic solar cells. *Acta Phys. Pol. A*, 2017. <https://doi.org/10.12693/APhysPolA.131.474>.
- [113] Zhang KHL, Xi K, Blamire MG, Egdell RG. *P*-type transparent conducting

References

- oxides. *J Phys Condens Matter* 2016. <https://doi.org/10.1088/0953-8984/28/38/383002>.
- [114] Hellstrom SL, Vosgueritchian M, Stoltenberg RM, Irfan I, Hammock M, Wang YB, et al. Strong and stable doping of carbon nanotubes and graphene by MoO_x for transparent electrodes. *Nano Lett* 2012. <https://doi.org/10.1021/nl301207e>.

Publication 1

Pramod M. Rajanna*, Sergey Luchkin, Konstantin V. Larionov, Artem Grebenko, Zakhar I. Popov, Pavel B. Sorokin, Mati Danilson, Sergei Bereznev, Peter D. Lund, and Albert G. Nasibulin*. Adhesion of Single-Walled Carbon Nanotube Thin Films with Different Materials. *J. Phys. Chem. Lett.* 2020, 11, 504–509. DOI: 10.1021/acs.jpcclett.9b03552

© 2020 American Chemical Society.
Reprinted with permission

Adhesion of Single-Walled Carbon Nanotube Thin Films with Different Materials

Pramod M. Rajanna,* Sergey Luchkin, Konstantin V. Larionov, Artem Grebenko, Zakhar I. Popov, Pavel B. Sorokin, Mati Danilson, Sergei Bereznev, Peter D. Lund, and Albert G. Nasibulin*

Cite This: *J. Phys. Chem. Lett.* 2020, 11, 504–509

Read Online

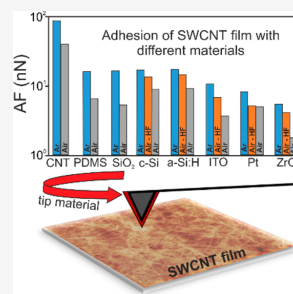
ACCESS |

Metrics & More

Article Recommendations

Supporting Information

ABSTRACT: Single-walled carbon nanotubes (SWCNTs) possess extraordinary physical and chemical properties. Thin films of randomly oriented SWCNTs have great potential in many opto-electro-mechanical applications. However, good adhesion of SWCNT films with a substrate material is pivotal for their practical use. Here, for the first time, we systematically investigate the adhesion properties of SWCNT thin films with commonly used substrates such as glass (SiO₂), indium tin oxide (ITO), crystalline silicon (C–Si), amorphous silicon (a-Si:H), zirconium oxide (ZrO₂), platinum (Pt), polydimethylsiloxane (PDMS), and SWCNTs for self-adhesion using atomic force microscopy. By comparing the results obtained in air and inert Ar atmospheres, we observed that the surface state of the materials greatly contributes to their adhesion properties. We found that the SWCNT thin films have stronger adhesion in an inert atmosphere. The adhesion in the air can be greatly improved by a fluorination process. Experimental and theoretical analyses suggest that adhesion depends on the atmospheric conditions and surface functionalization.



The unique properties of single-walled carbon nanotubes (SWCNTs) are attracting extensive interest from the scientific community for different applications.^{1–7} The usage of SWCNT networks as efficient transparent conductors is a particular challenge in terms of obtaining conformal films with smooth surfaces as well as creating a firm contact between the film and other materials.⁸ The substrate material considerably influences the adhesion of the SWCNT films. The performance of many SWCNT applications is governed by van der Waals (VdW) interactions with the substrate,^{9–11} in particular when nanotubes are used as transparent electrodes in optoelectronic devices.⁸ The contact between the nanotube film and substrate material impacts the interface properties that affect the device efficiency.^{12,13} In a SWCNT network, many nanotubes overlap and are suspended over each other without making contact with the substrate material, for example, in SWCNT/Si solar cell devices, lowering their performance.^{14,15} To overcome this, novel approaches have been proposed such as densification of SWCNTs,^{15–17} acid doping,^{16–18} and impregnating SWCNTs with conductive polymers.^{19,20} Thus, a better understanding of the adhesion of nanotube films and the associated mechanisms is important for the long-term reliability of devices employing the SWCNT films.^{21,22}

The significance of SWCNT adhesion has been discussed^{10,23–25} through lateral atomic force microscopy (AFM),^{9,22,23,26,27} tapping mode AFM,²⁴ dynamic force AFM,²⁵ and theoretical works using continuum analysis and atomistic simulations^{11,28,29} probing the adhesive properties of SWCNTs with other materials and between nanotubes themselves.^{11,21,22,26,27,29–31} Reported methods have been

deduced using either a hypothesis for the interaction of SWCNTs with its environment^{11,29} or experimental quantification of multiwalled carbon nanotubes or individual nanotube loop adhesion energy.^{22,26,27} However, the evidence from SWCNT thin film applications clearly indicates that the interaction of SWCNT films with the substrate is still an open question.

Here, we quantitatively evaluate the interaction of SWCNT thin films with various commonly used substrate materials (henceforth called materials) using AFM in air and inert Ar atmospheres. The materials chosen include glass (SiO₂), indium tin oxide (ITO), crystalline silicon (C–Si), amorphous silicon (a-Si:H), zirconium oxide (ZrO₂), platinum (Pt), polydimethylsiloxane (PDMS), and SWCNTs for self-adhesion measurements. We show that the adhesion of randomly oriented SWCNT thin films is strongly influenced by the atmospheric conditions and surface functionalization of the material. The measurements demonstrate stronger adhesion in an inert atmosphere, but adhesion in air can be greatly improved by a simple fluorination process.

We utilized aerosol-synthesized SWCNTs,^{32,33} which are dry-transferred from a nitrocellulose filter³⁴ to a desired substrate, which is a Si wafer in this case. Figure S1a shows the

Received: December 2, 2019

Accepted: January 1, 2020

Published: January 1, 2020

cross-sectional scanning electron microscopy (SEM) image of the SWCNT thin film on the Si wafer and the surface of randomly oriented closely connected individual and bundled nanotubes. The thickness of the film was ~ 44 nm as determined by SEM as shown in Figure S1a and verified from the absorbance spectrum (Figure S1b) as described by Mikheev et al.³⁵ This film was investigated in an atomic force microscope by collecting force–distance (F – D) curves between the SWCNT thin film sample and cantilevers coated by a given material as shown in Figure 1.

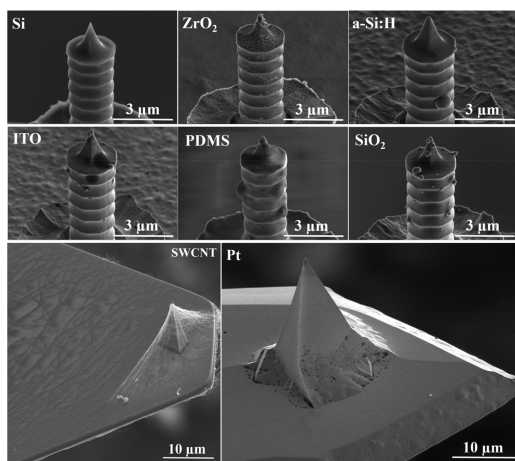


Figure 1. Cantilever tips covered with different materials: Si, ZrO₂, a-Si:H, ITO, PDMS, SiO₂, SWCNT, and Pt.

A flexible lever of the atomic force microscope cantilever is clamped from one side on a Si chip installed in a cantilever holder. The other free-standing side with a sharp tip is placed several tens of nanometers above the sample surface. Upon the approach, the distance between the tip and the sample is reduced, and the tip touches the sample and sets a compressive force on it, the value of which is determined from the lever upward bending using Hooke's law, $F = k\Delta d$, where k is the cantilever spring constant and Δd is the distance from the

onset of the compressive force to the set point. After reaching a predefined set point force, the tip is retracted from the sample and detached from it at an attractive force (downward lever bending), which is a measure of the adhesion force.^{36–38} This force depends on the experimental conditions such as the maximum force load and the cantilever tip radius. Collected maps of F – D curves (averaged over 65536 measurements in air and 1024 measurements in an inert Ar atmosphere, as detailed in section S1) were analyzed by the microscope software. The sample deformation, adhesion force, and peak force values are extracted from F – D curves³⁸ as shown in Figure S2. The peak force, or maximum force load, is a predefined set point parameter that is controlled by a microscope feedback loop system.

To determine and compare intrinsic adhesion parameters between SWCNTs and a given material, the measured adhesion force must be normalized by the tip–CNT contact area, which is governed by the aforementioned force load and tip radius. We used the Hertz model³⁹ to estimate the tip–surface contact area at the extremum applied force as $S = \pi R_{\text{tip}} h$, where R_{tip} is the tip apex radius and h is the deformation. Within this model, we assumed that the tip apex is a rigid sphere of a certain radius R_{tip} , which was measured on the dimpled aluminum substrate⁴⁰ (Table S1), the CNT surface is elastic half-space, and the strain is in the elastic limit. We also neglected surface roughness. Despite the fact that in the Hertz model the contact is nonadhesive, it can be accurately applied to adhesive contacts when the adhesive force is small compared to the applied force. The maximum applied force is limited due to the fact that the probe is likely to drop through a meshy SWCNT surface upon high force loading. As a result, the tip–sample contact area sharply increased due to side contacts of the tip with surrounding CNTs, leading to the increase in the adhesion force (e.g., panels a and b of Figure 2 show the change in the slope of adhesion force with deformation for ZrO₂ at a peak force of 50 nN as in the inset). With this assumption, we attribute the moment of the tip drop with the slope break in the plots shown in panels a and b of Figure 2, respectively. With an increasing applied force, the adhesion force demonstrates a gradual linear growth. Applying a force of 50 nN resulted in a large increase in the adhesion force and in some cases a decrease in the deformation as shown in Figure 2b and the

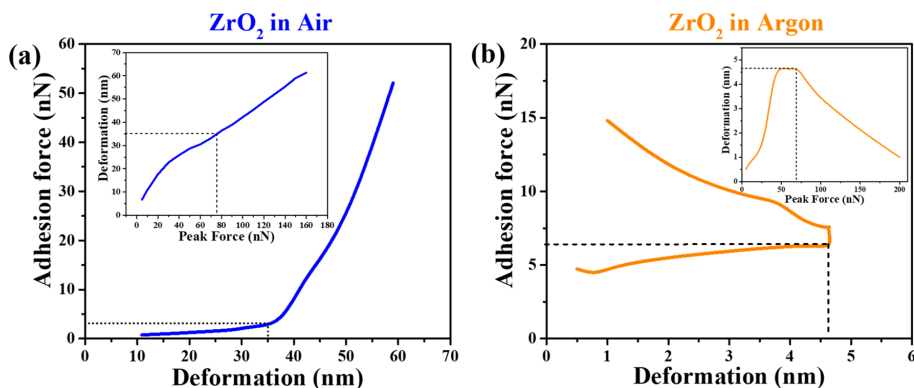


Figure 2. Adhesion force vs deformation measured in (a) air and (b) inert Ar atmospheres between the SWCNT film and ZrO₂.

corresponding F – D curves in Figure S2. The plots for other materials are available in Figure S3. For all of the materials, the slope break happened after the application of 50 nN of force, so we used this value for the Hertz model. The measured adhesion force (AF) as described above^{36–38} and the calculated surface adhesion force density (SAFD), which is the adhesion force normalized to the contact area, are represented in Figure 3 and Figure S4.

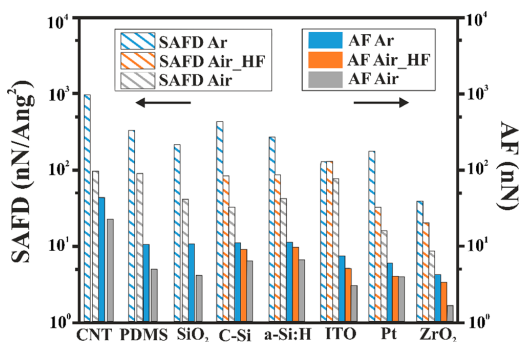


Figure 3. Adhesion force (AF) (right axis, solid bars) and surface adhesion force density (SAFD) (left axis, dashed bars) of SWCNT thin films with various materials.

For all studied materials, the normalized adhesion force (adhesion force density) in the inert Ar atmosphere is higher than in ambient air, which can be explained by the difference in the ambient humidity and its influence on the SWCNTs as shown by Shandakov et al.⁴¹ The relative humidity (RH) can affect adhesive properties, especially in nanoscale, due to formation of a capillary bridge when RH exceeds roughly a threshold value of 25%.^{42–44} The capillary force strongly depends on the sample local curvature, which affects the capillary bridge geometry, resulting in a higher adhesion force for the concave surface and a smaller adhesion force for the convex surface.^{42,45} On hydrophilic surfaces, increasing humidity increases the pull-off force, whereas on hydrophobic surfaces, humidity has a negligible effect.^{46,47} Because SWCNTs are hydrophobic⁴⁸ and possess a convex surface geometry, the capillary bridge effect is likely to be negligible. Instead, the smaller adhesion force in air is better explained by the reduction of the VdW forces in a polar water medium between the tip and the SWCNT thin film^{28,49} (section S3.1).

The experimentally measured adhesion force shown in Figure 3 can explain the following observations. SWCNT thin films are easily dry-transferred onto a-Si:H, Si, SiO₂, and PDMS in air, while under the same conditions, the transfer onto ITO and Pt is complicated and completely failed on ZrO₂. However, the same SWCNT thin films are easily dry-transferred on all of the materials in an inert atmosphere.

To verify that the adhesion force is strongly dependent on the humidity, we fluorinated the a-Si:H-, C-Si-, ZrO₂-, ITO-, and Pt-coated tips. The process of fluorination is well-known to alter the surface properties of materials without changing the bulk characteristics of the pristine material.^{50,51} The altered properties may concern wettability, adhesion, chemical stability, permeation, electrical conductivity, biocompatibility, grafting, mechanical behavior, and several others.⁵⁰ We used the dry process fluorination, which proceeds spontaneously at

room temperature via exposure of the samples to hydrofluoric (HF) vapor for 60 s. Each tip was calibrated once again immediately after the HF treatment, and the adhesion force measurements were conducted on the same SWCNT thin film in air at a peak force of 50 nN. The measured adhesion forces were recorded for the HF-treated tips and are shown in Figure 3, revealing that the adhesion force increased for all HF-treated tips. This trend is similar to the adhesion force measurements conducted in the inert atmosphere. Moreover, after the fluorination process, SWCNT films can be easily dry-transferred even on problematic materials, such as ITO, Pt, and ZrO₂.

To understand the role of fluorination in improving the adhesion of SWCNT thin films and their chemical composition, X-ray photoelectron spectroscopy (XPS) was carried out on ZrO₂ and a-Si:H tips (section S4). XPS infers that fluorinating the surface of the material in air modifies the chemical composition by partially eliminating the presence of humidity and creating fluorine-terminated Zr and C bonds (Figure S5d–h), which aids in improving adhesion and explains the easy dry-transfer of SWCNTs on ZrO₂ after HF treatment under ambient conditions.

The experimental measurements were realized under three different conditions using AFM: ambient air, HF treatment in air, and inert Ar atmosphere. Ambient air leads to material surface contamination, and the use of HF treatment in air helps to partially clean it by elimination of the native oxides and water vapor, which has been demonstrated in a number of experimental and theoretical works.^{52–54}

To explain the dependence of SWCNT thin film adhesion on the different materials and environmental conditions, we carried out density functional theory (DFT) (described in section S5). In compliance with our experimental conditions, three different cases with Si, Pt, ITO, and SiO₂ materials were studied, however replacing SWCNTs with a graphene monolayer. Inert atmosphere conditions were realized as the graphene monolayer on the clean material surface, and HF treatment in air was simulated as the graphene monolayer on the hydrogenated material surface. In the calculations, HF treatment in air was considered as hydrogenated surfaces and not specifically with fluorine atoms as the intention was to analyze the effects of different environmental conditions only. Also, data on fluorinated bonds were too limited for detailed DFT analysis in our case. Finally, ambient air conditions are represented as the graphene monolayer on the material surface passivated by OH or CO groups.^{52,55,56}

Calculation of the adhesion energy attributed to the VdW interaction was made directly by the following equation:

$$E_{\text{adh}} \left(\frac{\text{eV}}{\text{\AA}^2} \right) = \frac{1}{A} [E_{\text{total}} - (E_{\text{C}} + E_{\text{sub}})] \quad (1)$$

where A is the contact area between the graphene and the substrate in the unit cell, E_{total} is the total energy of the graphene/substrate system, and E_{C} and E_{sub} are the energies of the separate graphene and substrate, respectively.

A comparison of the calculated adhesion energy (E_{adh}) and experimental adhesion force density (SAFD) for Si, Pt, ITO, and SiO₂ under different conditions is shown in Figure 4. Here, theoretical and experimental values are shown by solid bars (left axis) and dashed bars (right axis, logarithmic scale), respectively. With blue (Ar), orange (HF), and gray (Air) colors, we depict the inert atmosphere, HF treatment in air, and ambient air conditions, respectively. Atomic models of

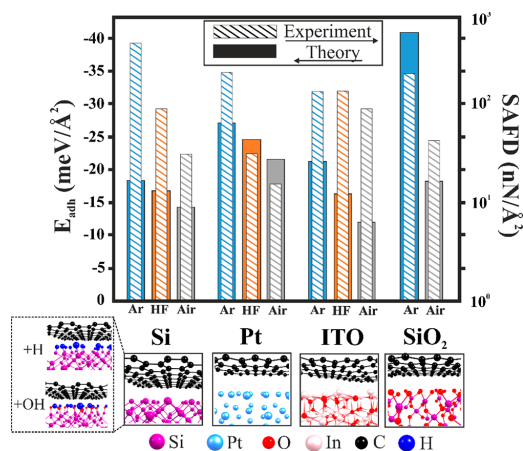


Figure 4. Comparison of the calculated adhesion energy (left axis, solid bars) and experimental adhesion force density (right axis, dashed bars) for Si, Pt, ITO, and SiO₂ under different environmental conditions, where Ar corresponds to the inert atmosphere, HF stands for HF treatment in air, and Air is the air condition. Atomic models of pristine interfaces (as in the inert atmosphere) and Si surface functionalized by H or OH groups are shown as examples below the corresponding graphs. The other atomic models are shown in Figure S6.

pristine interfaces (as in the inert atmosphere) after DFT optimization are shown below the corresponding material names in Figure 4. For the Si case, optimized atomic models of the interface passivated by H (HF treatment in air) and OH (ambient air) are shown in the dashed box (bottom left). The other atomic models are represented in Figure S6.

From Figure 4, we see a good correspondence between the experimental measurements and DFT simulations yielding the main effect of adhesion change under different conditions. Indeed, for every case of the graphene/material model, the pristine surface (blue solid bars) has adhesion energies higher than those of the hydrogenated surfaces (orange solid bars). Also, the hydrogenated surfaces have stronger interaction with graphene than in the case of their passivation by OH or CO groups (gray solid bars). The same monotonous trends are observed for the experimentally measured SAFD values shown in the logarithmic scale for a better representation (dashed bars).

From the DFT simulations, we can conclude that the contaminated material surface in ambient air worsens the adhesion with graphene (carbon nanotubes). However, through preliminary HF treatment of the material surface, native oxides and water vapors are possibly partially eliminated, which results in improved adhesion for graphene (carbon nanotubes). At the same time, the inert atmosphere conditions additionally allow the elimination of any intermediate functional groups on the surface of the material and approach to almost direct interaction of the partially clean SWCNT and AFM tip as demonstrated in the real experiment.

In summary, for the first time, we carried out adhesion force measurements of randomly oriented SWCNT thin films in air and inert atmospheres with various materials deposited directly on the AFM tips. Quantitative values were derived for the adhesion force from the force–distance curves by estimating

the tip–surface contact area according to the Hertz model. Through experimental observations and theoretical simulations, we conclude that the adhesion is greatly influenced by the environmental conditions and surface functionalization. We observe that the SWCNT thin films have better adhesion in an inert atmosphere. The adhesion affected by storing the samples under ambient air conditions can be greatly improved by a simple fluorination process. This work provides new insight into the physical mechanisms of SWCNT thin film adhesion that will succeed in its efficient usage with its exceptional properties for future roll-to-roll applications.

■ ASSOCIATED CONTENT

Supporting Information

The Supporting Information is available free of charge at <https://pubs.acs.org/doi/10.1021/acs.jpcllett.9b03552>.

Methods (section S1), SWCNT film characterization (section S2), AFM measurements (section S3), discussion (section S3.1), XPS of ZrO₂ and a-Si:H cantilever tips (section S4), and theoretical simulation of adhesion energy (section S5) (PDF)

■ AUTHOR INFORMATION

Corresponding Authors

Pramod M. Rajanna – Skolkovo Institute of Science and Technology, Moscow, Russia, and Aalto University, Espoo, Finland; orcid.org/0000-0002-6175-4442; Email: pramod.rajanna@skolkovotech.ru

Albert G. Nasibulin – Skolkovo Institute of Science and Technology, Moscow, Russia, and Aalto University, Espoo, Finland; orcid.org/0000-0002-1684-3948; Email: a.nasibulin@skoltech.ru

Other Authors

Sergey Luchkin – Skolkovo Institute of Science and Technology, Moscow, Russia

Konstantin V. Larionov – National University of Science and Technology MISIS, Moscow, Russia, Technological Institute for Superhard and Novel Carbon Materials, Moscow, Russia, and Moscow Institute of Physics and Technology, Dolgoprudny, Russia; orcid.org/0000-0003-4771-7220

Artem Grebenko – Skolkovo Institute of Science and Technology, Moscow, Russia, and Moscow Institute of Physics and Technology, Dolgoprudny, Russia

Zakhar I. Popov – National University of Science and Technology MISIS, Moscow, Russia, and Emanuel Institute of Biochemical Physics, Russian Academy of Sciences, Moscow, Russia

Pavel B. Sorokin – National University of Science and Technology MISIS, Moscow, Russia, Technological Institute for Superhard and Novel Carbon Materials, Moscow, Russia, and Moscow Institute of Physics and Technology, Dolgoprudny, Russia; orcid.org/0000-0001-5248-1799

Mati Danilson – Tallinn University of Technology, Tallinn, Estonia

Sergei Bereznev – Tallinn University of Technology, Tallinn, Estonia

Peter D. Lund – Aalto University, Espoo, Finland;

orcid.org/0000-0002-4819-3847

Complete contact information is available at:

<https://pubs.acs.org/10.1021/acs.jpclett.9b03552>

Notes

The authors declare no competing financial interest.

ACKNOWLEDGMENTS

The authors thank Ivan S. Mukhin of Saint Petersburg Academic University and ITMO University for a-Si:H and ITO depositions. The authors thank Aapo Poskela (Aalto University) for ZrO₂ deposition and Dr. Lide Yao (Aalto University) for SEM measurements of the SWCNT thin film cross section and morphology. P.M.R. and A.G.N. acknowledge the Russian Science Foundation for support (synthesis of SWCNTs) via Project 17-19-01787. K.V.L., Z.I.P., and P.B.S. gratefully acknowledge the financial support of the Ministry of Education and Science of the Russian Federation in the framework of Increase Competitiveness Program of NUST "MISIS" (K2-2019-016). K.V.L. and P.B.S. gratefully acknowledge a Grant of President of Russian Federation for government support of young DSc. (MD-1046.2019.2). The authors are grateful to supercomputer cluster NUST "MISIS" provided by the Materials Modeling and Development Laboratory (supported via Ministry of Education and Science of the Russian Federation Grant 14.Y26.31.0005) and to the Joint Supercomputer Center of the Russian Academy of Sciences. M.D. and S.B. acknowledge the support by institutional research funding IUT19-28 of the Estonian Ministry of Education and the European Union through the European Regional Development Fund (Project TK141). P.M.R. is thankful for the partial financial support from an EDUFI Fellowship (TM-19-11028) from the Finnish National Agency for Education.

REFERENCES

- Jariwala, D.; Sangwan, V. K.; Lauhon, L. J.; Marks, T. J.; Hersam, M. C. Carbon Nanomaterials for Electronics, Optoelectronics, Photovoltaics, and Sensing. *Chem. Soc. Rev.* **2013**, *42*, 2824.
- Tian, Y.; Timmermans, M. Y.; Kivistö, S.; Nasibulin, A. G.; Zhu, Z.; Jiang, H.; Okhotnikov, O. G.; Kauppinen, E. I. Tailoring the Diameter of Single-Walled Carbon Nanotubes for Optical Applications. *Nano Res.* **2011**, *4*, 807.
- Baughman, R. H.; Zakhidov, A. A.; De Heer, W. A. Carbon Nanotubes - The Route toward Applications. *Science* **2002**, *297*, 787.
- Jeon, I.; Matsuo, Y.; Maruyama, S. Single-Walled Carbon Nanotubes in Solar Cells. *Topics in Current Chemistry* **2018**, *4* DOI: 10.1007/s41061-017-0181-0.
- Avouris, P.; Chen, Z.; Perebeinos, V. Carbon-Based Electronics. *Nat. Nanotechnol.* **2007**, *2*, 605.
- Liu, Y.; Wang, F.; Wang, X.; Wang, X.; Flahaut, E.; Liu, X.; Li, Y.; Wang, X.; Xu, Y.; Shi, Y.; et al. Planar Carbon Nanotube-Graphene Hybrid Films for High-Performance Broadband Photodetectors. *Nat. Commun.* **2015**, *6*, 1–7.
- Sun, D. M.; Timmermans, M. Y.; Tian, Y.; Nasibulin, A. G.; Kauppinen, E. I.; Kishimoto, S.; Mizutani, T.; Ohno, Y. Flexible High-Performance Carbon Nanotube Integrated Circuits. *Nat. Nanotechnol.* **2011**, *6*, 156.
- Ellmer, K. Past Achievements and Future Challenges in the Development of Optically Transparent Electrodes. *Nat. Photonics* **2012**, *6*, 809.
- Hertel, T.; Walkup, R. E.; Avouris, P. Deformation of Carbon Nanotubes by Surface van Der Waals Forces. *Phys. Rev. B: Condens. Matter Mater. Phys.* **1998**, *58*, 13870.
- Hertel, T.; Martel, R.; Avouris, P. Manipulation of Individual Carbon Nanotubes and Their Interaction with Surfaces. *J. Phys. Chem. B* **1998**, *102*, 910.
- Tang, T.; Jagota, A.; Hui, C. Y. Adhesion between Single-Walled Carbon Nanotubes. *J. Appl. Phys.* **2005**, *97* (7), 074304.
- Li, X.; Jung, Y.; Sakimoto, K.; Goh, T. H.; Reed, M. A.; Taylor, A. D. Improved Efficiency of Smooth and Aligned Single Walled Carbon Nanotube/Silicon Hybrid Solar Cells. *Energy Environ. Sci.* **2013**, *6*, 879.
- Rajanna, P. M.; Meddeb, H.; Sergeev, O.; Tsapenko, A. P.; Bereznev, S.; Vehse, M.; Volobujeva, O.; Danilson, M.; Lund, P. D.; Nasibulin, A. G. Rational Design of Highly Efficient Flexible and Transparent P-Type Composite Electrode Based on Single-Walled Carbon Nanotubes. *Nano Energy* **2020**, *67*, 104183.
- Jia, Y.; Wei, J.; Wang, K.; Cao, A.; Shu, Q.; Gui, X.; Zhu, Y.; Zhuang, D.; Zhang, G.; Ma, B.; et al. Nanotube-Silicon Heterojunction Solar Cells. *Adv. Mater.* **2008**, *20* (23), 4594–4598.
- Hu, X.; Hou, P.; Liu, C.; Cheng, H. Carbon Nanotube/Silicon Heterojunctions for Photovoltaic Applications. *Nano Mater. Sci.* **2019**, *1*, 156–172.
- Azoubel, S.; Magdassi, S. Controlling Adhesion Properties of SWCNT-PET Films Prepared by Wet Deposition. *ACS Appl. Mater. Interfaces* **2014**, *6*, 9265.
- Santidrián, A.; Sanahuja, O.; Villacampa, B.; Diez, J. L.; Benito, A. M.; Maser, W. K.; Muñoz, E.; Anson-Casas, A. Chemical Postdeposition Treatments to Improve the Adhesion of Carbon Nanotube Films on Plastic Substrates. *ACS Omega* **2019**, *4*, 2804.
- Jia, Y.; Cao, A.; Bai, X.; Li, Z.; Zhang, L.; Guo, N.; Wei, J.; Wang, K.; Zhu, H.; Wu, D. Achieving High Efficiency Silicon-Carbon Nanotube Heterojunction Solar Cells by Acid Doping. *Nano Lett.* **2011**, *11*, 1901.
- Rajanna, P. M.; Gilshteyn, E. P.; Yagafarov, T.; Alekseeva, A. K.; Anisimov, A. S.; Neumüller, A.; Sergeev, O.; Bereznev, S.; Maricheva, J.; Nasibulin, A. G. Enhanced Efficiency of Hybrid Amorphous Silicon Solar Cells Based on Single-Walled Carbon Nanotubes and Polymer Composite Thin Film. *Nanotechnology* **2018**, *29* (10), 105404.
- Fan, Q.; Zhang, Q.; Zhou, W.; Xia, X.; Yang, F.; Zhang, N.; Xiao, S.; Li, K.; Gu, X.; Xiao, Z. Novel Approach to Enhance Efficiency of Hybrid Silicon-Based Solar Cells via Synergistic Effects of Polymer and Carbon Nanotube Composite Film. *Nano Energy* **2017**, *33*, 436.
- Li, W.; Li, Y.; Sheng, M.; Cui, S.; Wang, Z.; Zhang, X.; Yang, C.; Yu, Z.; Zhang, Y.; Tian, S. Enhanced Adhesion of Carbon Nanotubes by Dopamine Modification. *Langmuir* **2019**, *35*, 4527.
- Buchoux, J.; Bellon, L.; Marsaudon, S.; Aimé, J. P. Carbon Nanotubes Adhesion and Nanomechanical Behavior from Peeling Force Spectroscopy. *Eur. Phys. J. B* **2011**, *84*, 69.
- Falvo, M. R.; Taylor, R. M.; Helser, A.; Chi, V.; Brooks, F. P.; Washburn, S.; Superfine, R. Nanometre-Scale Rolling and Sliding of Carbon Nanotubes. *Nature* **1999**, *397*, 236.
- Akita, S.; Nishijima, H.; Nakayama, Y. Influence of Stiffness of Carbon-Nanotube Probes in Atomic Force Microscopy. *J. Phys. D: Appl. Phys.* **2000**, *33*, 2673.
- Lee, S. W.; Kim, K. K.; Cui, Y.; Lim, S. C.; Cho, Y. W.; Kim, S. M.; Lee, Y. H. Adhesion Test of Carbon Nanotube Film Coated onto Transparent Conducting Substrates. *Nano* **2010**, *5* (3), 133–138.
- Li, T.; Ayari, A.; Bellon, L. Adhesion Energy of Single Wall Carbon Nanotube Loops on Various Substrates. *J. Appl. Phys.* **2015**, *117*, 164309.
- Whittaker, J. D.; Minot, E. D.; Tanenbaum, D. M.; McEuen, P. L.; Davis, R. C. Measurement of the Adhesion Force between Carbon Nanotubes and a Silicon Dioxide Substrate. *Nano Lett.* **2006**, *6*, 953.
- Leite, F. L.; Bueno, C. C.; Da Róz, A. L.; Ziemath, E. C.; Oliveira, O. N. Theoretical Models for Surface Forces and Adhesion and Their Measurement Using Atomic Force Microscopy. *Int. J. Mol. Sci.* **2012**, *13*, 12773.

- (29) Yuan, X.; Wang, Y. Adhesion of Single- and Multi-Walled Carbon Nanotubes to Silicon Substrate: Atomistic Simulations and Continuum Analysis. *J. Phys. D: Appl. Phys.* **2017**, *50* (39), 395303.
- (30) Hashimoto, A.; Takei, Y.; Iwase, E.; Matsumoto, K.; Shimoyama, I. Adhesion Force Measurement between Silicon and Carbon Nanotubes Synthesized by Chemical Vapor Deposition. In *TRANSDUCERS 2009 - 15th International Conference on Solid-State Sensors, Actuators and Microsystems*; IEEE, 2009; p 2066.
- (31) Zhao, B.; Qi, H.; Liu, X.; Xu, D. Measurement of Adhesive Force between Single-Walled Carbon Nanotube and Ti. *Fullerenes, Nanotubes, Carbon Nanostruct.* **2012**, *20*, 750.
- (32) Nasibulin, A. G.; Kaskela, A.; Mustonen, K.; Anisimov, A. S.; Ruiz, V.; Kivistö, S.; Rackauskas, S.; Timmermans, M. Y.; Pudas, M.; Aitchison, B. Multifunctional Free-Standing Single-Walled Carbon Nanotube Films. *ACS Nano* **2011**, *5*, 3214.
- (33) Moaisal, A.; Nasibulin, A. G.; Brown, D. P.; Jiang, H.; Khriachtchev, L.; Kauppinen, E. I. Single-Walled Carbon Nanotube Synthesis Using Ferrocene and Iron Pentacarbonyl in a Laminar Flow Reactor. *Chem. Eng. Sci.* **2006**, *61*, 4393.
- (34) Kaskela, A.; Nasibulin, A. G.; Timmermans, M. Y.; Aitchison, B.; Papadimitratos, A.; Tian, Y.; Zhu, Z.; Jiang, H.; Brown, D. P.; Zakhidov, A. Aerosol-Synthesized SWCNT Networks with Tunable Conductivity and Transparency by a Dry Transfer Technique. *Nano Lett.* **2010**, *10*, 4349.
- (35) Mikheev, G. M.; Nasibulin, A. G.; Zonov, R. G.; Kaskela, A.; Kauppinen, E. I. Photon-Drag Effect in Single-Walled Carbon Nanotube Films. *Nano Lett.* **2012**, *12* (1), 77–83.
- (36) Pierce, M.; Stuart, J.; Pungor, A.; Dryden, P.; Hlady, V. Adhesion Force Measurements Using an Atomic Force Microscope Upgraded with a Linear Position Sensitive Detector. *Langmuir* **1994**, *10*, 3217.
- (37) Butt, H. J.; Cappella, B.; Kappl, M. Force Measurements with the Atomic Force Microscope: Technique, Interpretation and Applications. *Surf. Sci. Rep.* **2005**, *59* (1–6), 1–152.
- (38) Cappella, B.; Baschieri, P.; Frediani, C.; Miccoli, P.; Ascoli, C. Force-Distance Curves by AFM. *IEEE Eng. Med. Biol. Mag.* **1997**, *16* (2), 58–65.
- (39) Meyer, E.; Gyalog, T.; Overney, R. M.; Dransfeld, K., Eds. *Nanoscience: Friction and Rheology on the Nanometer Scale*; World Scientific: Singapore, 1998.
- (40) Dremov, V.; Fedoseev, V.; Fedorov, P.; Grebenko, A. Fast and Reliable Method of Conductive Carbon Nanotube-Probe Fabrication for Scanning Probe Microscopy. *Rev. Sci. Instrum.* **2015**, *86*, 053703.
- (41) Shandakov, S. D.; Lomakin, M. V.; Nasibulin, A. G. The Effect of the Environment on the Electronic Properties of Single-Walled Carbon Nanotubes. *Tech. Phys. Lett.* **2016**, *42*, 1071.
- (42) Paajanen, M.; Katainen, J.; Pakarinen, O. H.; Foster, A. S.; Lahtinen, J. Experimental Humidity Dependency of Small Particle Adhesion on Silica and Titania. *J. Colloid Interface Sci.* **2006**, *304*, 518.
- (43) Weeks, B. L.; Vaughn, M. W.; Deyoreo, J. J. Direct Imaging of Meniscus Formation in Atomic Force Microscopy Using Environmental Scanning Electron Microscopy. *Langmuir* **2005**, *21*, 8096.
- (44) Xiao, X.; Qian, L. Investigation of Humidity-Dependent Capillary Force. *Langmuir* **2000**, *16*, 8153.
- (45) Sirghi, L.; Nakagiri, N.; Sugisaki, K.; Sugimura, H.; Takai, O. Effect of Sample Topography on Adhesive Force in Atomic Force Spectroscopy Measurements in Air. *Langmuir* **2000**, *16*, 7796.
- (46) Jones, R.; Pollock, H. M.; Cleaver, J. A. S.; Hodges, C. S. Adhesion Forces between Glass and Silicon Surfaces in Air Studied by AFM: Effects of Relative Humidity, Particle Size, Roughness, and Surface Treatment. *Langmuir* **2002**, *18*, 8045.
- (47) Fukunishi, A.; Mori, Y. Adhesion Force between Particles and Substrate in a Humid Atmosphere Studied by Atomic Force Microscopy. *Adv. Powder Technol.* **2006**, *17*, 567.
- (48) Kyakuno, H.; Fukasawa, M.; Ichimura, R.; Matsuda, K.; Nakai, Y.; Miyata, Y.; Saito, T.; Maniwa, Y. Diameter-Dependent Hydrophobicity in Carbon Nanotubes. *J. Chem. Phys.* **2016**, *145*, 064514.
- (49) McLachlan, A. D. Retarded Dispersion Forces in Dielectrics at Finite Temperatures. *Proc. R. Soc. A Math. Phys. Eng. Sci.* **1963**, *274*, 80.
- (50) Tressaud, A.; Durand, E.; Labrugère, C.; Kharitonov, A. P.; Kharitonova, L. N. Modification of Surface Properties of Carbon-Based and Polymeric Materials through Fluorination Routes: From Fundamental Research to Industrial Applications. *J. Fluorine Chem.* **2007**, *128*, 378.
- (51) Liang, T.; Neumann, C. N.; Ritter, T. Introduction of Fluorine and Fluorine-Containing Functional Groups. *Angew. Chem., Int. Ed.* **2013**, *52*, 8214.
- (52) Wu, C. J.; Carter, E. A. Mechanistic Predictions for Fluorine Etching of Si(100). *J. Am. Chem. Soc.* **1991**, *113*, 9061.
- (53) Kang, J. K.; Musgrave, C. B. The Mechanism of HF/H₂O Chemical Etching of SiO₂. *J. Chem. Phys.* **2002**, *116* (1), 275–280.
- (54) Dhar, S.; Seitz, O.; Halls, M. D.; Choi, S.; Chabal, Y. J.; Feldman, L. C. Chemical Properties of Oxidized Silicon Carbide Surfaces upon Etching in Hydrofluoric Acid. *J. Am. Chem. Soc.* **2009**, *131*, 16808.
- (55) Donley, C.; Dunphy, D.; Paine, D.; Carter, C.; Nebesny, K.; Lee, P.; Alloway, D.; Armstrong, N. R. Characterization of Indium-Tin Oxide Interfaces Using X-Ray Photoelectron Spectroscopy and Redox Processes of a Chemisorbed Probe Molecule: Effect of Surface Pretreatment Conditions. *Langmuir* **2002**, *18*, 450.
- (56) Ertl, G.; Neumann, M.; Streit, K. M. Chemisorption of CO on the Pt(111) Surface. *Surf. Sci.* **1977**, *64*, 393.

Publication 2

Pramod M Rajanna*, Evgenia P Gilshteyn, Timur Yagafarov, Alena K Aleekseeva, Anton S Anisimov, Alex Neumüller, Oleg Sergeev, Sergei Berez-nev, Jelena Maricheva, and Albert G Nasibulin*. Enhanced efficiency of hybrid amorphous silicon solar cells based on single-walled carbon nanotubes and polymer composite thin film. *Nanotechnology* 29 (2018) 105404 (10pp). DOI: 10.1088/1361-6528/aaa647.

© 2018 IOP Publishers.
Reprinted with permission

PAPER

Enhanced efficiency of hybrid amorphous silicon solar cells based on single-walled carbon nanotubes and polymer composite thin film

To cite this article: Pramod M Rajanna *et al* 2018 *Nanotechnology* **29** 105404

View the [article online](#) for updates and enhancements.

Enhanced efficiency of hybrid amorphous silicon solar cells based on single-walled carbon nanotubes and polymer composite thin film

Pramod M Rajanna^{1,6}, Evgenia P Gilshteyn¹, Timur Yagafarov¹, Alena K Aleekseeva¹, Anton S Anisimov², Alex Neumüller³, Oleg Sergeev³, Sergei Bereznev⁴, Jelena Maricheva⁴ and Albert G Nasibulin^{1,5,6}

¹ Skolkovo Institute of Science and Technology, Skolkovo Innovation Center, Building 3, Moscow 143026, Russia

² Canatu Oy, Konalankuja 5, FI-00390 Helsinki, Finland

³ DLR Institute of Networked Energy Systems, German Aerospace Center (DLR), Carl-von-Ossietzky-Straße 15, D-26129 Oldenburg, Germany

⁴ Tallinn University of Technology, Department of Materials and Environmental Technology, Ehitajate tee 5, 19086 Tallinn, Estonia

⁵ Department of Applied Physics, Aalto University, School of Science, PO Box 15100, FI-00076 Espoo, Finland

E-mail: pramod.rajanna@skolkovotech.ru, pramod8503@gmail.com and a.nasibulin@skoltech.ru

Received 25 October 2017, revised 23 December 2017

Accepted for publication 9 January 2018

Published 31 January 2018



CrossMark

Abstract

We report a simple approach to fabricate hybrid solar cells (HSCs) based on a single-walled carbon nanotube (SWCNT) film and thin film hydrogenated amorphous silicon (a-Si:H). Randomly oriented high-quality SWCNTs with conductivity enhanced by means of poly(3,4-ethylenedioxythiophene) polystyrene sulfonate are used as a window layer and a front electrode. A series of HSCs are fabricated in ambient conditions with varying SWCNT film thicknesses. The polymethylmethacrylate layer drop-casted on fabricated HSCs reduces the reflection fourfold and enhances the short-circuit J_{sc} , open-circuit V_{oc} , and efficiency by nearly 10%. A state-of-the-art $J-V$ performance is shown for SWCNT/a-Si HSC with an open-circuit voltage of 900 mV and an efficiency of 3.4% under simulated one-sun AM 1.5 G direct illumination.

Keywords: carbon nanotube, amorphous silicon, PEDOT, PSS, solar cells, heterojunction

(Some figures may appear in colour only in the online journal)

1. Introduction

The use of non-crystalline and heterogeneous materials for solar cells has grown significantly over the past three decades and is currently one of the most active areas in photovoltaics (PVs) research. The studies in this field have three main objectives: (1) to improve the power conversion efficiency of devices; (2) to reduce production costs, and (3) to ensure that

module performance is maintained for several decades in outdoor conditions, thereby providing more energy than is used in production [1].

In recent years, hybrid solar cells (HSCs) with thin film amorphous silicon (a-Si:H) absorbers and spin-casted organic conductive polymer layers have attracted considerable interest due to the comparatively low cost of manufacturing large-area and mechanically flexible PV devices at a low processing temperature. Several studies have reported on a-Si:H and other organic conductive polymers such as PEDOT:PSS, P3HT,

⁶ Authors to whom any correspondence should be addressed.

PCBM, MEH-PPV, PCPDTBT HSCs, and more recently, polypyrrole/a-Si HSC [2–8] with photo-conversion efficiencies not exceeding 3%. On the other hand, carbon-based nanomaterials, for example, carbon nanotubes (CNTs), have made a valuable contribution to recent advances in the field of solar cell development in C-Si [9–11], CNT-polymer [12], and more recently in perovskite-based [13] solar cells. Furthermore, there are several reports showing improvements in HSC efficiency by the use of CNTs and conductive polymers such as PEDOT:PSS [14, 15]. The family of carbon nanomaterials, and especially single-walled CNTs (SWCNTs), has advantages in terms of higher flexibility, surface area, carrier mobility, chemical stability, and optoelectronic properties. A thin SWCNT film can be used not only as a perfect window layer in solar cells, but also as a transparent conductive electrode due to its direct sub-band gaps, tunable photoabsorption from the near infrared (NIR) range to the ultraviolet (UV) range, and high conductivity [13, 16–19]. However, to date not much research effort has been made into studying thin film HSCs based on SWCNTs and a-Si:H. Several studies investigated the PV behavior for HSCs based on carbon nanostructures and a-Si:H; however, the devices were reported to exhibit very poor power conversion efficiencies (PCE) of 0.02% [20], 0.08% [21], 0.5%, and 1.5% [22, 23], which is far from acceptable for real PV applications. We believe the main reasons for such low PCEs were low-quality pristine CNTs as well as a poor contact between a-Si:H and CNTs.

Here, we have developed solar cells that are based on the intrinsic a-Si:H thin film layer as the primary light absorber and optimized pristine SWCNT thickness with an enhanced conductivity by PEDOT:PSS as a window layer (instead of a p-doped a-Si:H layer) and conducting front contact. They are used as an alternative to transparent conductive oxides, usually indium tin oxide or aluminum-doped zinc oxide (AZO). These prototype cells also partially exclude the expensive vacuum technique in producing the window layer and the front contact by means of a dry transfer technique [24]. This reduces the exposure to toxic gases such as silane (SiH_4) and diborane (B_2H_6), as well as further high-energy, time-consuming and expensive vacuum sputtering processes. We fabricated state-of-the-art hybrid (a-Si:H) solar cells based on SWCNTs and a polymer composite thin film.

2. Experimental

2.1. Material synthesis and characterization

We used SWCNTs synthesized by the aerosol CVD technique described in detail elsewhere [24, 25]. These SWCNTs with an average diameter of 2.1 nm [26] are a randomly oriented network consisting of a mixture of metallic and semi-conducting tubes with p-type conductivity under ambient conditions [27]. Their thickness can easily be controlled by the collection time on a nitrocellulose membrane filter at the outlet of the reactor [25].

An electrically conductive PEDOT:PSS polymer layer was drop-casted from the pre-mix of commercially available 5 ml

PEDOT:PSS (1.3 wt.%; Sigma-Aldrich) aqueous suspension with 120 μl of glycerin, 250 μl of N-methylpyrrolidone, and 6.25 ml of isopropyl alcohol (IPA).

Polymethylmethacrylate (PMMA) was deposited from the solution by drop-casting. The solution was prepared by dissolving solid PMMA (molecular weight of 950 000; Sigma-Aldrich) in anisole (99.7%; Sigma-Aldrich) at a concentration of 4 wt.%.

X-ray photoelectron spectroscopy (XPS) was carried out to study the chemical composition of the SWCNT films using a Kratos Axis Ultra DLD. The transmission energy was 160 (survey) and 40 eV (high resolution spectra) with the AIKA source without a neutralizer.

Kelvin probe force microscopy (KPFM) from Asylum Research—Cypher ES tested the work function of the samples. We used BudgetSensors ElectriMulti75-G tips with a spring constant of 1.43 N m^{-1} and the first resonance frequency of 62.081 kHz. The measurements were conducted in an argon atmosphere glovebox in two pass amplitude modulated-KPFM with the second pass lift height of 35 nm. Highly oriented pyrolytic graphite ZYA was used for calibration prior to the actual measurements.

We used sheet resistance (R_s) and optical transmittance (T) for optoelectrical characterization of pristine SWCNT films. The sheet resistance was measured using a Jandel RM3000 four-probe unit. The optical transmittance was measured using a Perkin Elmer Lambda 1050 UV–vis–NIR spectrophotometer in a wide range from 150 to 3200 nm and hereafter usually referred to as 550 nm. The substrate contribution was subtracted as a background. Since absorbance (A) is a linear function of the SWCNT film thickness, the latter can be calculated using T_h (nm) = $417 \times A_{550}$ [28]. The thickness (T_h) and root mean square (RMS) roughness were confirmed using atomic force microscopy (AFM) (Cypher ES—Asylum Research).

The performance of the HSCs was measured under AM 1.5 G illumination with an intensity of 100 mW cm^{-2} at 25°C using a solar simulator (Newport Corporation, Oriel Sol3A Class AAA). The current density–voltage (J – V) characteristics were obtained with a source-measure unit (Keithley 2400). The external quantum efficiency (EQE) characteristics of the HSCs were measured using a spectral response measurement system (Bentham PVE300). This system used two sources of 75 W xenon (300–700 nm) and 100 W quartz halogen (700–1800 nm) coupled with a monochromator with a $1.85 \times 1.85 \text{ mm}^2$ slit at the output, which provides approximately a $2 \times 2 \text{ mm}^2$ monochromatic probe beam on the working plane of a calibrated solar cell. To correct the signal from the lamp spectrum, calibration was performed on a monocrystalline-Si sample. The stability of the HSCs was recorded, keeping it under the direct sun illumination for 1000 h.

Scanning electron microscopy (SEM) with a FEI Helios Nanolab 660 was used with a maximum accelerating voltage of 30 kV to investigate the morphology of SWCNTs and SWCNT/a-Si HSC cross-section. Transmission electron microscopy (TEM) with a FEI Tecnai G2 F20 was used with

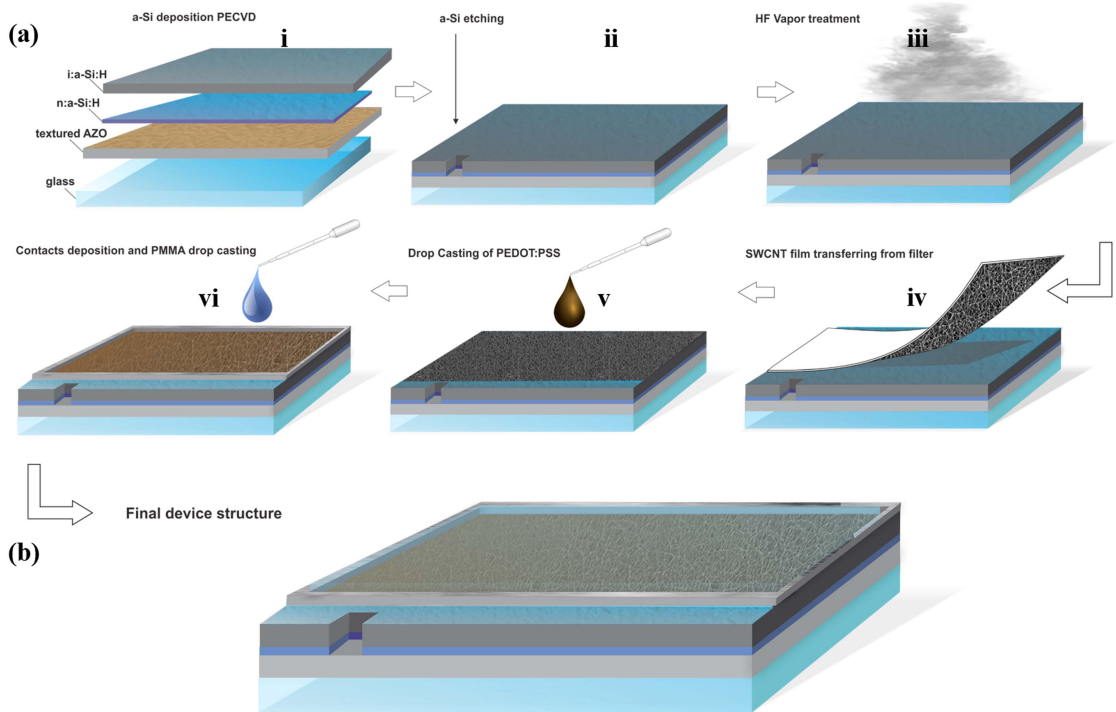


Figure 1. (a) Fabrication steps of a hybrid solar cell (HSC) process flow: (i) obtained structure with a-Si:H absorber; (ii) chemical local etching of a-Si:H to reach aluminum-doped zinc oxide back contact with KOH; (iii) hydrofluoric acid (HF) vapor treatment of a-Si:H surface for 140 s to etch the native oxide; (iv) dry transfer technique of single-walled carbon nanotubes (SWCNTs) on HF-treated a-Si:H surface at ambient conditions; (v) drop-casting of PEDOT:PSS at ambient conditions; (vi) bordering active area of the HSC with silver (silver paste) and final device structure of the HSC. (b) Fabricated SWCNT/a-Si:H HSC device.

an acceleration voltage of 80 kV and minimum possible illumination time for structural investigation of the SWCNTs.

The diffuse reflectance measurements were carried out on a Bentham PVE300 in the visible range from 300–900 nm.

2.2. Device fabrication

Figure 1(a) schematically shows the fabrication procedure of the HSCs. The initial layers were fabricated on Corning Eagle XG glass. First, AZO layers were deposited by DC-sputtering as a transparent back contact for bifacial solar cells. Then, n-doped (30 nm) and intrinsic (i) a-Si:H (300 nm) layers were grown using a plasma-enhanced chemical vapor deposition method described elsewhere [29]. The i:a-Si:H surface was treated with hydrofluoric acid (HF) vapor for 140 s to remove the native oxide from the surface. A series of pristine SWCNTs with varying thicknesses was dry-transferred onto this HF-treated i:a-Si:H surface under ambient conditions [24]. The transferred SWCNT film was densified by IPA drop-casting to ensure better contact and adhesion with the i:a-Si:H surface. The samples were further heated to 75 °C in air for 5 min to remove the residual solvent. A thin PEDOT:PSS layer with a thickness of 50 ± 5 nm was deposited by a simple drop-casting technique onto the SWCNT/a-Si:H. It was heated on a hot plate in air at 160 °C for 10 min. A thin

strip of silver paste was marked at the edges on four sides, forming an active HSC area of 0.3 cm².

The back contact AZO was reached locally by wet chemical etching of both silicon layers (330 nm), using a 6 M KOH solution. Prior to the etching, the samples were heated to 160 °C in air on a hot plate for 20 min. A small volume of 1 μ l KOH solution was drop-casted at the edge of the heated samples of the a-Si:H structure. The chemical reaction occurred immediately and the samples were removed from the hot plate after 5 s and then rinsed with deionized water. The samples were flushed with nitrogen gas and then heated to 70 °C in air for 5 min to ensure water evaporation. AZO resistivity was measured to be 16 Ω cm. The completed architecture of the SWCNT/a-Si:H solar cell device is shown in figure 1(b).

3. Results and discussion

3.1. Structural and chemical composition of SWCNT films

The pristine SWCNTs were dry-transferred from the nitrocellulose filter on a carbon-coated copper TEM grid and a crystalline silicon wafer for structural characterization and chemical composition analysis of the SWCNT films. The morphology and crystallinity of the tubes can be clearly seen

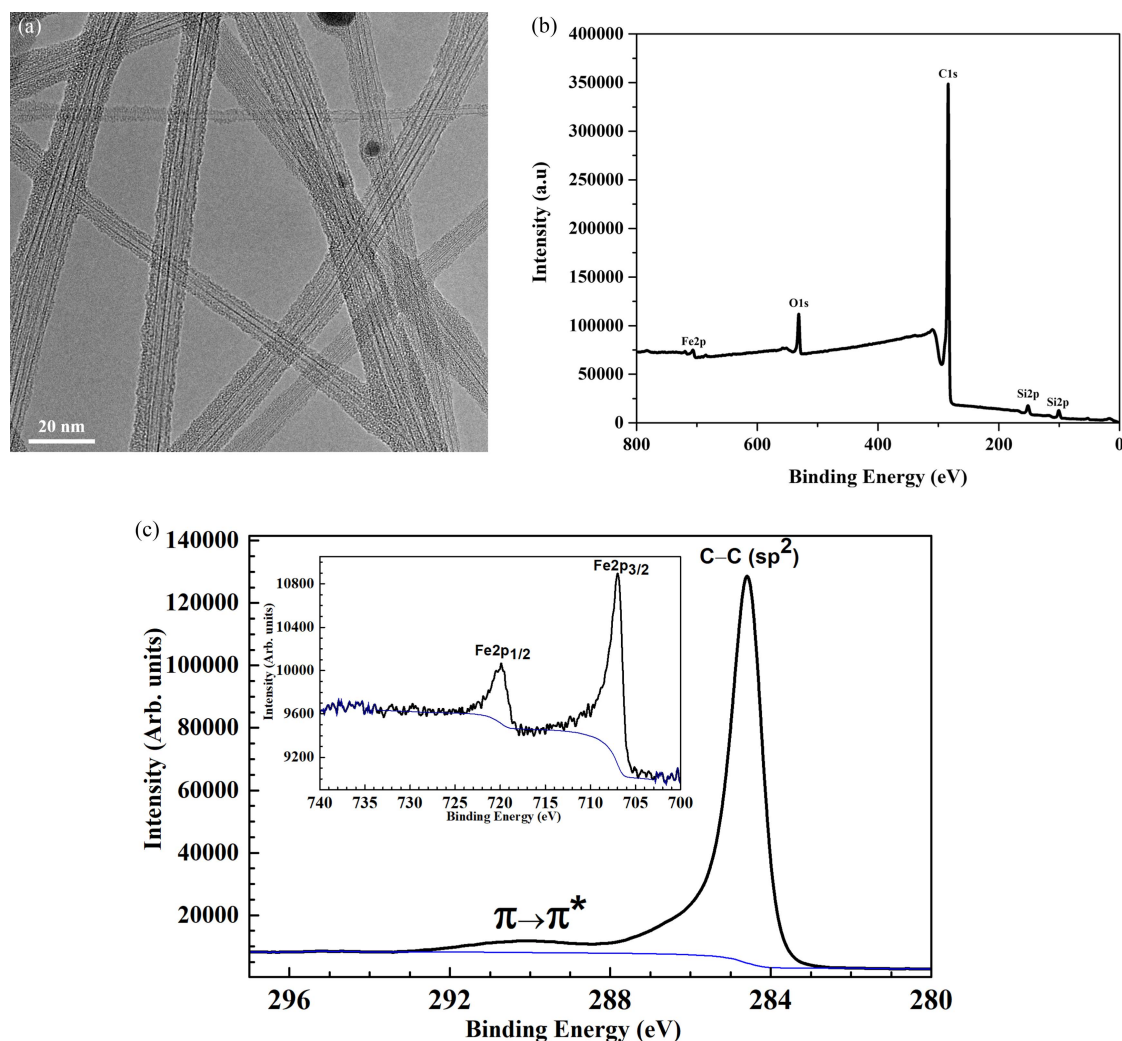


Figure 2. (a) TEM image of the SWCNT film; (b) XPS spectrum of the SWCNT film on a crystalline silicon wafer; (c) deconvoluted C1s XPS spectrum of the SWCNTs.

in a TEM image (figure 2(a)). Figure 2(b) shows the XPS spectrum of the investigated SWCNT film deposited on the silicon wafer. The spectrum mainly contains silicon, carbon, oxygen and iron lines. The observed carbon spectrum (figure 2(c)) is typical for sp^2 -carbon, as indicated by the asymmetry of the main peak and the presence of the $\pi \rightarrow \pi^*$ satellite in the binding energy region of about 290.5 eV. The shape and position of the Fe2p XPS spectrum (figure 2(c)) are typical for metallic iron.

The XPS spectra of the high resolution of the investigated sample (figure 2(b)) were decomposed into components. The concentration of the elements on the surface of the sample and the corresponding types of coupling are given in table 1.

Table 1. Elemental composition of the SWCNTs on a crystalline silicon wafer.

Element	Element content (at%)	Chemical bond
O	3.9	C-C (sp^3), C-CF, C-O, O=C-O, C=O, C-C (sp^2)
C	93.7	
Si	2.1	Si-Si, SiO ₂
Fe	0.3	Fe ⁰

3.2. Optoelectrical properties of SWCNT films

The pristine SWCNTs appear as a homogenous porous random network of bundles interconnected with each other, as

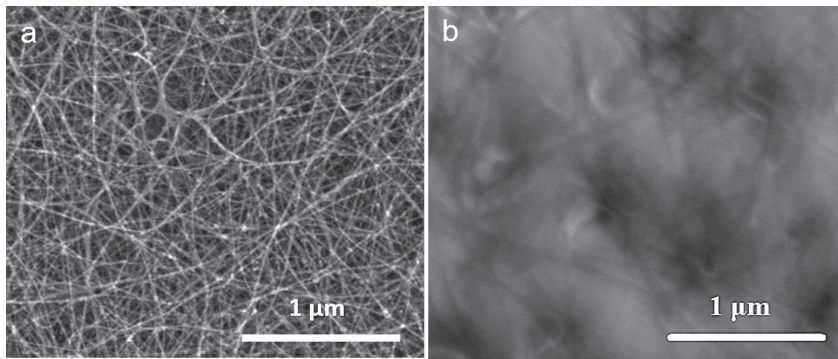


Figure 3. Morphological SEM image of: (a) the randomly oriented pristine SWCNT films; (b) uniformly-coated composite film (PEDOT:PSS—SWCNT film).

shown in figure 3(a). The SEM morphological image of PEDOT:PSS-SWCNT (composite film) in figure 3(b) enables the SWCNT network to retain its unique electrical and mechanical properties. Pristine SWCNTs of various transmittance values were characterized for thickness and sheet resistance. Therefore, the calculated thickness for a film with a transmittance of $T = 90\%$ was about 18 nm and the measured thickness from AFM was about 19 ± 1 nm. They were dry-transferred [24] on a cleaned micro glass slide ($1 \times 1 \text{ cm}^2$) to measure the sheet resistance and thickness. Figure 4 shows the dependence of the thickness and sheet resistance on the transmittance at 550 nm. Since the transmittance increased from 44.4% to 93.5%, the sheet resistance increased from 45 ± 2 to $360 \pm 2 \text{ } \Omega/\square$ respectively. In addition, a simple drop-cast of PEDOT:PSS ($2 \mu\text{l}$) on the SWCNT film led to a decrease in the sheet resistance of nearly one-half, to 23.4 ± 3.0 and $187.2 \pm 4.0 \text{ } \Omega/\square$ for the SWCNT films, with transmittances of $T = 44.4\%$ and $T = 93.5\%$, respectively. The values of the thickness, sheet resistance, and transmittance for SWCNT films without and with PEDOT:PSS are shown in table 2.

We used KPFM to better understand the decrease in the sheet resistance of SWCNTs with PEDOT:PSS. Three samples of SWCNT films with different thicknesses (CNT10, CNT20, and CNT100) were measured with and without PEDOT:PSS. We also measured a single PEDOT:PSS film in a separate measurement. The values of the work function were calculated from KPFM surface potential measurements for the pristine SWCNTs ($4.50 \pm 0.05 \text{ eV}$), composite film ($4.95 \pm 0.05 \text{ eV}$), and PEDOT:PSS ($5.30 \pm 0.05 \text{ eV}$).

The decrease in the sheet resistance of the composite film and the increase in its work function compared to the pristine SWCNT film can account for the fact that the PEDOT:PSS filled micropores in the film and, consequently, doped the SWCNTs. As can be seen from figure 3(b), the surface of the composite film is flat and the SWCNT bundled network cannot be observed clearly from the top of the composite film. This is confirmed by the AFM surface roughness measurements, wherein the pristine SWCNT films showed an RMS roughness of 20 nm, while the composite film RMS roughness was 7 nm. The effect of SWCNT doping can be clearly

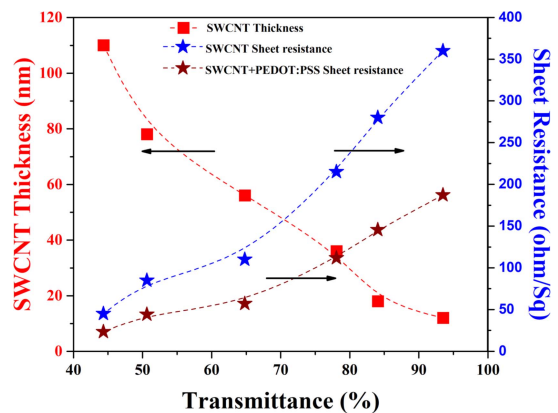


Figure 4. Dependence of SWCNT film thickness and sheet resistance on transmittance at 550 nm.

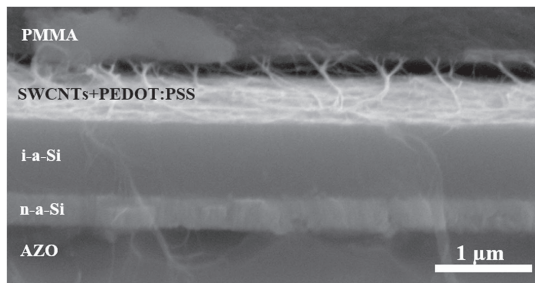
seen, as the work function of the composite film is higher than that of the pristine SWCNTs. Although PEDOT:PSS is less conductive and has a low carrier mobility, the continuous SWCNT network serves as a carrier transport bridge due to its high carrier mobility. Moreover, the net effect of conductivity enhancement is observed to be more pronounced for thinner SWCNT films with PEDOT:PSS, probably due to better distribution of the conducting polymer in the network of SWCNT bundles. This results in a homogeneous coating along the thickness of thinner SWCNT films. This can be observed from table 2, where CNT10 and CNT20 have thicknesses similar to that of PEDOT:PSS, indicating penetration of polymer through the SWCNTs, while CNT40, CNT60, CNT80 and CNT100 have nearly the combined thickness of the polymer and the SWCNTs.

3.3. SWCNT/a-Si:H HSC—as prepared devices

The sketch of the fabricated SWCNT/a-Si:HSC device architecture is shown in figure 1(b). The cross-section SEM image of the HSC (figure 5) clearly shows the individual layers of back contact (AZO), n:a-Si:H (n-type), i:a-Si:H

Table 2. Optoelectrical properties of SWCNT film and SWCNT film + PEDOT:PSS as a function of thickness (nm), transmittance (%), and sheet resistance (Ω/\square).

Sample name	SWCNT film thickness, Th (nm)	SWCNT film transmittance, T (%)	SWCNT film sheet resistance, R_s (Ω/\square)	SWCNT film + PEDOT:PSS thickness, Th (nm)	SWCNT film + PEDOT:PSS transmittance, T (%)	SWCNT film + PEDOT:PSS sheet resistance, R_s (Ω/\square)
CNT10	12	93.5	360	52	91.2	187.2
CNT20	19	84.1	280	61	82.3	145.6
CNT40	38	78.1	215	85	75.8	111.8
CNT60	57	64.8	110	104	62.4	57.2
CNT80	76	50.7	85	124	48.1	44.2
CNT100	95	44.4	45	143	41.6	23.4

**Figure 5.** A cross-section SEM image of a SWCNT/a-Si HSC.

(intrinsic absorber layer), and SWCNT film with PEDOT:PSS (p-type) stacked one above the other, forming a substrate configuration *nip* structure. Neither the standard transparent conducting layer nor the contact grid were fabricated on the front side of HSCs.

The J - V characteristics of HSCs fabricated with pristine SWCNTs of varying thicknesses (samples are named as CNT10, CNT20, CNT40, CNT60, CNT80, and CNT100) are shown in figure 6(a) and tabulated in table 3. We achieved a PCE of $\eta = 2.7 \pm 0.3\%$ with a fill factor (FF) of $41.5 \pm 3\%$ for CNT20. As shown in figure 5(a), a pristine SWCNT thickness of 19 ± 1 nm was found to be the best in combination with PEDOT:PSS (50 ± 5 nm). We measured the short-circuit current density (J_{sc}) of 7.9 ± 0.1 mA cm $^{-2}$ and the open-circuit voltage (V_{oc}) of 0.82 ± 0.04 V. While analyzing the dark state curve shown in figure 6(a), we obtained the reverse saturation current density of $J_0 = 6.05 \pm 0.01 \times 10^{-4}$ mA cm $^{-2}$, the shunt resistance of $R_p = 106.0 \pm 0.5$ M Ω /cm 2 , the series resistance of $R_s = 30 \pm 2$ k Ω /cm 2 , and the diode ideality factor of $n = 1.10 \pm 0.05$. The high shunt resistance value together with a very low value of reverse saturation current density and series resistance led to a high PCE of the SWCNT/a-Si:H HSCs. For these measurements, the light was from the SWCNT side. Moreover, during the analysis of the J - V parameters in table 3, we found that the current density increased from 3.90 ± 0.02 mA cm $^{-2}$ for CNT10 to 7.9 ± 0.1 mA cm $^{-2}$ for CNT20; it then decreased for all the subsequent HSC devices with thicker SWCNT films beyond 19 nm. The low current

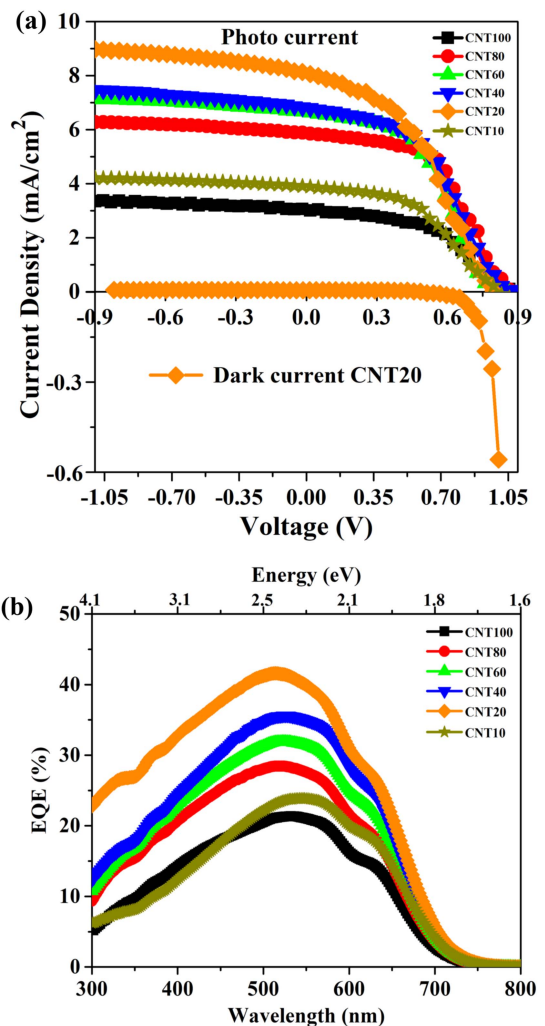
**Figure 6.** Characteristics of HSCs fabricated with SWCNT films of different thicknesses: (a) J - V curves of photo and dark current response for CNT20; (b) external quantum efficiency (EQE) spectra.

Table 3. Comparison of J - V parameters: open-circuit voltage (V_{oc}), short-circuit current density (J_{sc}), fill factor (FF), and power conversion efficiency (η) of HSCs fabricated with SWCNT films of different thicknesses.

Sample Name	V_{oc} (V)	J_{sc} (mA cm ⁻²)	FF (%)	η (%)
CNT10	0.828	3.90	46.9	1.5
CNT20	0.820	7.90	41.5	2.7
CNT40	0.904	6.80	44.1	2.7
CNT60	0.896	5.90	52.3	2.8
CNT80	0.860	5.70	45.4	2.6
CNT100	0.872	3.04	48.0	1.3

density for CNT10 can be explained by the high resistance of the SWCNTs and PEDOT:PSS. A further increase in the thickness of the SWCNT film beyond 19 nm with PEDOT:PSS yielded a lower current density, induced by the decrease in transmittance of SWCNT films. It must be taken into account that the back reflection and the carrier collection on the back side were provided with only an AZO layer and not with a back metal contact. This significantly reduced the cell efficiency. In addition, figure 6(b) shows the experimental EQE spectra corresponding to various SWCNT thicknesses in HSCs. It can be observed that the EQE value decreased with an increase in the thickness of SWCNT films, with a maximum EQE value of 42% at 514 nm obtained for CNT20, exhibiting a strong blue response. This might have been induced by lower absorption in the composite film (p-layer) and reduced recombination at the a-Si:H/SWCNT interface in comparison with any other SWCNT film thickness. The current density is calculated from the EQE for the CNT20 film from the following equation [30]:

$$J_{sc}^{EQE} = -q \int_{\lambda_1}^{\lambda_2} EQE(\lambda) \Phi_{ph,\lambda}^{AM1.5} d\lambda,$$

where the spectral photon flux with a range from 300 to 800 nm is 7.1 ± 0.1 mA cm⁻². The current density values from the J - V curve and EQE closely match. Furthermore, it is interesting to note that the line shape of the EQE curve does not change, irrespective of the SWCNT film thickness. For CNT10, CNT40, CNT60, and CNT80 the EQE dramatically decreases for wavelengths shorter than 350 nm, indicating a strong surface recombination at the i:a-Si:H/SWCNT interface. A sharp fall in the EQE for all SWCNT film thicknesses beyond 700 nm can be attributed to the a-Si:H energy gap (1.7 eV). The spectral behavior resembles the a-Si:H *nip* solar cells, indicating that the photo generation process goes on mainly within the i:a-Si:H.

The high current density of CNT20 can also account for the inherent Schottky behavior of SWCNTs due to metallic and semiconducting tubes within its network. Semiconducting SWCNTs have a work function of 4.5 eV with a band gap of 0.5 eV [31] and metallic SWCNTs with a zero bandgap [32] have a work function of nearly 5.0 eV. On forming a composite film with PEDOT:PSS, the SWCNT network is doped, thereby increasing the work function of semiconducting SWCNTs. This is confirmed by the KPFM measurements of the composite film with a work function of 4.95 eV, which is close to the metallic SWCNTs' work

function. When this composite film comes into contact with i:a-Si:H (Fermi level position of 4.70 eV) [33], the Schottky barrier is reduced across the a-Si:H/SWCNT interface. Further, since the thickness of the SWCNT film increases beyond 19 nm, the transmittance decreases, which leads to a lower absorption and the reduced photo-generated carriers in the i:a-Si:H. In addition, as the SWCNT film thickness increases, PEDOT:PSS is not evenly distributed along the thickness of the SWCNTs. This possibly results in two recombination centers at the SWCNTs/PEDOT:PSS and SWCNTs/a-Si:H interfaces. Thus, the concentration of the generated hole carriers is lower for CNT40, CNT60, CNT80, and CNT100. It is worth mentioning that in our approach, the optimized composite film of PEDOT:PSS and SWCNT not only increases the effective contact area of a-Si by forming a continuous heterojunction, but also stimulates the holes in PEDOT:PSS to be transferred to the interconnected SWCNT network, due to the higher charge carrier mobility and low sheet resistance of SWCNTs along with their one-dimensional axis [34, 35]. Thus, PEDOT:PSS and SWCNT together facilitate the hole transport from a-Si [23]. Compared to all the previously reported work [20–22], we made use of the combined effect of SWCNTs and PEDOT:PSS to attain better and higher J - V characteristics of HSC. It is also the reason for the state-of-the-art performance of the HSCs fabricated in our work.

3.4. PMMA as an encapsulating and antireflective layer

PMMA was used to protect the device from any surface modification under ambient conditions. PMMA has a transmittance close to 100% over a wide wavelength, where a-Si:H generates photo-induced carriers. The fabrication process shown in figure 1 was modified and the last step of PMMA drop-casting was added (figure 1(a)—step vi). A 2 μ l quantity of PMMA solution was drop-casted onto the fabricated CNT20 device, so that the active area of the cell was uniformly coated. The device was placed on a hot plate at 90 °C for 20 min to ensure solvent evaporation.

The thickness of the PMMA layer was measured to be 300 nm from the cross-section SEM image (figure 5). The J - V characteristics comparison of the CNT20 HSC device both with PMMA and without PMMA is shown in figure 7(a) and tabulated in table 4. Compared to the values reported in section 3.3, the sample CNT20 with PMMA attained $\eta = 3.36 \pm 0.30\%$, FF = $41.8 \pm 3\%$, $J_{sc} = 8.99 \pm 0.10$ mA cm⁻², and $V_{oc} = 0.896 \pm 0.040$ V. An enhancement amounting to 10% was observed with PMMA in PCE, J_{sc} , and V_{oc} . The dark state curve shown in figure 7(a) gives the reverse saturation current density of $J_0 = 8.04 \pm 0.01 \times 10^{-4}$ mA cm⁻², the shunt resistance of $R_p = 350 \pm 1$ M Ω /cm², the series resistance of $R_s = 21 \pm 2$ k Ω /cm², and a diode ideality factor of $n = 1.06 \pm 0.03$, i.e. close to the ideal diode factor, hinting at a reduced carrier recombination. The EQE curves of CNT20 with and without PMMA are shown in figure 7(b). The EQE value saturates at 47.1%, demonstrating an increase of almost 10% compared to the device without PMMA. The EQE response is significantly

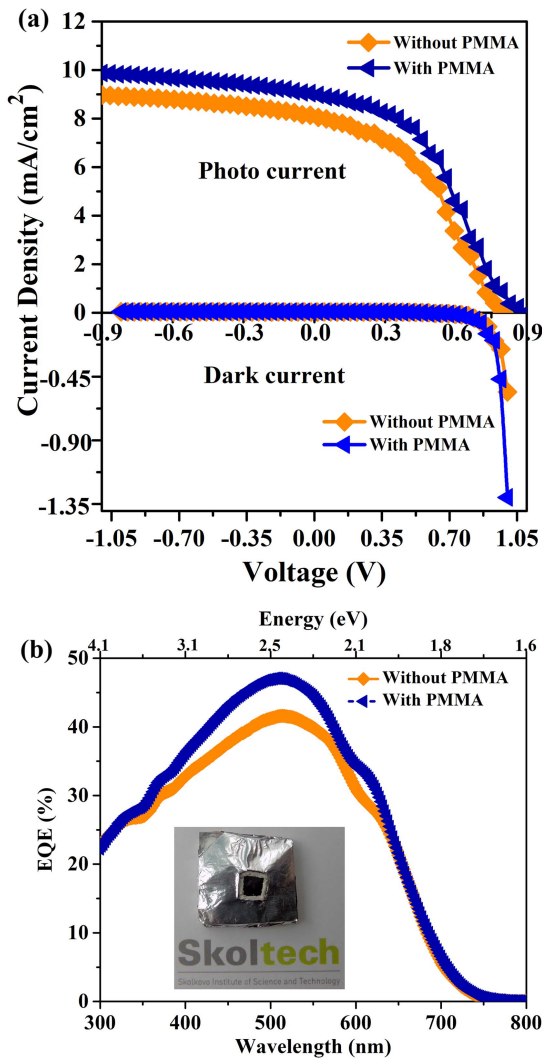


Figure 7. Characteristics of HSCs fabricated with CNT20 sample: (a) J - V curve comparison without Polymethylmethacrylate (PMMA) and with PMMA for photo and dark current response; (b) EQE spectra comparison without PMMA and with PMMA.

Table 4. Comparison of J - V parameters of HSC fabricated with CNT20 sample without PMMA and with PMMA.

Conditions	V_{oc} (V)	J_{sc} (mA cm ⁻²)	FF (%)	η (%)
Without PMMA	0.820	7.90	41.5	2.704
With PMMA	0.896	8.99	41.8	3.360

enhanced for a wavelength range from 320 to 640 nm. A sharp increase in the EQE value with PMMA, from 24% at 318 nm to 47% at 500 nm, indicates enhanced light absorption and photo generation in the i-a-Si:H.

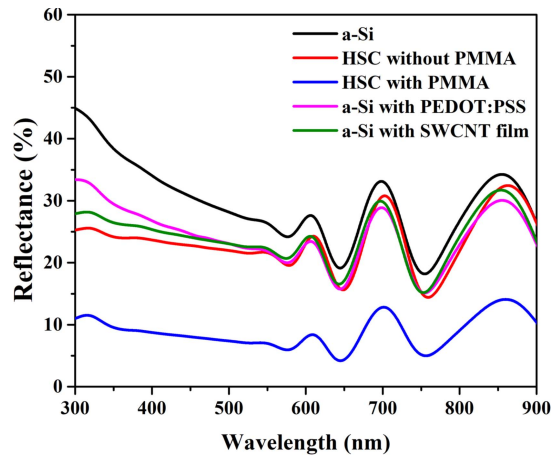


Figure 8. Reflectance spectra of plain a-Si:H, HSC without PMMA, HSC with PMMA, a-Si:H with PEDOT:PSS, and a-Si:H with SWCNT film.

Furthermore, the use of PMMA as an antireflective coating (ARC) has been a topic of interest, and several works have focused on the use of a PMMA layer acting as a broad band ARC over Si-CNT solar cells [36–38]. Hence, we carried out diffuse reflectance measurements to test the effect of PMMA as an ARC in our solar cell. The reflectance spectra of plain a-Si:H, a-Si:H with SWCNTs, a-Si:H with PEDOT:PSS, HSC without PMMA, and HSC with PMMA are shown in figure 8. The a-Si:H surface with textures exhibits about 20% minimum reflectance ranging from 500–800 nm. The reflection minima of the HSC without PMMA are slightly lower than those of plain a-Si:H, at about 16% in the visible region. The minimum reflectance of a-Si:H with PEDOT:PSS and a-Si:H with SWCNTs is lower than that of plain a-Si:H and is similar to the reflectance of HSC without PMMA.

Additionally, we can observe a red shift at wavelengths corresponding to the maximum reflectance between 700–900 nm for HSC without PMMA. A similar observation for C-Si was made by Fan *et al* wherein the red shift was attributed to the increase in the thickness of a PEDOT:PSS-CNT composite film when incorporating the CNT network [15]. Therefore, the thickness of the PEDOT:PSS in the composite film should be optimized to give rise to more photo-generated carriers triggered by the increase in light absorption of a-Si:H. Moreover, it is notable to see that the incorporation of PEDOT:PSS and SWCNT film on an a-Si surface reduces the reflectance. This is caused by the antireflection effect of PEDOT:PSS and SWCNTs. Further, HSC with PMMA shows a reduction to about 4.5% reflectance in the visible region. Consequently, PMMA as an effective ARC increases the light trapping efficiency, producing more photo-generated carriers and thus increasing the current density and HSC efficiency.

4. Conclusion

In this work, we demonstrate a low-cost and environmentally friendly process technology for the fabrication of a SWCNT/a-Si:H hybrid PV device that uses SWCNTs with an enhanced conductivity by PEDOT:PSS as a window layer and front electrode. The dry transfer technique and drop-casting method are fully compatible with roll-to-roll manufacturing in the future market integration of low-cost flexible solar cells. A PCE of 2.7% is exhibited for such a thin film hybrid device. PMMA incorporation reduces the reflection of the HSC fourfold and enhances the short-circuit J_{sc} and PCE by nearly 10%. The state-of-the-art performance, with a PCE of 3.4%, is recorded for this HSC. This kind of HSC is promising for future fabrication of low-cost flexible thin film CNT based HSCs.

Acknowledgments

The authors acknowledge the financial support from the Ministry of Education and Science of the Russian Federation (project RFMEFI61815X0003), from the Estonian Research Council (project ETAG15028) and from the German Federal Ministry of Education and Research (BMBF, reference number 01DJ15030) within the joint project FLEXAPP in a framework of ERA.Net RUS Plus program.

ORCID iDs

Pramod M Rajanna  <https://orcid.org/0000-0002-6175-4442>

References

- [1] Shah A V 2010 *Thin-Film Silicon Solar Cells* (Lausanne: EPFL Press) pp 1–10
- [2] Williams E L, Jabbar G E, Wang Q, Shaheen S E, Ginley D S and Schiff E A 2005 Conducting polymer and hydrogenated amorphous silicon hybrid solar cells *Appl. Phys. Lett.* **87** 223504
- [3] Alet P J, Palacin S, Cabarrocas P R, Kalache B, Firon M and de Bettignies R 2007 Hybrid solar cells based on thin-film silicon and P3HT—a first step towards nano-structured devices *Eur. Phys. J. Appl. Phys.* **36** 231–4
- [4] Gowrishankar V, Scully S R, McGehee M D, Wang Q and Branz H M 2006 Exciton splitting and carrier transport across the amorphous-silicon/polymer solar cell interface *Appl. Phys. Lett.* **89** 252102
- [5] Pei Z, Thiyyagu S, Jhong M S, Hsieh W S, Cheng S J, Ho M W, Chen Y H, Liu J C and Yeh C M 2011 An amorphous silicon random nanocone/polymer hybrid solar cell *Sol. Energy Mater. Sol. Cells* **95** 2431–6
- [6] Yun M H, Jang J H, Kim K M, Song H, Lee J C and Kim J Y 2013 A hybrid solar cell fabricated using amorphous silicon and a fullerene derivative *Phys. Chem. Chem. Phys.* **15** 19913
- [7] Schaefer S *et al* 2014 Electric field distribution in hybrid solar cells comprising an organic donor polymer and amorphous silicon *Org. Photonics Photovolt.* **2** 12–20
- [8] Dosenovicova D, Maricheva J, Neumüller A, Sergeev O, Volobujeva O, Nasibulin A G, Kois J, Öpik A and Bereznev S 2017 Selective photoelectrochemical deposition of polypyrrole onto hydrogenated a-Si for optoelectronic applications *Mater. Sci. Semicond. Process.* **68** 1–5
- [9] Nicola F D *et al* 2017 100% internal quantum efficiency in polychiral single-walled carbon nanotube bulk heterojunction/silicon solar cells *Carbon* **114** 402–10
- [10] Wang F, Kozawa D, Miyauchi Y, Hiraoka K, Mouri S, Ohno Y and Matsuda K 2015 Considerably improved photovoltaic performance of carbon nanotube-based solar cells using metal oxide layers *Nat. Commun.* **6** 6305
- [11] Zhang Y F, Wang Y F, Chen N, Wang Y Y, Zhang Y Z, Zhou Z H and Wei L M 2010 Photovoltaic enhancement of Si solar cells by assembled carbon nanotubes *Nano-Micro Lett.* **2** 22–5
- [12] Landi B J, Raffaele R P, Castro S L and Bailey S G 2005 Single-wall carbon nanotube–polymer solar cells *Prog. Photovolt., Res. Appl.* **13** 165–72
- [13] Aitola K *et al* 2017 High temperature-stable perovskite solar cell based on low-cost carbon nanotube hole contact *Adv. Mater.* **29** 1606398
- [14] Khatri I, Tang Z G, Liu Q M, Ishikawa R, Ueno K and Shirai H 2013 Green-tea modified multi-walled carbon nanotubes for efficient poly(3,4-ethylenedioxythiophene) poly(styrenesulfonate)/n-silicon hybrid solar cell *Appl. Phys. Lett.* **102** 063508
- [15] Fan Q *et al* 2017 Novel approach to enhance efficiency of hybrid silicon-based solar cells via synergistic effects of polymer and carbon nanotube composite film *Nano Energy* **33** 436–44
- [16] Ren S, Bernardi M, Lunt R R, Bulovic V, Grossman J C and Gradecak S 2011 Towards efficient carbon nanotube/P3HT solar cells: active layer morphology, electrical, and optical properties *Nano Lett.* **11** 5316–21
- [17] Kymakis E and Amaratunga G A J 2002 Single-wall carbon nanotube/conjugated polymer photovoltaic devices *Appl. Phys. Lett.* **80** 112–4
- [18] Du J, Bittner F, Hecht D S, Ladous C, Ellinger J, Oekermann T and Wark M 2013 A carbon nanotube-based transparent conductive substrate for flexible ZnO dye-sensitized solar cells *Thin Solid Films* **531** 391–7
- [19] Kyaw A K K *et al* 2011 Dye-sensitized solar cell with a titanium-oxide-modified carbon nanotube transparent electrode *Appl. Phys. Lett.* **99** 021107
- [20] Schriver M, Regan W, Loster M and Zettl A 2010 Carbon nanostructure–aSi:H photovoltaic cells with high open-circuit voltage fabricated without dopants *Solid State Commun.* **150** 561–3
- [21] Gobbo S D, Castrucci P, Scarselli M, Camilli L, Crescenzi M D, Mariucci L, Valletta A, Minotti A and Fortunato G 2011 Carbon nanotube semitransparent electrodes for amorphous silicon based photovoltaic devices *Appl. Phys. Lett.* **98** 183113
- [22] Funde A M *et al* 2016 Carbon nanotube–amorphous silicon hybrid solar cell with improved conversion efficiency *Nanotechnology* **27** 185401
- [23] Alekseeva A K, Rajanna P M, Anisimov A S, Sergeev O, Bereznev S and Nasibulin A G 2018 Synergistic effect of single-walled carbon nanotubes and PEDOT:PSS in thin film amorphous silicon hybrid solar cell *Phys. Status Solidi b* **255** 1700557
- [24] Nasibulin A G *et al* 2011 Free-standing single-walled carbon nanotube films *ACS Nano* **5** 3214–21
- [25] Moiala A, Nasibulin A G, Brown D P, Jiang H, Khriachtchev L and Kauppinen E I 2006 Single-walled carbon nanotube synthesis using ferrocene and iron pentacarbonyl in a laminar flow reactor *Chem. Eng. Sci.* **61** 4393–402

- [26] Tian Y, Timmermans M, Kivistö S, Nasibulin A, Zhu Z, Jiang H, Okhotnikov O and Kauppinen E 2011 Tailoring the diameter of single-walled carbon nanotubes for optical applications *Nano Res.* **4** 807–15
- [27] Pal P P *et al* 2015 Dry functionalization and doping of single-walled carbon nanotubes by ozone *J. Phys. Chem. C* **119** 27821–8
- [28] Gorkina A L *et al* 2016 Transparent and conductive hybrid graphene/carbon nanotube films *Carbon* **100** 501–7
- [29] Neumüller A, Bereznev S, Ewert M, Volobujeva O, Sergeev O, Falta J, Vehse M and Agert C 2016 Carrier collection losses in interface passivated amorphous silicon thin-film solar cells *Appl. Phys. Lett.* **109** 043903
- [30] Abou-Ras D, Kirchartz T and Rau U 2016 *Advanced Characterization Techniques for Thin Film Solar Cells* vol 1 2nd edn (New York: Wiley) pp 55–66
- [31] Kaskela A *et al* 2010 Aerosol-synthesized SWCNT networks with tunable conductivity and transparency by a dry transfer technique *Nano Lett.* **10** 4349–55
- [32] Deslippe J, Spataru C D, Prendergast D and Louie S G 2007 Bound excitons in metallic single-walled carbon nanotubes *Nano Lett.* **7** 1626
- [33] Schropp R and Zeman M 1998 *Amorphous and Microcrystalline Silicon Solar Cells: Modelling, Materials and Device Technology* vol 5 (Dordrecht: Kluwer)
- [34] Fuhrer M S, Kim B M, Durkop T and Brintlinger T 2002 High-mobility nanotube transistor memory *Nano Lett.* **2** 755–9
- [35] Snow E S, Campbell P M, Ancona M G and Novak J P 2005 High-mobility carbon-nanotube thin-film transistors on a polymeric substrate *Appl. Phys. Lett.* **86** 033105
- [36] Li X, Yu X and Han Y 2013 Polymer thin films for antireflection coatings *J. Mater. Chem. C* **1** 2266–85
- [37] Li R, Di J, Yong Z, Sun B and Li Q 2014 Polymer thin films for antireflection coatings *J. Mater. Chem. A* **2** 4140–3
- [38] Yu L, Tune D D, Shearer C J and Shapter J G 2015 Implementation of antireflection layers for improved efficiency of carbon nanotube–silicon heterojunction solar cells *Sol. Energy* **118** 592–9

Publication 3

Alena K. Alekseeva¹, **Pramod Mulbagal Rajanna**^{1*}, Anton S. Anisimov, Oleg Sergeev, Sergei Bereznev, and Albert G. Nasibulin*. Synergistic Effect of Single-Walled Carbon Nanotubes and PEDOT:PSS in Thin Film Amorphous Silicon Hybrid Solar Cell. *Phys. Status Solidi B* 2018, 255, 1700557. DOI: 10.1002/pssb.201700557.

© 2017 WILEY-VCH Verlag GmbH & Co. KGaA, Weinheim.
Reprinted with permission

Synergistic Effect of Single-Walled Carbon Nanotubes and PEDOT:PSS in Thin Film Amorphous Silicon Hybrid Solar Cell

Alena K. Alekseeva, Pramod Mulbagal Rajanna,* Anton S. Anisimov, Oleg Sergeev, Sergei Bereznev, and Albert G. Nasibulin*

We propose a simple fabrication method of thin film hybrid solar cells by combining single-walled carbon nanotubes (SWCNTs) and poly(3,4-ethylenedioxythiophene) polystyrene sulfonate (PEDOT:PSS) with hydrogenated amorphous silicon (a-Si:H). Electrically conductive polymer PEDOT:PSS introduced in a randomly oriented network of SWCNTs forms a coupled continuous heterojunction between PEDOT:PSS–SWCNT and a-Si:H. We fabricated and compared the performance of SWCNT/a-Si:H, PEDOT:PSS/a-Si:H and PEDOT:PSS–SWCNT/a-Si:H solar cells. The PEDOT:PSS–SWCNT/a-Si:H solar cells resulted to have an efficiency of 1.6% with state-of-the-art fill factor and open circuit voltage of 54% and 0.803 V, respectively.

1. Introduction

Under current development of solar cells, thin film technology with minimum material consumption allows fabrication of low cost devices. Amorphous silicon (a-Si) is promising material due to its unique mechanical, electrical and optical properties, which

A. K. Alekseeva, P. M. Rajanna, Prof. A. G. Nasibulin
Skolkovo Institute of Science and Technology
Nobel str. 3, Moscow 143026, Russia
E-mail: pramod.rajan@skolkovotech.ru; a.nasibulin@skoltech.ru

Dr. A. S. Anisimov
Canatu Oy
Konalankuja 5, FI-00390 Helsinki, Finland

Dr. O. Sergeev
DLR Institute of Networked Energy Systems
German Aerospace Center (DLR)
Carl-von-Ossietzky-Straße 15, 26129 Oldenburg, Germany

Dr. S. Bereznev
Department of Materials and Environmental Technology
Tallinn University of Technology
Ehitajate tee 5, 19086 Tallinn, Estonia

Prof. A. G. Nasibulin
Department of Applied Physics
Aalto University
P.O. Box 15100, FI-00076 Espoo, Finland

 The ORCID identification number(s) for the author(s) of this article can be found under <https://doi.org/10.1002/pssb.201700557>.

Alena K. Alekseeva and Pramod Mulbagal Rajanna have contributed equally.

DOI: 10.1002/pssb.201700557

makes them compatible with roll-to-roll manufacturing and flexible device concept. Solar cells based on hydrogenated amorphous silicon (a-Si:H) usually have either p-i-n or n-i-p architecture. The presence of intrinsic layer is essential for extended electric field at the origin of photo-generation between the p- and n-layers. This assists in carrier travel and immediate separation of electrons and holes to avoid recombination due to extremely short travel distances caused by shorter lifetime of photo-generated carriers in a-Si:H. Typically in a-Si:H thin film, the p-doped layer is obtained by plasma enhanced chemical vapor deposition of gas mixture containing toxic diborane (B_2H_6) gas at relatively high temperature.

An alternative to replace p-a-Si:H layer is a SWCNT film. Exposed to air, SWCNTs absorb oxygen and becomes p-type semiconductor.^[1,2] The optoelectrical, chemical and mechanical properties of SWCNTs make them applicable in solar cells as a p-layer.^[3–8] SWCNT films on a contact with i-a-Si:H layer form heterojunction. It is important to have a continuous contact between SWCNTs and a-Si:H for an optimum charge transfer. If otherwise, it results in a very high resistance at the SWCNT/a-Si:H interface and extremely poor $J-V$ characteristics. Several studies have reported hybrid solar cells based on amorphous silicon with SWCNTs exhibiting poor $J-V$ characteristics, where fill factor (FF) and open circuit voltage (V_{oc}) equals only to 20% and 0.35 V,^[9] 19% and 0.5 V,^[10] 28% and 0.3 V,^[11] respectively.

In this paper, in order to obtain heterojunctions with continuous contact between SWCNT and a-Si:H we introduced an electrically conductive polymer poly(3,4-ethylenedioxythiophene) polystyrene sulfonate (PEDOT:PSS) in the SWCNT films. We compared the photovoltaic performance of SWCNT/a-Si:H, PEDOT:PSS/a-Si:H and PEDOT:PSS-SWCNT/a-Si:H solar cells. The combination of SWCNTs and PEDOT:PSS have better $J-V$ performance with the state-of-the-art performance of $FF = 54\%$ and $V_{oc} = 0.803$ V for such type of devices.

2. Experimental Section

In the current study three types of solar cells were fabricated at the same conditions: SWCNT/a-Si:H, PEDOT:PSS/a-Si:H and

PEDOT:PSS-SWCNT/a-Si:H. The fabrication process of the hybrid devices are as described. Al:ZnO, used as a back contact, was deposited on the glass substrates by sputtering. Plasma enhanced chemical vapor deposition (PECVD) with silane (SiH₄), hydrogen (H₂) and phosphine (PH₃) was used for deposition of n-doped (30 nm thickness) and intrinsic (250 nm thickness) layers of hydrogenated amorphous silicon on top of the Al:ZnO. In order to open the back contact, 6M of KOH aqueous solution was drop-casted on top of the a-Si:H layers. The speed of chemical reaction of KOH with a-Si:H was increased by heating the substrates up to 160 °C on the hot plate. After 5 s, KOH was removed with distilled water. The obtained resistivity of the back contact was around 17 ohms-cm. Subsequently, natural oxide layer on a-Si:H was removed by HF vapor treatment for 10 s.

SWCNTs were synthesized by an aerosol chemical vapor deposition method described elsewhere.^[12,13] SWCNT films collected on a nitrocellulose filter at the outlet of the reactor are a mixture of metallic and semiconducting nanotubes, which exposed to air, demonstrates p-type conductivity. Thickness of the film was controlled by the collection time. SWCNT films with thickness of 60 nm were deposited on i-a-Si:H films using dry deposition method.^[14,15]

An electrically conductive PEDOT:PSS polymer, was chosen for application in SWCNT/i-a-Si:H heterojunction due to its high hole mobility and environmental stability. PEDOT:PSS was spin coated on top of the SWCNT/i-a-Si:H structures for 90 s at 3000 rpm with an acceleration speed of 800 rpm s⁻¹ from the mixture of aqueous suspension of 5 ml PEDOT:PSS (1.3 wt.% Sigma-Aldrich) with glycerine, N-methylpyrrolidone and isopropanol (IPA) in a ratio of 1:2:19 respectively.

Lastly, to evaporate residues from the solvent and to activate the acceptor states of the polymer^[16] the devices were annealed on the hot plate at a temperature of 160 °C for 10 min. Subsequent to annealing rectangular shaped front contacts were made at the edges out of silver paste on top of the structure. To harden the front contacts the devices were annealed at 160 °C for 5 min on the hot plate. The active area of the solar cells was around 0.5 cm². The schematic structure of the completed device is shown in Figure 1(a).

The current density–voltage (*J*–*V*) characteristics, which determine the performance of the fabricated solar cells, were obtained by a source-measure unit Keithley 2400 in a solar simulator Newport Corporation, Oriel Sol3A Class AAA (AM

1.5G illumination, intensity 100 mW cm⁻², temperature 25 °C). The external quantum efficiency (EQE) of the hybrid solar cells was measured using spectral response measurement system Bentham PVE300. The cross-section of PEDOT:PSS-SWCNT/a-Si solar cell was explored with Carl Zeiss NEON 40 EsB field emission SEM combining GEMINI lens design with an advanced Canion FIB column (equipped with Gallium liquid metal ion source). Prior to investigation, the sample was coated with thin metal contrast layer. The cross-section was formed with focused ion beam at 2 μA emission current, 30 kV acceleration voltage and 10 nA of milling current. Multi-step polishing was performed at milling currents from 200 to 20 pA. The SEM image was obtained at 20 kV acceleration voltage using in-lens secondary electron detectors. The work function was measured using Kelvin Probe Force Microscopy from Asylum Research – Cypher ES. Figure 1(b) show the cross-section SEM image.

3. Results and Discussion

The current density–voltage (*J*–*V*) characteristics of the three types of hybrid solar cells: PEDOT:PSS-SWCNT/a-Si:H, PEDOT:PSS/a-Si:H and SWCNT/a-Si:H were measured in the dark (Figure 2a) and under illumination (Figure 2b) with inset of a fabricated hybrid solar cell. We hereby clarify that only the best working cells are reported here for each of the three types of hybrid solar cells. The *J*–*V* characteristics measured in the dark clearly reveals the diode properties for all the three types of hybrid solar cells. Analyzing the dark *J*–*V* curve for all three types of solar cells, PEDOT:PSS-SWCNT/a-Si:H solar cell exhibits a higher reverse saturation current density (*J*₀) than the other two solar cells, while the shunt resistance (*R*_p), series resistance (*R*_s) and diode ideality factor (*n*) are nearly the same. The calculated values for PEDOT:PSS-SWCNT/a-Si:H solar cell are respectively *J*₀ = 3.40 ± 0.01 × 10⁻⁴ mA cm⁻², *R*_p = 75.0 ± 0.5 MΩ cm⁻², *R*_s = 30.0 ± 0.5 kΩ cm⁻², and *n* = 1.05 ± 0.05.

The *J*–*V* curve shifts under illumination showing a typical photovoltaic behavior for all the three hybrid solar cells. However, solar cell with PEDOT:PSS-SWCNT and a-Si:H shows more desirable *J*–*V* characteristics than those with only PEDOT:PSS or SWCNT film. The PEDOT:PSS-SWCNT/a-Si:H solar cell exhibits a better performance: a short-circuit current-density of *J*_{sc} = 3.56 ± 0.10 mA cm⁻², an open-circuit voltage of *V*_{oc} = 0.803 ± 0.003 V, a fill factor of FF = 54 ± 3% and a

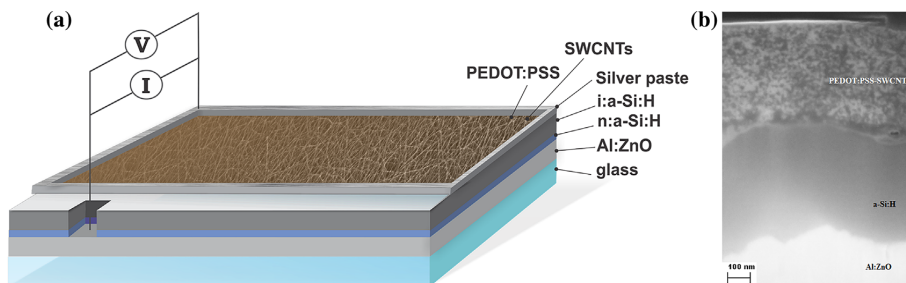


Figure 1. (a) Fabricated PEDOT:PSS-SWCNT/a-Si:H solar cell; (b) cross-section SEM image of a PEDOT:PSS-SWCNT/a-Si:H solar cell.

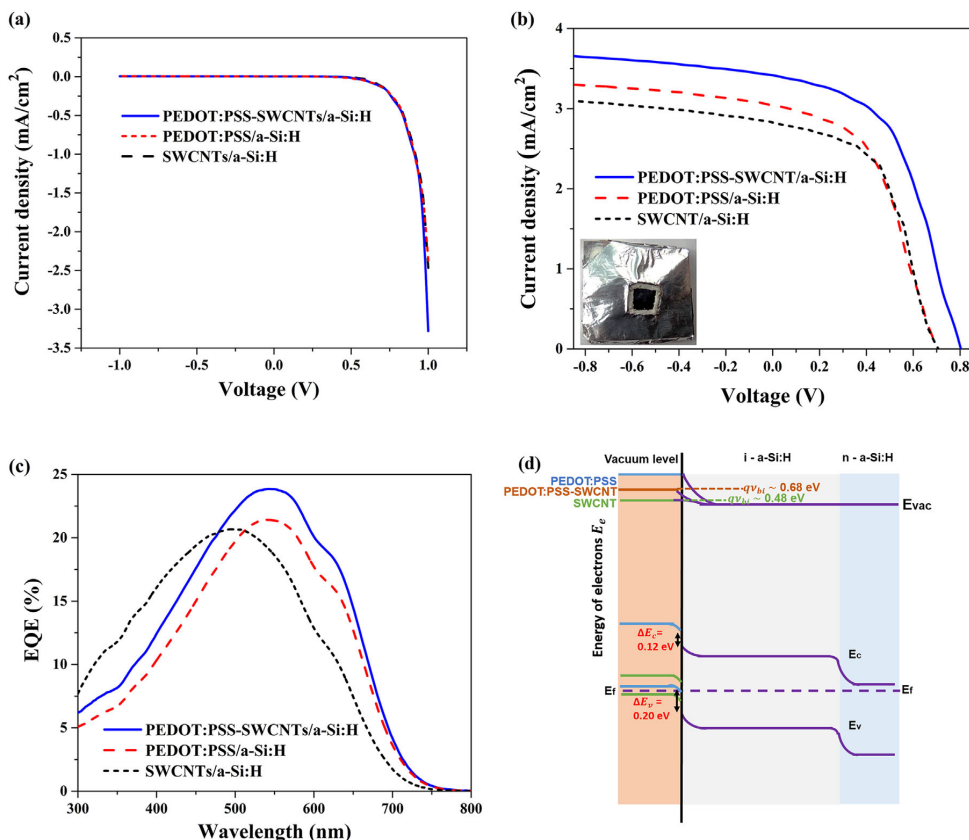


Figure 2. (a) Dark and (b) photo J - V characteristics of PEDOT:PSS-SWCNT/a-Si:H, PEDOT:PSS/a-Si:H and SWCNT/a-Si:H hybrid solar cells, with inset of a fabricated PEDOT:PSS-CNT/a-Si hybrid solar cell. (c) EQE spectrum; (d) schematic band diagram of the fabricated devices with the band offset at PEDOT:PSS/i-a-Si:H marked in red.

efficiency of $\eta = 1.57 \pm 0.03\%$. Whereas, for the PEDOT:PSS/a-Si:H and SWCNT/a-Si:H solar cells J_{sc} equal to 3.03 ± 0.10 and $2.80 \pm 0.10 \text{ mA cm}^{-2}$, V_{oc} equal to 0.710 ± 0.003 and $0.700 \pm 0.003 \text{ V}$, FF equal to $40.4 \pm 3.0\%$ and $45.2 \pm 3.0\%$, and η equal to $1.03 \pm 0.03\%$ and $1.10 \pm 0.03\%$, respectively (Table 1). It is worth noting that fill factor and open circuit voltage of PEDOT:PSS-SWCNT/a-Si:H hybrid solar cell is found to be the state-of-the-art exceeding previously reported amorphous silicon hybrid solar cells using either SWCNTs or conductive polymer.^[9–11,17–20] This can be explained by the introduction of

Table 1. J - V parameters of the fabricated solar cells: open-circuit voltage (V_{oc}), short-circuit current density (J_{sc}), fill factor (FF), and power conversion efficiency (η).

Sample name	V_{oc} (V)	J_{sc} (mA cm^{-2})	FF (%)	η (%)
PEDOT:PSS-SWCNT/a-Si:H	0.803	3.56	54.0	1.57
PEDOT:PSS/a-Si:H	0.710	3.03	40.4	1.03
SWCNT/a-Si:H	0.700	2.80	45.2	1.10

PEDOT:PSS which fills the micropores of SWCNT film and forms continuous contact with i-a-Si:H. This leads to the formation of coupled heterojunctions between SWCNT/i-a-Si:H and PEDOT:PSS/i-a-Si:H rather than a usual single-heterojunction between SWCNT/i-a-Si:H as has been previously reported. Thus, in the PEDOT:PSS-SWCNT/i-a-Si:H solar cell, beyond the heterojunctions formed by PEDOT:PSS and SWCNT individually, their combined effect is more important. As shown in Figure 2 (d), the work function of SWCNT film, PEDOT:PSS and PEDOT:PSS-SWCNT composite film are 4.6, 5.2, and 4.85 eV, respectively. The i-a-Si:H Fermi level position and mobility gap is taken from the literature.^[21] The HOMO-LUMO gap of the PEDOT:PSS is estimated to be 1.5 eV.^[22] The Fermi level offset between the PEDOT:PSS-SWCNT composite film produces a built-in voltage (V_{bi}) of about 0.7 V, which is larger than that of a SWCNT network and PEDOT:PSS individually. The estimated V_{bi} is close to the measured V_{oc} of PEDOT:PSS-SWCNT/i-a-Si:H and SWCNT/i-a-Si:H solar cells. Moreover, the high V_{oc} in PEDOT:PSS/i-a-Si:H solar cell can be attributed to the high band gap of PEDOT:PSS, while the lower FF is possibly

due to the high resistivity of PEDOT:PSS film and stronger recombination near the V_{oc} . A similar observation for C-Si has been reported by Hu et al. for PEDOT:PSS/Si nanowire hybrid solar cell.^[23]

External quantum efficiency (EQE) measurements of all the three types of hybrid solar cells are shown in Figure 2(c). EQE spectrum for PEDOT:PSS-SWCNT/a-Si:H shows a higher EQE saturation value of 24% than the other two solar cells. Additionally, for SWCNT/a-Si:H solar cell shows a strong blue-shift which can be due to the strong absorbance of SWCNTs. However, all three EQE spectra of the hybrid solar cells resembles to the standard a-Si:H solar cell in a wavelength of 300–800 nm. The current density from EQE and J - V curve are in close match for all three solar cells. The sharp decrease in the EQE beyond 700 nm can be attributed to the a-Si:H mobility gap (1.7 eV).

Combining the J - V parameters and EQE, the following analysis was made. The fabricated solar cell of PEDOT:PSS-SWCNT/a-Si:H exhibits the state-of-the-art fill factor and open circuit voltage; while the current density is lower due to an increased absorption of incident photons at the PEDOT:PSS-SWCNT layer (p-layer). Hence, the p-layer needs to be optimized in order to increase absorption and photo-generation of charge carriers in the i-a-Si:H. This potentially will lead to a higher photo-generated current density and efficiency.

4. Conclusion

We presented the fabrication method of a hybrid thin film amorphous silicon solar cell with p-layer from a combination of PEDOT:PSS and SWCNTs. The micropores in the SWCNTs were filled by PEDOT:PSS providing a continuous junction of the PEDOT:PSS-SWCNT mixture with a-Si:H. We exploited the synergistic effect of combination of PEDOT:PSS with SWCNTs on the properties of solar cells. We fabricated a PEDOT:PSS-SWCNT/a-Si:H hybrid solar cell with a state-of-the-art FF = 54% and V_{oc} = 0.803 V, based on analysis of three types of solar cells fabricated under the same conditions. The efficiency of the as-designed PEDOT:PSS-SWCNT/a-Si:H solar cell is 1.6%, which has been enhanced by about 31% and 38% in comparison to the SWCNT/a-Si:H (1.1%) and PEDOT:PSS/a-Si:H (1%) solar cell fabricated using the same materials, respectively. Our current approach with the proposed materials makes the cells compatible to a roll-to-roll manufacturing process and allows utilizing them for flexible applications.

Acknowledgements

This work is supported by the Ministry of Education and Science of the Russian Federation through ERA-NET project (agreement 14.618.21.0003; identification number RFME-F161815 × 0003). The authors also would like to acknowledge financial support from Estonian Research Council (project ETAG15028) and from German Federal Ministry of Education and Research (project BMBF, reference number 01DJ15030).

Conflict of Interest

The authors declare no conflict of interest.

Keywords

amorphous materials, PEDOT:PSS, silicon, single-walled carbon nanotubes, solar cells, thin films

Received: October 1, 2017

Revised: November 16, 2017

Published online: December 11, 2017

- [1] A. Javey, J. Guo, Q. Wang, M. Lundstrom, H. Dai, *Nature* **2003**, 424, 654.
- [2] Z. Yao, C. Kane, C. Dekker, *Phys. Rev. Lett.* **2000**, 84, 13.
- [3] H. Kataura, Y. Kumazawa, Y. Maniwa, I. Umezuo, S. Suzuki, Y. Ohtsuka, Y. Achiba, *Synth. Met.* **1999**, 103, 1.
- [4] K.-R. Chen, H.-F. Yeh, H.-C. Chen, T.-J. Liu, S.-J. Huang, P.-Y. Wu, C. Tiu, *Adv. Chem. Eng. Sci.* **2013**, 3, 3.
- [5] J.-C. Blancon, M. Paillet, H. N. Tran, X. T. Than, S. A. Guebrou, A. Ayari, A. S. Miguel, N. M. Phan, A.-A. Zahab, J.-L. Sauvajol, N. D. Fatti, F. Vallee, *Nat. Commun.* **2013**, 4, 2542.
- [6] A. Krishnan, E. Dujardin, T. W. Ebbesen, P. N. Yianilos, M. M. J. Treacy, *Phys. Rev. B* **1998**, 58, 20.
- [7] F. Li, H. M. Cheng, S. Bai, G. Su, M. S. Dresselhaus, *Appl. Phys. Lett.* **2000**, 77, 3161.
- [8] P. P. Pal, T. Larionova, I. V. Anoshkin, H. Jiang, M. Nisula, A. A. Goryunkov, O. V. Tolochko, M. Karppinen, E. I. Kauppinen, A. G. Nasibulin, *J. Phys. Chem. C* **2015**, 119, 49.
- [9] M. Schriver, W. Regan, M. Loster, A. Zettl, *Solid State Commun.* **2010**, 150, 13.
- [10] S. Del Gobbo, P. Castrucci, M. Scarselli, L. Camilli, M. De Crescenzi, L. Mariucci, A. Valletta, A. Minotti, G. Fortunato, *Appl. Phys. Lett.* **2011**, 98, 183113.
- [11] A. M. Funde, A. G. Nasibulin, H. G. Syed, A. S. Anisimov, A. Tsapenko, P. Lund, J. D. Santos, I. Torres, J. J. Gandia, J. Cárabe, A. D. Rozenberg, I. A. Levitsky, *Nanotechnology* **2016**, 27, 185401.
- [12] A. G. Nasibulin, A. Kaskela, K. Mustonen, A. S. Anisimov, V. Ruiz, S. Kivisto, S. Rackauskas, M. Y. Timmermans, M. Pudas, B. Aitchison, M. Kauppinen, D. P. Brown, O. G. Okhotnikov, E. I. Kauppinen, *ACS Nano* **2011**, 5, 3214.
- [13] A. Moisala, A. G. Nasibulin, D. P. Brown, H. Jiang, L. Khriachtchev, E. I. Kauppinen, *Chem. Eng. Sci.* **2006**, 61, 4393.
- [14] M. Adachi, S. Tsukui, K. Okuyama, *J. Nanoparticle Res.* **2003**, 5, 1.
- [15] M. Y. Zavodchikova, T. Kulmala, A. G. Nasibulin, V. Ermolov, S. Franssila, K. Grigoros, E. I. Kauppinen, *Nanotechnology* **2009**, 20, 8.
- [16] E. Vitoratos, S. Sakkopoulos, N. Paliatas, K. Emmanouil, S. A. Choulis, *Open J. Org. Polym. Mater.* **2012**, 2, 7.
- [17] Z. Pei, S. Thiyagu, M.-S. Jhong, W. S. Hsieh, S. J. Cheng, M. W. Ho, Y. H. Chen, J. C. Liu, C. M. Yeh, *Sol. Energy Mater. Sol. Cells* **2011**, 95, 2431.
- [18] M. H. Yun, J. H. Jang, K. M. Kim, H. Song, J. C. Lee, J. Y. Kim, *Chem. Phys.* **2013**, 15, 19913.
- [19] S. Schaefer, S. Albrecht, D. Neher, T. F. Schulze, E. Conrad, L. Korte, B. Rech, J. Würdenweber, A. Gordijn, U. Scherf, I. Dumsch, *Org. Photon. Photovolt.* **2014**, 2, 12.
- [20] D. Dosenovicova, J. Maricheva, A. Neumüller, O. Sergeev, O. Volobujeva, A. G. Nasibulin, J. Kois, A. Öpik, S. Bereznev, *Mater. Sci. Semicond. Process.* **2017**, 68, 1.
- [21] M. Mews, M. Liebhaber, B. Rech, L. Korte, *Appl. Phys. Lett.* **2015**, 107, 013902.
- [22] S. Jäckle, M. Mattiza, M. Liebhaber, G. Brönstrup, M. Rommel, K. Lips, S. Christiansen, *Sci. Rep.* **2015**, 5, 13008.
- [23] K. Y. Hu, C. K. Li, H. J. Syu, Y. Lai, C. F. Lin, Y. R. Wu, *J. Appl. Phys.* **2016**, 120, 215501.

Publication 4

Pramod M. Rajanna*, Hosni Meddeb, Oleg Sergeev, Alexey P. Tsapenko, Sergei Bereznev, Martin Vehse, Olga Volobujeva, Mati Danilson, Peter D. Lund*, Albert G. Nasibulin*. Rational design of highly efficient flexible and transparent p-type composite electrode based on single-walled carbon nano-tubes. *Nano Energy* 67 (2020) 104183. DOI: 10.1016/j.nanoen.2019.104183.

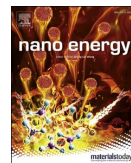
© 2019 Elsevier Ltd.

Reprinted with permission



Contents lists available at ScienceDirect

Nano Energy

journal homepage: <http://www.elsevier.com/locate/nanoen>

Full paper

Rational design of highly efficient flexible and transparent p-type composite electrode based on single-walled carbon nanotubes

Pramod M. Rajanna^{a,b,**}, Hosni Meddeb^c, Oleg Sergeev^c, Alexey P. Tsapenko^{a,b}, Sergei Bereznev^d, Martin Vehse^c, Olga Volobujeva^d, Mati Danilson^d, Peter D. Lund^{b,*}, Albert G. Nasibulin^{a,b,***}

^a Skolkovo Institute of Science and Technology, Skolkovo Innovation Center, Building 3, Moscow, 143026, Russia

^b Aalto University, P.O. Box 15100, FI-00076, Aalto, Espoo, Finland

^c DLR Institute of Networked Energy Systems, Carl-von-Ossietzky-Straße 15, 26129, Oldenburg, Germany

^d Tallinn University of Technology, Department of Materials and Environmental Technology, Ehitajate Tee 5, 19086, Tallinn, Estonia



ARTICLE INFO

Keywords:

Transparent p-type electrode
Flexible
Single-walled carbon nanotubes
Composite
Hybrid thin film solar cells

ABSTRACT

Transparent electrodes are of great importance in electronics and energy technologies. At present, transparent conductive oxides are mainly n-type conductors dominating the market and have restricted the technological advancements. Single-walled carbon nanotubes (SWCNTs) have recently emerged as promising p-type transparent conductor owing to their superior hole mobility, conductivity, transparency, flexibility and possibility to tune the work function. Here, we develop a novel rational design of p-type flexible transparent conductive film (TCF) based on SWCNTs combined with poly (3,4-ethylenedioxythiophene) polystyrene sulfonate (PEDOT:PSS), molybdenum oxide and SWCNT fibers. In a configuration of SWCNTs-MoO₃-PEDOT:PSS/SWCNT fibers, we achieved a record equivalent sheet resistance of 17 Ω/sq with a transmittance of 90% at 550 nm and a high degree of flexibility. We demonstrate that our solar cells developed on the basis of the proposed electrode and hydrogenated amorphous silicon (a-Si:H) yield an outstanding short-circuit current density of $J_{sc} = 15.03$ mA/cm² and a record power conversion efficiency of PCE = 8.8% for SWCNTs/a-Si:H hybrid solar cells. We anticipate that this novel rationally designed p-type TCF opens a new avenue in widespread energy technologies, where high hole conductivity and transparency of the material are prerequisites for their successful implementation.

1. Introduction

In last decades, transparent electrodes have played a key role in the scientific and technological development [1,2]. They are capable to simultaneously transmit light and conduct electrical current [1]. Currently, transparent conductive oxides, that make up the majority of transparent electrodes and are employed in practically all modern devices, are mainly degenerated n-type conductors [2]. An extensive research to find effective p-type conductors is being widely carried out starting with CuAlO₂ by Kawazoe et al. to perovskites [2–4]. Their successful implementation might help achieve many technological advancements, e.g. in bifacial and multijunction solar cells and water-splitting devices that require both p- and n-type transparent electrodes [2,5,6]. However, none of the efforts for p-type electrodes

have been near to successful in terms of transparency, conductivity and hole mobility. Thus, carbon nanotube networks especially based on single-walled carbon nanotubes (SWCNTs) [7–9], conductive polymer films like PEDOT:PSS [10–12], and transition metal oxides [13–20] have recently emerged as alternative promising p-type transparent conductors owing to superior optical and electrical characteristics.

The unique optoelectronic properties of SWCNTs are attracting extensive research efforts from the scientific community in different fields [7]. Over the last decade, enormous interest was devoted to the development of SWCNTs as transparent conductive film in versatile applications e.g. photovoltaics, optoelectronic, and photodetection [7, 21–29]. SWCNTs have recently achieved sheet resistance values below 100 Ω/sq with a transmittance of 90% in the middle of visible spectrum (550 nm) [30–32], which make randomly oriented p-doped SWCNT

* Corresponding author.

** Corresponding author. Skolkovo Institute of Science and Technology, Skolkovo Innovation Center, Building 3, Moscow, 143026, Russia.

*** Corresponding author. Skolkovo Institute of Science and Technology, Skolkovo Innovation Center, Building 3, Moscow, 143026, Russia.

E-mail addresses: pramod.rajanna@skolkovotech.ru (P.M. Rajanna), peter.lund@aalto.fi (P.D. Lund), a.nasibulin@skoltech.ru (A.G. Nasibulin).

films a promising alternative to replace widespread transparent conducting oxides. However, the SWCNT electrical conductivity, which is already close to the fundamental limit in a single-element configuration [30], is still a bottleneck for real applications [3,17,27]. The integration of a wire network as efficient transparent and conductive electrode places a prominent challenge in terms of obtaining sufficiently long, thin nanotubes with smooth surfaces as well as realization of firm contact at the heterointerface with other semiconductor materials [1,22,33]. To this end, poly (3,4-ethylenedioxythiophene) polystyrene sulfonate (PEDOT:PSS) has emerged as a cost-effective and industrial compatible conductive polymer that has showed high integration performance with SWCNTs owing to its high conductivity, transparency, and mobility [34–36]. Moreover, the use of transition metal oxide as carrier selective contact has induced a great deal of interest in recent years [14–17,19,37]. Interestingly, molybdenum oxide (MoO_3) which acts as a metal with high workfunction is considered to be a preferential multi-dimensional material with great asset as efficient hole transport layer, carrier dopant to SWCNTs and PEDOT:PSS and importantly also as an antireflection layer in various photovoltaics technologies [14–19,37–39]. Further development of p-type transparent conductors based on SWCNTs requires not only effective and stable dopant molecules, but also a rational design. To this end we introduce the concept of a multilayered unified combination of films with conductive polymers and transition metal oxides.

In this study, we present a novel approach of constructing a multi-component composite that combines SWCNT films and fibers, PEDOT:PSS and MoO_3 as components of an effective flexible and transparent p-type conductor in the configuration of SWCNTs- MoO_3 -PEDOT:PSS/SWCNT fibers measuring a record equivalent sheet resistance (R_{sh}) of $17 \Omega/\text{sq}$ with a transmittance of 90% at 550 nm. The developed TCF displays a high degree of mechanical flexibility with $\leq 5\%$ change in resistance. Such configuration allows the creation of both an effective window layer and charge transport medium in high-performance solid-state hybrid solar cells. We demonstrate the effectiveness of developed TCF by integrating on a-Si:H absorber yielding an outstanding short-circuit current density (J_{sc}) of $15.03 \text{ mA}/\text{cm}^2$ and record PCE up to 8.8% for SWCNTs/a-Si:H hybrid structures. This is an effective 16% improvement over a conventional n-i-p configured solar cell. Based on a set of characterization techniques and numerical simulation, we reveal the optoelectronic properties governing the device performance and explain the related fundamental mechanism of our developed multi-functional layers as p-type TCF. The outstanding performance of the as fabricated SWCNT/a-Si:H hybrid solar cell using TCF verifies its validity and broadens the horizon for the application of our novel p-type electrode in varied and versatile new energy technologies.

2. Methods

2.1. TCF and solar cell fabrication

2.1.1. Materials

The SWCNT films were synthesized by means of aerosol chemical vapor deposition (CVD) method as described in details elsewhere [9,40,41]. The synthesized material was confirmed to be single walled carbon nanotubes by transmission electron microscopy (TEM) as shown in the Supplementary Information Fig. S1. The doping of SWCNT films was performed using spin-casting of a 15 mM chloroauric acid (HAuCl_4) solution in ethanol [31]. Thin MoO_3 interlayers of about 4 nm were deposited using thermal evaporation technique in vacuum at room temperature. Furthermore, SWCNTs-PEDOT:PSS composite was formed by spin-casting of an electrically conductive PEDOT:PSS on SWCNT films from the pre-mix of commercially available 5 ml PEDOT:PSS (1.3 wt%) aqueous suspension with 120 μl of glycerin, 250 μl of N-methylpyrrolidone and 6.25 ml of isopropyl alcohol (IPA) [36]. 4 wt% polymethylmethacrylate (PMMA) solution in anisole was spin-casted on SWCNT fibers to form the anti-reflective layer [36].

2.1.2. SWCNT fibers

To utilize the exceptional electrical properties of SWCNTs, the original films were transformed to form self-similar top fiber electrodes. SWCNT films were dry-transferred onto a cleaned glass surface. A drop of isopropanol (IPA) was drop-casted on the SWCNT films. The wet film was carefully lifted to make long and narrow SWCNT fibers [42]. Solvent evaporation shrinks the film into a dense fiber (fabrication process is shown in Fig. 1a–d) with a width of 60–100 μm after being placed on top of SWCNTs- MoO_3 -PEDOT:PSS composite film in a wet-state as shown in Fig. 1e and f. SWCNTs utilized for fibers and films were synthesized at the same conditions. Then the wet fiber was placed onto the composite surface and dried to make a conformal contact to the underlying SWCNTs- MoO_3 -PEDOT:PSS composite film as seen from Fig. 1e and f. This flattened shape builds a strong van der Waals interaction between the SWCNT fibers and the composite film, induced by their self-similar structure, thereby completing the TCF.

2.1.3. Solar cell fabrication

For the solar cell fabrication, we used $10 \times 10 \text{ cm}^2$ commercial glass substrates coated with 700 nm textured aluminum doped zinc oxide (AZO) as back contact. Both n-doped a-Si:H layer and intrinsic i-a-Si:H absorber were grown consequently over AZO layer in a multichamber plasma enhanced CVD system von Ardenne CS-400PS at 13.56 MHz [43,44]. After that the substrate was cut into $2.5 \times 2.5 \text{ cm}^2$ individual samples for device fabrication. SWCNTs film and fiber top electrodes on a-Si:H (i) define the working area (1 cm^2) of individual cells. The reference sample was fabricated with conventional 10 nm p-a-Si window layer and 90 nm indium tin oxide (ITO) front electrode. The SWCNTs/a-Si:H hybrid solar cells were fabricated as described in detail previously [36]. In brief, partially fabricated a-Si:H thin film solar cells till intrinsic layer were utilized. Ultra-thin MoO_3 (4 nm) was thermally evaporated on a-Si:H (i). Different configurations of developed TCFs (TCF1, TCF2, TCF3 and TCF4) were deposited on MoO_3 under ambient conditions as p-type window layer and front electrode to complete the device architecture as shown in Fig. 1. Cross-section scanning electron microscopy (SEM) image of the fabricated device is shown in Supplementary Fig. S2.

2.2. TCF and solar cell characterization

High resolution scanning electron microscope (HR-SEM Zeiss Merlin) was used for surface morphology, thickness and cross-section of TCFs, solar cells and SWCNT fibers. Optical measurements were carried on Bentham PVE300 in the visible range from 300 to 800 nm [36]. The sheet resistance (R_s) of the samples was measured by a linear four-probe method (with a distance of 1 mm between the probes) using Jandel RM3000 test unit which served as a current source and digital voltmeter. For a qualitative comparison of TCF characteristics with different transmittances, we utilized an equivalent sheet resistance (R_{90}) calculated for a transmittance of 90% at 550 nm (T_{550}) with $R_{90} = 1/(K \cdot \log_{10}(10/9))$, where $K = 1/(R_s \cdot A_{550}) = \log_{10}(T_{550})/R_s$ is a figure of merit of TCF. Conductivity, σ , was calculated from $\sigma = R_s/t$, where t is the thickness [40].

The solar cells were characterized by J - V measurements under standard test conditions (100 mW/cm^2 , 25 °C) using an AAA Class solar simulator with an AM1.5G filter [36]. Furthermore, spectral response measurements, external quantum efficiency (EQE), of the single junction solar cells were conducted using a monochromator in the wavelength range between 300 and 800 nm [36].

2.3. Numerical simulations

In order to elucidate the physical mechanism of different TCF configurations and to gain fundamental understanding of their integration in n-i-p solar cells, we performed numerical simulations using AFORS-HET (automat for simulation of heterostructures) software [45]. The

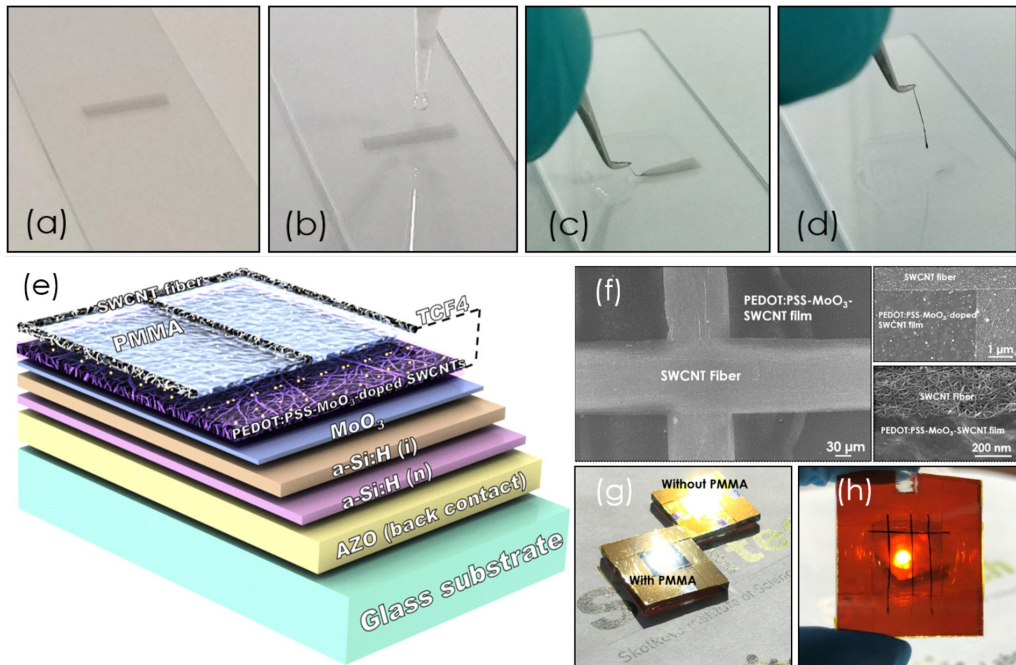


Fig. 1. SWCNT fiber fabrication process using wet-pulling technique: (a) Dry transferred SWCNT film on glass surface; (b) Drop-casting of isopropyl alcohol (IPA); (c) Self-shrinking of SWCNT film; (d) SWCNT fiber formation under the IPA evaporation; (e) Solar cell architecture with newly developed transparent electrode TCF4 (from bottom to top): Glass/Al:ZnO/a-Si:H (n)/a-Si:H (i)/MoO₃/SWCNT doped-MoO₃-PEDOT:PSS/SWCNT fibers doped/PMMA; (f) SEM images of SWCNT fibers showing a cross point of two fibers on a cell surface, the PEDOT:PSS-MoO₃-doped SWCNTs composite film and good contact between the composite film and fiber crossed on the cell surface uniformly; (g) Fabricated solar cells (with and without PMMA) exposed to sun showing the anti-reflective effect with PMMA coating; and (h) Photograph of the fabricated solar cell on a-Si using developed TCF showing its transparency.

simulation program includes various possibilities of modelling hetero-junction solar cells and standard methods for determining characteristics. The general principles of modelling solar cells are based on solving semiconductor equations as in Poisson's, transport and continuity equations for charge carriers [46].

The adopted electrical parameter set is presented in [Supplementary Table S1](#) based on our previous characteristics [36] and relevant references [31,47–51]. The optical refractive index and extinction coefficient data were implemented on the basis of ellipsometry measurements [52]. Moreover, the optical properties, mainly external and internal reflections on the front and rear electrode, were taken in account according to the cell configuration. The band diagram was plotted in the equilibrium calculation mode. The $J-V$ curves were extracted at steady-state DC mode under spectral radiation AM1.5 at ambient temperature. The spectral response was computed using a monochromatic excitation photon flux of $10^{16} \text{ cm}^{-2} \text{ s}^{-1}$ in the wavelength range between 300 and 800 nm.

3. Results

3.1. Opto-electrical and mechanical properties of TCF components

3.1.1. Opto-electrical properties of SWCNT films, SWCNT fibers and TCF

All the ingredients utilized to compose the p-type multilayer TCFs are listed in [Table 1](#). SWCNT films were created using a dry-transfer technique [40], SWCNT fibers were wet pulled from the film as described above. For doping of the SWCNT films and fibers, we used a HAuCl₄ ethanol solution. PEDOT:PSS layer was deposited onto SWCNT by spin-casting technique. MoO₃ was deposited by thermal evaporation method. The layer of PMMA was spin casted on the surface of SWCNTs

fibers.

The surface morphologies of the pristine SWCNT, MoO₃-SWCNT, SWCNTs-MoO₃-PEDOT:PSS and SWCNTs doped -MoO₃-PEDOT:PSS films are shown in [Fig. 2a–d](#). When deposited onto porous SWCNTs, PEDOT:PSS impregnates the film, which leads to the formation of a homogeneous composite material with a smooth surface. Each successive component added to the composite affected both optical and electrical properties as shown in [Table 1](#). The original SWCNT films we used had a transmittance of 87% at 550 nm ([Fig. 2e](#)), whereas that of the fiber shrunk from the same SWCNT film was much lower (~2.0%). The reason for the difference is that during the process of being picked up and layed down, the film condensed into a narrow dense fiber with overlapped nanotube bundles and most of the incident light would be depleted ([Fig. 2](#)). Also, for comparison, the optical transmission of polymethylmethacrylate (PMMA), doped SWCNT film and fiber, SWCNT-MoO₃ and different TCFs (TCF1, TCF2, TCF3 and TCF4 as in [Table 1](#)) are shown in [Fig. 2](#). The conductivity (σ in S cm^{-1}) of the SWCNT film and SWCNT fiber was $0.15 \pm 0.02 \text{ S cm}^{-1}$ and $62.00 \pm 7.20 \text{ S cm}^{-1}$ respectively, demonstrating the excellent conductivity of the SWCNT fiber. While the doped SWCNT films and SWCNT fibers showed a substantial increase in the conductivity to $0.51 \pm 0.06 \text{ S cm}^{-1}$ and $100.00 \pm 11.60 \text{ S cm}^{-1}$, respectively. The equivalent sheet resistance (at a transmittance of 90%) [53] of pristine SWCNT film was $364 \text{ } \Omega/\text{sq}$. Doping of the SWCNT film by HAuCl₄ reduced the transmittance value by 2.6%, but also decreased the equivalent sheet resistance to $104 \text{ } \Omega/\text{sq}$. Similarly, spin casting of PEDOT:PSS on top of the SWCNTs led to a decrease of both transmittance and sheet resistance of the resulted film. A composite structure containing doped SWCNTs, MoO₃ and PEDOT:PSS revealed a transmittance of 81.2% with an equivalent sheet resistance of $65 \text{ } \Omega/\text{sq}$. The enhancement of the optoelectrical properties was

Table 1

Description and comparison of transmittance (%), conductivity, σ ($S\text{ cm}^{-1}$), sheet resistance R_s (Ω/sq) and equivalent sheet resistance R_{90} (Ω/sq) of pristine SWCNT film, doped SWCNT film, SWCNT-MoO₃, SWCNT-PEDOT:PSS, SWCNT-MoO₃-PEDOT:PSS, SWCNT doped-MoO₃-PEDOT:PSS, SWCNT fiber, doped SWCNT fiber, TCF1, TCF2, TCF3 and TCF4.

Sample Name	Structure description	T (%)	σ ($S\text{ cm}^{-1}$)	R_{sh} (Ω/sq)	R_{90} (Ω/sq)
SWCNT film	Thin film of SWCNTs	86.6	0.15 ± 0.02	128 ± 5.0	364
Doped SWCNT film	Spin-casting of HAuCl ₄ on SWCNT film.	84.0	0.51 ± 0.06	37 ± 2.0	104
SWCNT-MoO ₃	Thermal evaporation of MoO ₃ on SWCNT film.	86.2	0.21 ± 0.02	112 ± 3.0	312
SWCNT-PEDOT:PSS	Spin-casting of PEDOT:PSS	84.6	0.59 ± 0.07	76 ± 3.5	205
SWCNT-MoO ₃ -PEDOT:PSS	Composite structure	83.8	1.00 ± 0.11	49 ± 2.2	123
SWCNT doped-MoO ₃ -PEDOT:PSS	CNT doped composite structure	81.2	1.82 ± 0.20	27 ± 1.1	65
SWCNT fiber	Narrow fibers from SWCNT film	2.0	62.00 ± 7.20	–	–
Doped SWCNT fiber	Fibers doped with HAuCl ₄	1.9	100.0 ± 11.6	–	–
TCF1	SWCNTs-PEDOT:PSS/SWCNT fibers	78.9	12.42 ± 1.37	12.0 ± 0.8	28
TCF2	SWCNTs-MoO ₃ -PEDOT:PSS/SWCNT fibers	78.7	14.90 ± 1.64	10.0 ± 0.4	22
TCF3	SWCNTs doped with HAuCl ₄ -MoO ₃ -PEDOT:PSS/SWCNT fibers doped with HAuCl ₄	76.3	24.83 ± 2.73	6.0 ± 0.3	17
TCF4	SWCNTs doped with HAuCl ₄ -MoO ₃ -PEDOT:PSS/SWCNT fibers doped/PMMA	76.3	24.83 ± 2.73	6.0 ± 0.3	17

observed after SWCNT fibers were added on top of the composite (in a 3 bus bar (3BB) configuration with a distance between parallel fibers of 3 mm as shown in Figs. 1 and 2f), lowering the equivalent sheet resistance to 28 Ω/sq for the non-doped stack SWCNTs-PEDOT:PSS/SWCNT fibers (TCF1). This highlights that SWCNT fibers can also be substituted for traditional metal contacts owing to its high conductivity and simple deposition process as demonstrated here. The deposition of MoO₃ on the SWCNT surface (TCF2) before adding PEDOT:PSS dropped the value to 22 Ω/sq . A record equivalent sheet resistance of 17 Ω/sq was achieved for a complete structure consisting of HAuCl₄ doped SWCNTs with MoO₃ and PEDOT:PSS covered by doped SWCNT fibers (TCF3). To the best of our knowledge, this is the state-of-the-art equivalent sheet resistance for a transparent electrode based on randomly oriented SWCNT films and for any transparent p-type conductors [3].

3.1.2. Mechanical properties of TCF

The developed transparent p-type conductor showed a high degree of mechanical flexibility. The TCF3 on a polyimide (PI) substrate was subjected to 50 000 bending cycles (at bending angles of 20°, 45°, 90° and 180°, which corresponded to radii of curvature of 10, 6.5, 4.5 and 1.6 mm⁻¹). The resistance of the electrodes increased to 0.65–5.15%,

respectively, and became stable after 23 000–40 000 cycles as shown in Fig. 2g and Supplementary Fig. S3.

3.2. Application of developed TCF in hybrid solar cell

To prove the applicability of the developed TCFs, we tested the material as a p-type window layer and a front electrode in hybrid solar cells based on amorphous silicon (the fabricated device picture and the schematics are shown in Fig. 1a–d). Recently, we have reported hybrid solar cells using SWCNT film and a-Si:H [35,36], revealing that the intrinsic absorber layer of the solar cells had a poor contact with SWCNTs deposited on top, which could be improved by impregnating the tubes with conductive polymer [35,36]. Furthermore, for better extraction of charge carriers and alignment of bands in the solar cell layers, we added a supplemental ultra-thin MoO₃ layer on the a-Si:H(i) surface as both passivation buffer layer and high work function hole selective contact. Experimental and numerical simulation (Supplementary Table S1) of the *J-V* characteristics of four different cell types under AM 1.5 conditions are shown in Figs. 3 and S4 (*J-V* parameters tabulated in Supplementary Table S2). Typical photovoltaic behavior was observed for all types with good correlation between experiment and simulation. The TCF1 solar cell *J-V* curve exhibited S-shape behavior with improved short-circuit current density of $J_{sc} = 11.93\text{ mA cm}^{-2}$ compared to solar cell without MoO₃ (Supplementary Fig. S5a), open-circuit voltage of $V_{oc} = 0.795\text{ V}$, and fill factor of $FF = 41.3\%$, resulting in $PCE = 3.9\%$. This highlights that the ultra-thin MoO₃ layer with a high work-function compared to the valence band energy of the a-Si:H absorber (5.6 eV) [47] reduces the barrier between TCF1 and a-Si:H and induces band bending of TCF1 thereby increasing the hole density in the vicinity of the TCF1/MoO₃/a-Si layer (Fig. 4a). The resulting asymmetry between the hole and electron conductivity [17] in TCF/MoO₃/a-Si increases the extraction of holes from a-Si:H absorber.

Subsequently, the TCF2 configuration with MoO₃ on the SWCNT film exhibited $J_{sc} = 12.63\text{ mA cm}^{-2}$, $V_{oc} = 0.800\text{ V}$, and $FF = 51.1\%$ ($PCE = 5.1\%$) with no S-shape and elevated photo and dark currents (Supplementary Fig. S4) indicating lower junction and TCF2 resistance (Table 1 and Supplementary Table S3). Further, the difference in work functions between SWCNTs (4.5 eV) and MoO₃ (6.5 eV), leads to a large band bending implicated in the alignment of the Fermi level (Fig. 4b).

TCF3 cell showed an ideal *J-V* curve with $J_{sc} = 12.83\text{ mA cm}^{-2}$, improved $V_{oc} = 0.870\text{ V}$ and significantly increased $FF = 67.4\%$, resulting in $PCE = 7.5\%$. In the TCF3, doping of the SWCNT films and fibers increases the conductivity of the electrode owing to the reduced Schottky barrier between semiconducting and metallic SWCNTs [54] and increase in the hole concentration, which yields a significant improvement in the short-circuit current and a drop in series resistance (Supplementary Tables S2 and 3). Furthermore, the shift in the work function of the SWCNTs from 4.45 to 6.14 eV after the doping [31] changes the band alignment and promotes photo-carrier extraction to the highly conductive SWCNT fibers (Fig. 4c). The band alignment in the SWCNTs/MoO₃ dictates the conduction mechanism through band-to-band (B2BT) or trap-assisted (TAT) tunneling [48]. The low activation energy (the difference between Fermi level and the highest level of the valence band) of doped SWCNTs and high work function of MoO₃ enables the reduction of energy barriers for better collection of holes and inhibits the conduction of electrons [47,55]. Therefore, in TCF3 the band offset between the valence band of SWCNTs and the conduction band of MoO₃ is minimized leading to a promoted B2BT (Fig. 4c) resulting in lower resistive losses at the junction; while in TCF2 hole transport is characterized by a dominant TAT (Fig. 4b).

Finally, TCF4 devices demonstrated improved characteristics of $J_{sc} = 14.11\text{ mA cm}^{-2}$, $V_{oc} = 0.907\text{ V}$, and $FF = 68.0\%$, leading to a record $PCE = 8.3\%$ with a diode ideality factor $n = 1.02$ (Supplementary Table S3). The increase in the short-circuit current is mainly due to the anti-reflective effect of PMMA [36] leading to higher photo-generation current in the a-Si:H layer. Introducing a reflective rear mirror on the

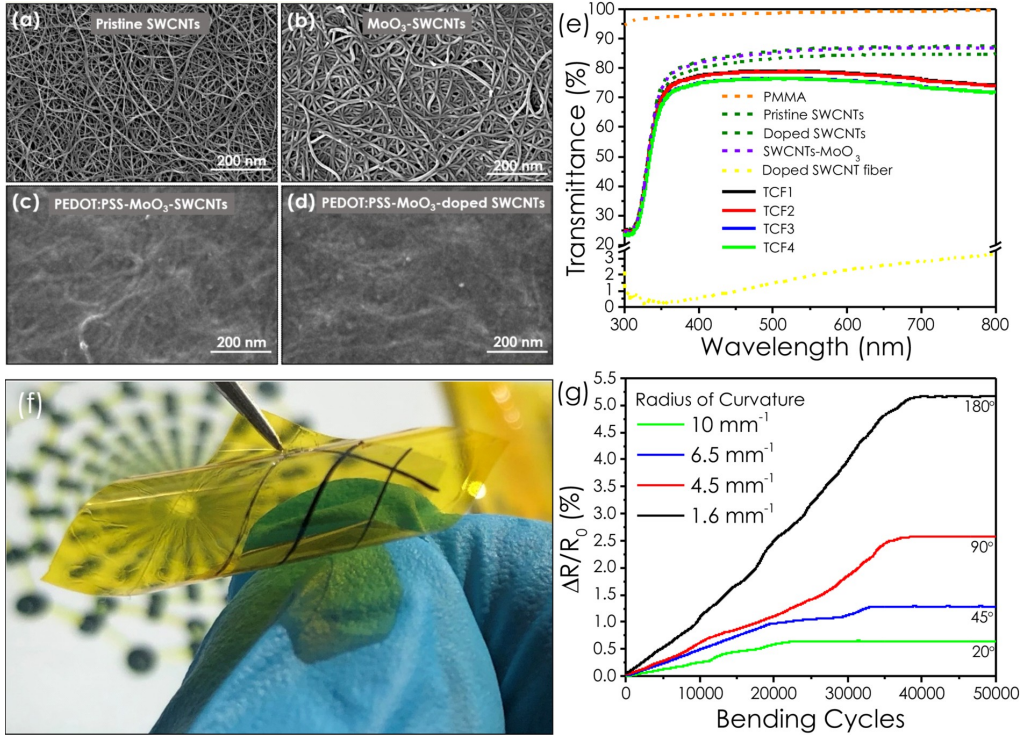


Fig. 2. Surface morphology of various types of electrodes: (a) Pristine SWCNTs; (b) MoO₃-SWCNTs; (c) PEDOT:PSS-MoO₃-SWCNTs composite; and (d) PEDOT:PSS-MoO₃-doped SWCNTs composite. (e) Optical transmittance of individual components for the TCFs: pristine and doped SWCNT films, SWCNT + MoO₃, PMMA, and different types of TCFs: TCF1, TCF2, TCF3 and TCF4. For comparison the transmittance spectra of SWCNT fiber and SWCNT fiber doped are also presented; (f) A photograph of TCF3 on a polyimide substrate; and (g) TCF4 resistance change during 50 000 bending cycles at angles of 20°, 45°, 90° and 180° with the radii of curvature from 10 to 1.6 in mm⁻¹.

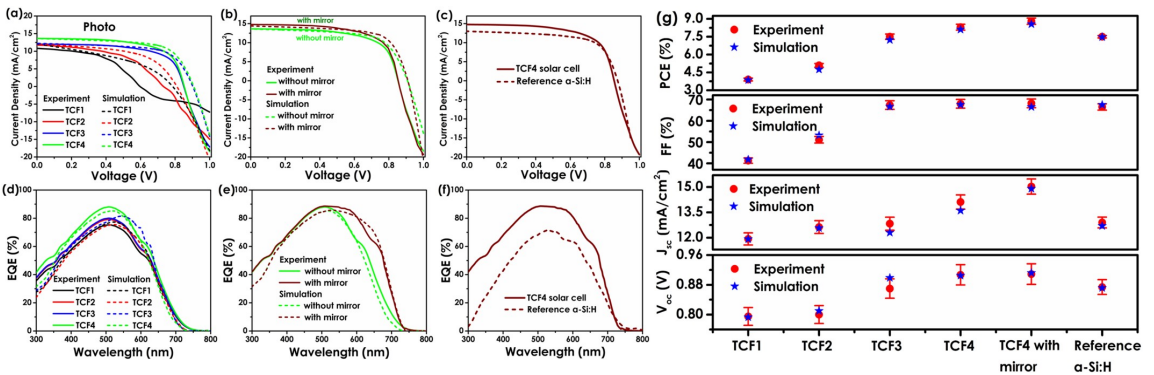


Fig. 3. Comparison of experimental data and simulations of (a) photo J-V curves; (b) photo J-V curves with and without mirror; (c) J-V curves of TCF4 solar cell and standard reference a-Si:H solar cell; (d) EQE spectra of respective TCF solar cells; (e) EQE spectra of without and with mirror (f) EQE spectra of TCF4 solar cell and standard reference a-Si:H solar cell; and (g) J-V parameters of fabricated solar cells using different TCFs.

back side of the TCF4 solar cell further increased the current density to $J_{sc} = 15.03 \text{ mA cm}^{-2}$ (Fig. 3b) and exceeded the state-of-the-art PCE = 8.8%, proving that internal reflection from the back reflector to the cell core further contributes into the increase in absorption by the a-Si:H layer. For comparison, the J-V curves of the latter device and the standard reference solar cell (with boron-doped a-Si:H p-type layer and

metal contacts) are shown in Fig. 3c. We see 16% (a net 1.4%) efficiency improvement after integrating the newly developed transparent electrode into the nip-configured a-Si:H solar cell instead of the conventional p-a-Si/TCO front window layer stack.

We measured the external quantum efficiency (EQE) of all solar cell types. Fig. 3d shows that the EQE value saturated at 75% for the TCF1

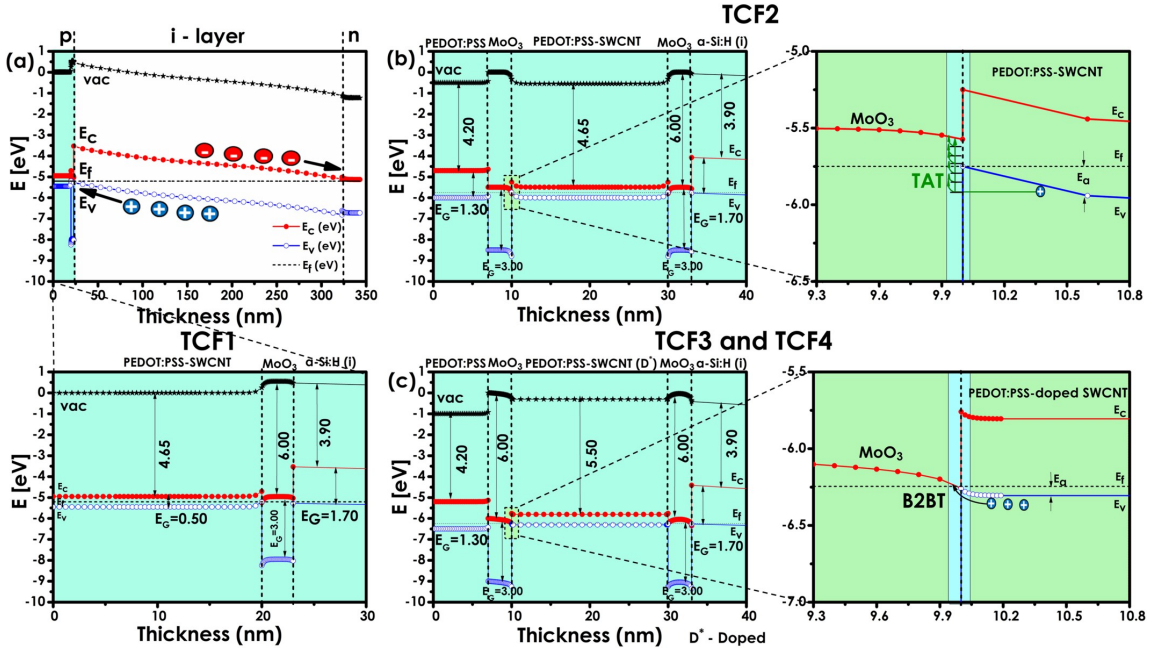


Fig. 4. Comparison of equilibrium band-diagrams of solar cells fabricated with (a) TCF1; (b) TCF2; (c) TCF3 and TCF4.

and nearly 80% for the TCF2 and TCF3 solar cells in the range from 300 to 800 nm, corresponding to the a-Si:H light absorption wavelength range. This results in an increase in the absolute EQE value by 30% compared to a solar cell without a MoO₃ layer (Supplementary Fig. S5b). Increased EQE indicates a reflection drop in the window layer [38], leading to enhanced photocurrent generation (Supplementary Table S4). Moreover, MoO₃ work function (6.5 eV) is higher than that of SWCNTs (4.45 eV), which might lead to additional p-type doping [56]. A drop in the series resistance from 10 Ω cm² (TCF1) to 6 and 3 Ω cm² (for TCF2 and TCF3, respectively) proves the rise of the hole concentration in the SWCNTs coated by MoO₃ (Supplementary Table S3 and Table 1). In contrast, the TCF4 solar cell with PMMA exhibited an increase in the EQE value saturated at around 90%, indicating a reduced reflection. Introducing a reflective rear mirror on the back side of a TCF4 solar cell results in broader EQE spectra for wavelengths over 500 nm as shown in Fig. 3e, clearly demonstrating increased absorption and better optical control in the a-Si:H layer. Also, for comparison the EQE spectra of a standard a-Si:H reference and TCF4 solar cells with reflective mirror is shown in Fig. 4f. The *J*_{sc} calculated from EQE spectra and *J*-*V* parameters for all the solar cell types are in very good agreement with the experiment as shown in Fig. 3g (Supplementary Tables S2 and S4), thus validating the performance of all solar cells with the developed transparent conductors [36].

4. Discussion and conclusions

Being used as a selective hole contact and window electrode the developed TCFs have a significant impact on the performance of solar cells. It has been demonstrated that the asymmetric conductivities of electrons and holes in their respective contact regions of the device are the key requirement for the charge carrier separation in solar cells [57, 58]. In our case, at the TCF contact, the charge hole current in the steady state is defined as follows

$$j_h = \frac{\sigma_h}{e} \text{grad } E_{F,v}$$

where σ_h is the electrical conductivity, e is the elementary charge and $E_{F,v}$ is the quasi Fermi level reflecting electrochemical potential of holes, and the occupation of states in the valence band [58]. In terms of physical perception, this electrochemical potential represents the free energy of hole carriers at a certain temperature. Thus, the preferential direction of hole transport tends to minimize their free energy [58]. The electrical conductivity depends on the hole mobility μ_h and carrier concentrations, n_h , as described in the equation $\sigma_h = en_h\mu_h$ [59]. Thus, a key guideline for better hole selectivity in our TCF is to ensure greater hole and low electron conductivities in the contact region.

In TCF1, the high work function of MoO₃ (6.5 eV) compared to the energy position of the valence band of the a-Si:H absorber (5.6 eV) [47] enables the Fermi energy of the TCF1 lower than the position of the valence band of a-Si:H. This induces an accumulation of holes and a depletion of electrons, ensuring a sufficient selectivity between charge carriers in the vicinity of the TCF1/MoO₃/a-Si layer [57] (Fig. 4a). The rise of local hole concentration promotes the asymmetry between the hole and electron conductivity in the contact region and boosts the selective extraction of excess holes from the a-Si:H absorber [57,59] (Table S3).

In TCF2, the difference in work functions between SWCNTs (4.5 eV) and MoO₃ (6.5 eV), leads to a large band bending implicated in the alignment of the Fermi level (Fig. 4b). The increase of EQE (Fig. 3d) for TCF 2 involving an additional MoO₃ compared to TCF1 is an indication of antireflection effect of MoO₃ in the window layer [38]. This minimization of light reflection loss leads to an enhancement of the generation of photocurrent.

In general, for a p-type contact, the transport of holes is governed by the energy barriers at the valence band [48]. Thus, in the case of TCF3, hole transport strongly depends on the activation energy of the SWCNT (difference between E_f and E_v) in respect to the work function of the MoO₃. By doping SWCNTs, the activation energy of SWCNTs is reduced which minimizes the energy barriers and allows better collection of holes.

Finally, it is envisaged that the future development of this novel p-

type TCF in combination with better passivation, light trapping schemes and nanostructuring [60] should revolutionize future photovoltaic devices. Nevertheless, the applications of the novel p-type composite material are not limited only to solar cells. Rational design and room-temperature processing broaden the horizon for transparent and flexible electrode implementation in diversified applications in other fields of science and technology.

In conclusion, we have developed a rational design for a novel highly efficient flexible transparent p-type conductor, combining the superior properties of SWCNTs with PEDOT:PSS, MoO₃ and SWCNT fibers grid into a single composite material. The use of thin multicomponent layers and the introduction of high-conductive SWCNT fibers have resulted in a major improvement in the TCF development. SWCNT fibers as such can be used as replacement for traditional metal contacts due to their high conductivity and simple deposition process as demonstrated here. A configuration of SWCNTs-MoO₃-PEDOT:PSS/SWCNT fibers resulted in a record equivalent sheet resistance of R₉₀ of 17 Ω/sq with a transmittance of 90%, and superior bendability. As a demonstration, the TCFs were used as a combined window layer and front electrode to form hybrid thin film solar cells with amorphous silicon absorber. An outstanding current of J_{sc} = 15.03 mA/cm² and a record PCE = 8.8% for such thin film solar cells led to an effective 16% improvement over a conventional nip-configured a-Si:H solar cells.

Acknowledgement

P.M.R. and A.G.N. acknowledge the Russian Science Foundation for the support (synthesis and doping of SWCNTs) by project #17-19-01787. H.M., O.S. and M.V. acknowledge the partial financial support by the Federal Ministry of Education and Research of Germany (BMBF, ref. number 01DJ15030). S.B and M.D acknowledge the Estonian Ministry of Education and Research (IUT19-28), and the European Union through the European Regional Development Fund project TK141. P.M.R thanks for the partial financial support from Doctoral Studies Internationalization Program Dora Plus activity 2.2 financed by European Regional Development Fund and EDUFi Fellowship (# TM-19-11028) from Finnish National Agency for Education.

Appendix A. Supplementary data

Supplementary data to this article can be found online at <https://doi.org/10.1016/j.nanoen.2019.104183>.

References

- [1] K. Ellmer, Past achievements and future challenges in the development of optically transparent electrodes, *Nat. Photonics* (2012), <https://doi.org/10.1038/nphoton.2012.282>.
- [2] M. Morales-Masis, S. De Wolf, R. Woods-Robinson, J.W. Ager, C. Ballif, Transparent electrodes for efficient optoelectronics, *Adv. Electron. Mater.* (2017), <https://doi.org/10.1002/aeml.201600529>.
- [3] K.H.L. Zhang, K. Xi, M.G. Blamire, R.G. Egdell, P-type transparent conducting oxides, *J. Phys. Condens. Matter* (2016), <https://doi.org/10.1088/0953-8984/28/38/383002>.
- [4] H. Kawazoe, M. Yasukawa, H. Hyodo, M. Kurita, H. Yanagi, H. Hosono, P-type electrical conduction in transparent thin films of CuAlO₂, *Nature* (1997), <https://doi.org/10.1038/40087>.
- [5] J.F. Wager, D.A. Keszler, R.E. Presley, Transparent electronics, 2008, <https://doi.org/10.1007/978-0-387-72342-6>.
- [6] L. Chen, J. Yang, S. Klaus, L.J. Lee, R. Woods-Robinson, J. Ma, Y. Lum, J.K. Cooper, F.M. Toma, L.W. Wang, I.D. Sharp, A.T. Bell, J.W. Ager, P-type transparent conducting oxide/n-type semiconductor heterojunctions for efficient and stable solar water oxidation, *J. Am. Chem. Soc.* (2015), <https://doi.org/10.1021/jacs.5b03536>.
- [7] P. Avouris, M. Freitag, V. Perebeinos, Carbon-nanotube photonics and optoelectronics, *Nat. Photonics* (2008), <https://doi.org/10.1038/nphoton.2008.94>.
- [8] E.M. Doherty, S. De, P.E. Lyons, A. Shmeliov, P.N. Nirmalraj, V. Scardaci, J. Joimel, W.J. Blau, J.J. Boland, J.N. Coleman, The spatial uniformity and electromechanical stability of transparent, conductive films of single walled nanotubes, *Carbon N. Y.* (2009), <https://doi.org/10.1016/j.carbon.2009.04.040>.
- [9] A.G. Nasibulin, A. Kaskela, K. Mustonen, A.S. Anisimov, V. Ruiz, S. Kivistö, S. Rackauskas, M.Y. Timmermans, M. Pudas, B. Aitchison, M. Kauppinen, D. P. Brown, O.G. Okhotnikov, E.I. Kauppinen, Multifunctional free-standing single-walled carbon nanotube films, *ACS Nano* (2011), <https://doi.org/10.1021/nn200338r>.
- [10] Y.H. Kim, C. Sachse, M.L. MacHala, C. May, L. Müller-Meskamp, K. Leo, Highly conductive PEDOT:PSS electrode with optimized solvent and thermal post-treatment for ITO-free organic solar cells, *Adv. Funct. Mater.* (2011), <https://doi.org/10.1002/adfm.201002290>.
- [11] S. Jäckle, M. Liebhaber, C. Gersmann, M. Mews, K. Jäger, S. Christiansen, K. Lips, Potential of PEDOT:PSS as a hole selective front contact for silicon heterojunction solar cells, *Sci. Rep.* 7 (2017) 1–8, <https://doi.org/10.1038/s41598-017-01946-3>.
- [12] C.P. Lee, K.Y. Lai, C.A. Lin, C.T. Li, K.C. Ho, C.I. Wu, S.P. Lau, J.H. He, A paper-based electrode using a graphene dot/PEDOT:PSS composite for flexible solar cells, *Nano Energy* (2017), <https://doi.org/10.1016/j.nanoen.2017.04.044>.
- [13] X. Li, W.C.H. Choy, F. Xie, S. Zhang, J. Hou, Room-temperature solution-processed molybdenum oxide as a hole transport layer with Ag nanoparticles for highly efficient inverted organic solar cells, *J. Mater. Chem. A* 1 (2013) 6614–6621, <https://doi.org/10.1039/c3ta10531h>.
- [14] J. Bullock, A. Cuevas, T. Allen, C. Battaglia, Molybdenum oxide MoOx: a versatile hole contact for silicon solar cells, *Appl. Phys. Lett.* (2014), <https://doi.org/10.1063/1.4903467>.
- [15] C. Battaglia, X. Yin, M. Zheng, I.D. Sharp, T. Chen, S. McDonnell, A. Azcatl, C. Carraro, B. Ma, R. Maboudian, R.M. Wallace, A. Javey, Hole selective MoOx contact for silicon solar cells, *Nano Lett.* (2014), <https://doi.org/10.1021/nl404389u>.
- [16] L.G. Gerling, S. Mahato, A. Morales-Vilches, G. Masmitja, P. Ortega, C. Voz, R. Alcubilla, J. Puigdollers, Transition metal oxides as hole-selective contacts in silicon heterojunctions solar cells, *Sol. Energy Mater. Sol. Cells* (2016), <https://doi.org/10.1016/j.solmat.2015.08.028>.
- [17] J. Bullock, M. Hettick, J. Geissbühler, A.J. Ong, T.G. Allen, C.M. Sutter-Fella, T. Chen, H. Ota, S. De Wolf, E.W. Schaler, C. Ballif, A. Cuevas, A. Javey, Efficient silicon solar cells with dopant-free asymmetric heterocontacts, *Nat. Energy* (2016), <https://doi.org/10.1038/energy.2015.31>.
- [18] Y. Jiang, C. Li, H. Liu, R. Qin, H. Ma, Poly(3,4-ethylenedioxythiophene):poly(styrenesulfonate)(PEDOT:PSS)-molybdenum oxide composite films as hole conductors for efficient planar perovskite solar cells, *J. Mater. Chem. A* (2016), <https://doi.org/10.1039/c6ta03658a>.
- [19] F. Wang, S. Zhao, B. Liu, Y. Li, Q. Ren, R. Du, N. Wang, C. Wei, X. Chen, G. Wang, B. Yan, Y. Zhao, X. Zhang, Silicon solar cells with bifacial metal oxides carrier selective layers, *Nano Energy* (2017), <https://doi.org/10.1016/j.nanoen.2017.07.014>.
- [20] C. Liu, W. Li, J. Chen, J. Fan, Y. Mai, R.E.I. Schropp, Ultra-thin MoOx as cathode buffer layer for the improvement of all-inorganic CsPbBr₂ perovskite solar cells, *Nano Energy* (2017), <https://doi.org/10.1016/j.nanoen.2017.08.048>.
- [21] P. Avouris, Z. Chen, V. Perebeinos, Carbon-based electronics, *Nat. Nanotechnol.* (2007), <https://doi.org/10.1038/nnano.2007.300>.
- [22] D. Kozawa, K. Hiraoka, Y. Miyauchi, S. Mouri, K. Matsuda, Analysis of the photovoltaic properties of single-walled carbon nanotube/silicon heterojunction solar cells, *Appl. Phys. Express* 5 (2012) 1–4, <https://doi.org/10.1143/APEX.5.042304>.
- [23] D. Jariwala, V.K. Sangwan, L.J. Lauhon, T.J. Marks, M.C. Hersam, Carbon nanomaterials for electronics, optoelectronics, photovoltaics, and sensing, *Chem. Soc. Rev.* (2013), <https://doi.org/10.1039/c2cs35335k>.
- [24] Y. Liu, F. Wang, X. Wang, X. Wang, E. Flahaut, X. Liu, Y. Li, X. Wang, Y. Xu, Y. Shi, R. Zhang, Planar carbon nanotube-graphene hybrid films for high-performance broadband photodetectors, *Nat. Commun.* 6 (2015) 1–7, <https://doi.org/10.1038/ncomms9589>.
- [25] Z. Zhang, L. Wei, X. Qin, Y. Li, Carbon nanomaterials for photovoltaic process, *Nano Energy* (2015), <https://doi.org/10.1016/j.nanoen.2015.04.003>.
- [26] X.G. Hu, P.X. Hou, C. Liu, F. Zhang, G. Liu, H.M. Cheng, Small-bundle single-walled carbon nanotubes for high-efficiency silicon heterojunction solar cells, *Nano Energy* (2018), <https://doi.org/10.1016/j.nanoen.2018.06.004>.
- [27] I. Jeon, Y. Matsuo, S. Maruyama, Single-walled carbon nanotubes in solar cells, *top. Curr. Chem.* (2018), <https://doi.org/10.1007/s41061-017-0181-0>.
- [28] I. Jeon, R. Xiang, A. Shawky, Y. Matsuo, S. Maruyama, Single-walled carbon nanotubes in emerging solar cells: synthesis and electrode applications, *Adv. Energy Mater.* (2018), <https://doi.org/10.1002/aeml.201801312>.
- [29] V. Ferguson, S.R.P. Silva, W. Zhang, Carbon materials in perovskite solar cells: prospects and future challenges, *Energy Environ. Mater.* (2019), <https://doi.org/10.1002/eeem.2.12035>.
- [30] K. Mustonen, P. Laiho, A. Kaskela, T. Susi, A.G. Nasibulin, E.I. Kauppinen, Uncovering the ultimate performance of single-walled carbon nanotube films as transparent conductors, *Appl. Phys. Lett.* (2015), <https://doi.org/10.1063/1.4932942>.
- [31] A.P. Tsapenko, A.E. Goldt, E. Shulga, Z.I. Popov, K.I. Maslakov, A.S. Anisimov, P. B. Sorokin, A.G. Nasibulin, Highly conductive and transparent films of H₂OCl₄-doped single-walled carbon nanotubes for flexible applications, *Carbon N. Y.* (2018), <https://doi.org/10.1016/j.carbon.2018.01.016>.
- [32] E.X. Ding, Q. Zhang, N. Wei, A.T. Khan, E.I. Kauppinen, High-performance single-walled carbon nanotube transparent conducting film fabricated by using low feeding rate of ethanol solution, *R. Soc. Open Sci.* (2018), <https://doi.org/10.1098/rsos.180392>.
- [33] X. Li, M. Mariano, L. McMillon-Brown, J.S. Huang, M.Y. Sfeir, M.A. Reed, Y. Jung, A.D. Taylor, Charge transfer from carbon nanotubes to silicon in flexible carbon

- nanotube/silicon solar cells, *Small* (2017), <https://doi.org/10.1002/smll.201702387>.
- [34] Q. Fan, Q. Zhang, W. Zhou, X. Xia, F. Yang, N. Zhang, S. Xiao, K. Li, X. Gu, Z. Xiao, H. Chen, Y. Wang, H. Liu, W. Zhou, S. Xie, Q. Fan, Q. Zhang, W. Zhou, X. Xia, F. Yang, N. Zhang, S. Xiao, K. Li, X. Gu, Z. Xiao, H. Chen, Y. Wang, H. Liu, W. Zhou, S. Xie, Q. Fan, X. Xia, F. Yang, S. Xiao, X. Gu, Z. Xiao, H. Chen, Y. Wang, H. Liu, W. Zhou, S. Xie, Novel approach to enhance efficiency of hybrid silicon-based solar cells via synergistic effects of polymer and carbon nanotube composite film, *Nano Energy* (2017), <https://doi.org/10.1016/j.nanoen.2017.02.003>.
- [35] A.K. Alekseeva, P.M. Rajanna, A.S. Anisimov, O. Sergeev, S. Bereznev, A. G. Nasibulin, Synergistic effect of single-walled carbon nanotubes and PEDOT:PSS in thin film amorphous silicon hybrid solar cell, *Phys. Status Solidi* (2017), <https://doi.org/10.1002/psb.201700557>.
- [36] P.M. Rajanna, E.P. Gilshteyn, T. Yagafarov, A.K. Alekseeva, A.S. Anisimov, A. Neumüller, O. Sergeev, S. Bereznev, J. Maricheva, A.G. Nasibulin, Enhanced efficiency of hybrid amorphous silicon solar cells based on single-walled carbon nanotubes and polymer composite thin film, *Nanotechnology* 29 (2018), <https://doi.org/10.1088/1361-6528/aaa647>.
- [37] J.H. Yang, S.J. Kang, Y. Hong, K.S. Lim, Doping-free intrinsic amorphous silicon thin-film solar cell having a simple structure of $(\text{SiO}_2/\text{Si})_n/\text{Si}/(\text{SiO}_2/\text{Si})_m/\text{Si}$, *IEEE Electron. Device Lett.* 35 (2014) 96–98, <https://doi.org/10.1109/LED.2013.2289309>.
- [38] F. Wang, D. Kozawa, Y. Miyauchi, K. Hiraoka, S. Mouri, Y. Ohno, K. Matsuda, Considerably improved photovoltaic performance of carbon nanotube-based solar cells using metal oxide layers, *Nat. Commun.* (2015), <https://doi.org/10.1038/ncomms7305>.
- [39] L.K. Jagadamma, H. Hu, T. Kim, G.O.N. Ndjawa, A.E. Mansour, A. El Labban, J.C. D. Faria, R. Munir, D.H. Anjum, M.A. McLachlan, A. Amassian, Solution-processable MoOx nanocrystals enable highly efficient reflective and semitransparent polymer solar cells, *Nano Energy* 28 (2016) 277–287, <https://doi.org/10.1016/j.nanoen.2016.08.019>.
- [40] A. Kaskela, A.G. Nasibulin, M.Y. Timmermans, B. Aitchison, A. Papadimitratos, Y. Tian, Z. Zhu, H. Jiang, D.P. Brown, A. Zakhidov, E.I. Kauppinen, Aerosol-synthesized SWCNT networks with tunable conductivity and transparency by a dry transfer technique, *Nano Lett.* (2010), <https://doi.org/10.1021/nl101680s>.
- [41] Y. Tian, M.Y. Timmermans, S. Kivistö, A.G. Nasibulin, Z. Zhu, H. Jiang, O. G. Okhotnikov, E.I. Kauppinen, Tailoring the diameter of single-walled carbon nanotubes for optical applications, *Nano Res.* (2011), <https://doi.org/10.1007/s12274-011-0137-6>.
- [42] M.A. Zhilyaeva, E.V. Shulga, S.D. Shandakov, I.V. Sergeichev, E.P. Gilshteyn, A. S. Anisimov, A.G. Nasibulin, A novel straightforward wet pulling technique to fabricate carbon nanotube fibers, *Carbon* N. Y. (2019), <https://doi.org/10.1016/j.carbon.2019.04.111>.
- [43] A. Neumüller, S. Bereznev, M. Ewert, O. Volobujeva, O. Sergeev, J. Falta, M. Vehse, C. Agert, Carrier collection losses in interface passivated amorphous silicon thin-film solar cells, *Appl. Phys. Lett.* (2016), <https://doi.org/10.1063/1.4959955>.
- [44] A. Neumüller, O. Sergeev, S.J. Heise, S. Bereznev, O. Volobujeva, J.F.L. Salas, M. Vehse, C. Agert, Improved amorphous silicon passivation layer for heterojunction solar cells with post-deposition plasma treatment, *Nano Energy* (2018), <https://doi.org/10.1016/j.nanoen.2017.11.053>.
- [45] R. Varache, C. Leendertz, M.E. Gueunier-Farret, J. Haschke, D. Muñoz, L. Korte, Investigation of selective junctions using a newly developed tunnel current model for solar cell applications, *Sol. Energy Mater. Sol. Cells* (2015), <https://doi.org/10.1016/j.solmat.2015.05.014>.
- [46] G.J.H.M. Wilfried, van Sark, Lars Korte, Roca Francisco, Physics and Technology of Amorphous-Crystalline Heterostructure Silicon Solar Cells, Springer, 2010, <https://doi.org/10.1007/978-3-642-22275-7>.
- [47] C. Messmer, M. Bivour, J. Schon, S.W. Glunz, M. Hermle, Numerical simulation of silicon heterojunction solar cells featuring metal oxides as carrier-selective contacts, *IEEE J. Photovol.* (2018), <https://doi.org/10.1109/JPHOTOV.2018.2793762>.
- [48] A.V. Shah, Thin-film Silicon Solar Cells, 2010, <https://doi.org/10.1201/b16327>.
- [49] M.I. Kabir, Z. Ibrahim, K. Sopjan, N. Amin, Effect of structural variations in amorphous silicon based single and multi-junction solar cells from numerical analysis, *Sol. Energy Mater. Sol. Cells* 94 (2010) 1542–1545, <https://doi.org/10.1016/j.solmat.2009.12.031>.
- [50] N. Hernández-Como, A. Morales-Acevedo, Simulation of hetero-junction silicon solar cells with AMPS-1D, *Sol. Energy Mater. Sol. Cells* (2010), <https://doi.org/10.1016/j.solmat.2009.05.021>.
- [51] S. Balendhran, J. Deng, J.Z. Ou, S. Walia, J. Scott, J. Tang, K.L. Wang, M.R. Field, S. Russo, S. Zhuiykov, M.S. Strano, N. Medhekar, S. Sriram, M. Bhaskaran, K. Kalantar-Zadeh, Enhanced charge carrier mobility in two-dimensional high dielectric molybdenum oxide, *Adv. Mater.* (2013), <https://doi.org/10.1002/adma.201203346>.
- [52] G.E. Jellison, F.A. Modine, Parameterization of the optical functions of amorphous materials in the interband region, *Appl. Phys. Lett.* (1996), <https://doi.org/10.1063/1.118064>.
- [53] I.V. Anoshkin, A.G. Nasibulin, Y. Tian, B. Liu, H. Jiang, E.I. Kauppinen, Hybrid carbon source for single-walled carbon nanotube synthesis by aerosol CVD method, *Carbon* N. Y. (2014), <https://doi.org/10.1016/j.carbon.2014.06.057>.
- [54] K.K. Ki, J.B. Jung, K.P. Hyeon, M.K. Soo, H.Z. Geng, A.P. Kyung, H.J. Shin, S. M. Yoon, A. Benayad, J.Y. Choi, H.L. Young, Fermi level engineering of single-walled carbon nanotubes by AuCl₃ doping, *J. Am. Chem. Soc.* (2008), <https://doi.org/10.1021/ja8038689>.
- [55] P. Procel, G. Yang, O. Isabella, M. Zeman, Theoretical evaluation of contact stack for high efficiency IBC-SHJ solar cells, *Sol. Energy Mater. Sol. Cells* 186 (2018) 66–77, <https://doi.org/10.1016/j.solmat.2018.06.021>.
- [56] S.L. Hellstrom, M. Vosgueritchian, R.M. Stoltenberg, I. Irfan, M. Hammock, Y. B. Wang, C. Jia, X. Guo, Y. Gao, Z. Bao, Strong and stable doping of carbon nanotubes and graphene by MoO_x for transparent electrodes, *Nano Lett.* (2012), <https://doi.org/10.1021/nl301207e>.
- [57] P. Würfel, *Physics of Solar Cells: from Basic Principles to Advanced Concepts*, 2009.
- [58] U. Würfel, A. Cuevas, P. Würfel, Charge carrier separation in solar cells, *IEEE J. Photovol.* (2015), <https://doi.org/10.1109/JPHOTOV.2014.2363550>.
- [59] S.M. Sze, K.K. Ng, *Physics of Semiconductor Devices*, third ed., 2006, <https://doi.org/10.1002/9780470068328>.
- [60] C. Zhang, Y. Song, M. Wang, M. Yin, X. Zhu, L. Tian, H. Wang, X. Chen, Z. Fan, L. Lu, D. Li, Efficient and flexible thin film amorphous silicon solar cells on nanotextured polymer substrate using sol-gel based nanoimprinting method, *Adv. Funct. Mater.* 27 (2017), <https://doi.org/10.1002/adfm.201604720>.



Pramod M. Rajanna is a PhD student in Aalto University, Finland and Skolkovo Institute of Science and Technology, Russia. He previously worked as Researcher in EWE Research Center for Energy Technology NEXT ENERGY (Current, German Aerospace Center-DLR Institute of Networked Energy Systems) and Forschungszentrum Jülich, Germany. He received his Bachelor's and Master's in Electronics at University of Mysore, India in 2007 and 2009 respectively. His current research is focused on the application of SWCNT thin films as heterostructures for solar cell applications.



Dr. Sci. Albert G. Nasibulin is a Professor at Skolkovo Institute of Science and Technology (Moscow, Russia) and an Adjunct Professor at the Department of Applied Physics, Aalto University. He held an Academy Research Fellow position (term 2006–2011). He got his PhD in Physical Chemistry (1996) and Doctor of Science at Saint-Petersburg Technical State University (Russia). His main recent research topic is devoted to transparent, flexible, stretchable and conductive single-walled CNT films and their numerous applications in photonics, photovoltaics and optoelectronics. He has a successful background in an academic research with over 250 peer-reviewed scientific publications and 31 patents.



Dr. Peter D. Lund is a Professor in Engineering Physics and Advanced Energy Systems at Aalto University, Finland. He has 40 years of experience in new energy technologies, including solar and fuel cells. He has had visiting positions in China and Germany. Dr Lund is active in senior roles within European Union energy initiatives: he has chaired the Advisory Group Energy of European Commission and the Energy Steering Panel of European Academies Science Advisory Council. He has served in an advisory role for many energy programs worldwide. He is member of the Finnish Academy of Science and Letters and the Swedish Engineering Academy in Finland. He has published 500 research papers, and received several awards, including the Chinese Jinling Award in 2016.



Dr. Hosni Meddeb is a recipient of INTEL-KACST Consortium scholarship to conduct his doctoral research at IMEC in Belgium. In 2015, he received his Ph.D. degree in Physics, on the development of amorphous silicon thin films for Si heterojunction solar cells. For two years later, he joined the electrical engineering-nanoelectronics department at Interdisciplinary Institute for Technological Innovation (3IT) in Sherbrooke-Canada, developing tunnel field-effect transistors for CMOS technology. Since 2017, he is working as research scientist at German Aerospace Center, DLR Institute of Networked Energy Systems, involved in the photovoltaics activities and solar cells integration based on novel functional layers and nanostructured optoelectronic devices.



Dr. Oleg Sergeev owned his Ph.D. in Material Science in the field of light-emitting sol-gel nanostructures in 2001. His postdoctoral research at the University of Wuppertal, Germany was devoted to the development and application of unique near-field cathodoluminescence characterization technique. Since 2009 he develops solar cells at DLR Institute of Networked Energy Systems (former EWE Research Center for Energy Technology NEXT ENERGY) in Oldenburg.



Dr. Martin Vehse is head of the department Urban and Residential Technologies at the DLR Institute of Networked Energy Systems. He studied physics at the University of Bremen, finished his Ph.D. study with the doctoral level in 2001. Afterwards, he spent a post-doctoral period at the University of California, Santa Barbara at the Institute for Polymers and Organic Solids, working in the field of conducting polymers. In 2004, he started his professional career as project manager on OLED technology at the company Novald GmbH, and joined the photovoltaics activities at the research institute NEXT ENERGY in August 2010. Since 2017 he is working at the German Aerospace Center.



Dr. Sergei Bereznev received his Ph.D. degree in 2003 in chemical and material science from Tallinn University of Technology (TalTech). He worked as a researcher and senior researcher at the Department of Materials Science, TalTech from 2000 to 2016. He is currently an associate professor in the Department of Materials and Environmental Technology at TalTech. His current research interests include the development of novel functional layers and hybrid structures for optoelectronics, nanoscale coatings, and growth studies of nanostructures.



Dr. Olga Volobujeva is currently Senior Researcher in Department of Materials and Environmental Technology at the Tallinn University of Technology. She obtained her Ph.D. degree in Chemical and Material Science from TUT in 2008. Her research focuses on fabrication and characterization of chalcogenide-based thin film solar cells.



Alexey P. Tsapenko is currently a Ph.D. student at Skolkovo Institute of Science and Technology and Aalto University. He received his Bachelor and Master degrees in Optoelectronics from Bauman Moscow State Technical University in 2011 and 2013, respectively. His research focuses on the development of state-of-the-art flexible and stretchable material solutions for ITO replacement and diverse investigation of the carrier dynamics of the pristine and treated/doped SWCNTs.



Dr. Mati Danilov received his B.S. degree in applied physics from Tallinn University of Technology under the supervision of Prof. Jüri Krustok, in 2003. Then he obtained his M.S. degree in materials science also in Tallinn University of Technology, Estonia in 2005. During the master studies he worked as extraordinary researcher, later during Ph.D. studies as researcher in Department of Materials Science, Tallinn University of Technology. In 2016 he received his Ph.D. degree in materials science from the Tallinn University of Technology. His scientific interests are focused on solar energy material XPS studies and solar cell opto-electrical studies.

Publication 5

Pramod M. Rajanna*, Peter D. Lund*, Albert G. Nasibulin*. Hybrid heterojunction solar cells based on single-walled carbon nanotube and silicon thin films – a mini review. *Submitted, May 2020.*

© 2020 Pramod Mulbagal Rajanna.
Reprinted with permission

Hybrid heterojunction solar cells based on single-walled carbon nanotube and silicon thin films – a mini review

Pramod M. Rajanna^{1,2}, Peter D. Lund^{1*}, Albert G. Nasibulin^{1,2*}*

¹ Aalto University, School of Science, P.O. Box 15100, FI-00076 Aalto, Espoo, Finland

² Skolkovo Institute of Science and Technology, Nobel Street 3, Moscow 121205, Russia

*Corresponding authors:

Pramod M. Rajanna,

e-mail: rajanna.pramod@aalto.fi

Peter D. Lund,

e-mail: peter.lund@aalto.fi

Albert G. Nasibulin,

e-mail: a.nasibulin@skoltech.ru

Highlights

- First comprehensive review of SWCNTs/a-Si:H thin film solar cells is presented.
- Progress of SWCNTs/a-Si:H hybrid heterojunction solar cell from 0.03% to 8.80% is discussed.
- SWCNT composites as an effective p-type layer in hybrid heterojunction solar cell is discussed.
- Future development direction of SWCNTs based heterojunction solar cells is put forward.

Abstract

Hybrid heterojunction solar cells based on silicon and single-walled carbon nanotube (SWCNT) thin films have a simple structure and their manufacture employ simple low-temperature processes. Moreover, their progress has been rapid during the last decade, wherein the efficiency of heterojunction solar cells combining hydrogenated amorphous silicon (a-Si:H) and SWCNTs thin film has increased from 0.03% to 8.80%. Here, we present a comprehensive overview of the state-of-the-art on SWCNTs/a-Si:H heterojunction solar cells. In addition to a comprehensive technology review, important special features such as adhesion of SWCNT film to a-Si:H, the interface between SWCNT and a-Si:H, and their influence on the performance of the heterojunctions are included. Future paths for improving the performance of such solar cells are also suggested. Finally, key challenges and trends for further research and development of SWCNTs/amorphous silicon heterojunction solar cells are discussed.

Keywords

amorphous silicon, hybrid heterojunction, single-walled carbon nanotubes, solar cells, thin film

Nomenclatures used

AZO	Aluminum doped zinc oxide
a-Si:H	hydrogenated amorphous silicon
c-Si	crystalline silicon
CNTs	carbon nanotubes
CVD	chemical vapor deposition
FTO	fluorine doped tin oxide
FF	fill factor
ITO	indium tin oxide
J-V	current density-voltage
PV	photovoltaics
PCE	power conversion efficiency
PECVD	plasma-enhanced chemical vapor deposition
PDMS	polydimethylsiloxane
PEDOT:PSS	poly(3,4-ethylenedioxythiophene)-poly(styrenesulfonate)
PANI	polyaniline
PMMA	polymethylmethacrylate
SWCNT	single-walled carbon nanotube
TCF	transparent conductive film

1. Introduction

The interest in renewable energy sources has significantly increased along the needs to reduce greenhouse gas emissions as part of the climate change mitigation. Photovoltaics (PV) is one of the future key clean energy technologies and its markets are growing fast[1]. Among various solar cell types, crystalline silicon (c-Si) dominates the market showing high power conversion efficiency (PCE) exceeding 26% with heterojunction with intrinsic thin technology based on thin a-Si:H passivating layers and on interdigitated back contacts on n-type silicon wafers[2,3]. But as recent technologies are evolving into flexible, versatile and portable electronics, there is also demand for manufacturing solar cells in roll-to-roll processes while maintaining an adequate PCE. Such solar cells would be thin, flexible and could be directly incorporated into applications such as buildings, e.g. as roofing shingles. The structural complexity and ease of device fabrication are the key factors that determine the cost and the viability of future applications. Especially, thin film silicon and a group of nanomaterials and nanotechnologies are rising up as a promising trend due to the reduced usage of materials and adjustable structure at the nanoscale[4,5].

Thin film solar cells, including the ones made of hydrogenated amorphous silicon (a-Si:H), have been demonstrated as suitable materials for roll-to-roll production with advantages of reduced fabrication cost, increased light absorptivity, reduced thickness of solar cell, thereby reducing material consumption and device weight[4]. Additionally, a-Si:H can be deposited on any foreign substrate by plasma enhanced chemical vapor deposition (PECVD) close to room temperature[4]. But, as the carrier mobility of a-Si:H is low, they require an expensive transparent conducting layer as the top contact such as indium tin oxide (ITO)[6]. However, the ITO film causes not only optical loss due to parasitic absorption at a short wavelength but also open-circuit voltage (V_{oc}) degradation due to the plasma damage during sputtering[7–9]. Additionally, the ITO electrode have several other disadvantages including high cost, scarcity of material, lack of flexibility, high structural defects, and poor stability at high temperatures. Therefore, ITO-free solar cells have become an important focus of research for next generation PV devices[10,11].

Carbon is the other element (apart from silicon) that is abundantly available in nature, which have a historic contribution in research and human development. Moreover, carbon nanomaterials have become one of most active research fields in the world[12]. Among the various carbon nanomaterials, carbon nanotubes (CNTs), in particular SWCNTs, have made a

valuable contribution to recent advances in the field of solar cell development owing to a wide range of properties from conductors to semiconductors with variable bandgaps based on their atomic structure [13–18]. While the CNTs can have multiple number of walls, SWCNTs exhibit excellent opto-electrical advantages over double and multi-walled CNTs[19]. In PV devices, it has definite advantages in terms of flexibility, surface area, carrier mobility, chemical stability, and optoelectronic properties. A thin SWCNT film can be used not only as a perfect window layer in solar cells, but also as a transparent conductive electrode due to its direct sub-band gaps, tunable photoabsorption from the near infrared to the ultraviolet range, and high conductivity[16,20–22]. Moreover, SWCNTs have much higher mechanical resilience than ITO, with a similar work function of -5.0 eV and a much lower raw material cost owing to its abundance. For this reason, SWCNTs have been used extensively as a hole transport layer[16,23–28], even as light absorber[29–33], and more popularly as p-type transparent electrodes[25,34–40] in many solar cell devices and are termed as “heterojunction or hybrid solar cells”, thus replacing brittle ITO, fluorine-doped tin oxide and expensive metal electrodes, especially in c-Si[16,17,23,24,27,28,37,38], polymer[41–43], and more recently in perovskite based solar cells[16,17,44–48].

Among the different methods to grow SWCNTs, aerosol (floating catalyst) CVD method, which produces uniform thin films collected directly on a filter paper[49] is found to be one of the most promising and suitable for PV applications[17]. These SWCNT thin films have been combined with c-Si to form heterojunction solar cells that have rapidly progressed with PCE of 11-17% in the last decade[23,50,51]. Several reviews exist that highlights the progress made in SWCNT/c-Si solar cells[16,27,37,38,52–54]. Also, heterojunction solar cells combining a-Si:H and SWCNTs thin film have been reported that have progressed from around 0.03% to 8.80% during the same time[25,55–59]. The focus on using SWCNT thin films in a-Si:H is to prevent the use of any standard p-(boron or aluminum) doped a-Si:H or microcrystalline silicon, ITO and other traditional metal layers like Au, Ag, Al, and Cu. And, moreover to utilize the mechanical properties offered by both SWCNTs and a-Si:H, which are potential for flexible and wearable application. In this structure, SWCNTs are proposed as a window layer p-type transparent conductive film (TCF), a potential replacement for all the aforementioned layers and processes, thereby making less energy consuming process technology, minimizing the material consumption and reducing the net cost. Moreover, as recent technologies are evolving into flexible, versatile, and portable electronics, SWCNTs/a-Si:H heterojunction solar cells looks attractive. However, unlike SWCNTs/c-Si, no reports exists to highlight the progress made in SWCNTs/a-Si:H thin film heterojunction solar cells. Therefore, in this review, we

focus to present the application of SWCNT thin films in a-Si:H solar cells. We briefly discuss the working principles of SWCNTs/a-Si:H heterojunctions and summarize the development of SWCNT thin films in a-Si:H. The adhesion of SWCNT film to a-Si:H, the interface between SWCNT and a-Si:H, and their influence on the performance of the heterojunctions are discussed. This aims to highlight the progress and the advantages of SWCNT thin film as heterojunctions with a-Si:H in PV applications, and to provide possible hints that might help in the further development of SWCNTs-based PV devices.

2. SWCNTs/a-Si:H heterojunction solar cells

2.1 Working Mechanism

Solar cells composed of a SWCNT film and Si form a heterojunction device that has been well studied[39,60,61]. The SWCNT film acts not only as charge carrier transport, but also as a photoactive layer[37,52]. The SWCNTs/Si heterojunction follows classical p-n or Schottky theory, where in the photo-generated carriers travel distance is determined by the carrier diffusion length, which is of the same order of magnitude as the cell layer thickness. The electric field responsible for the separation of photo-generated carriers (electron-hole pairs) is concentrated within a very thin zone at the p/n junction or in other words at the closest proximity of the SWCNTs and Si interface, thereby enabling the separation of photo-generated carriers. However, in amorphous silicon materials, the carriers can travel only short distances before recombination. Hence, a uniform electric field needs to be present from the origin of photo-generation throughout the entire cell thickness. This electric field assists carrier travel and immediately separates electron and holes, thereby avoiding recombination. The field assisted travel distance is given by the drift length. Therefore, an intrinsic (i)-layer is inserted between p- and n-layers, to form a pin-diode. For more details on the pin-diode theory, the reader is suggested to review relevant literatures[6,62,63]. During the last decade, the use of carbon nanotubes in thin film amorphous silicon has been of great interest for researchers as light trapping structures, antireflective coatings, transparent electrodes, and p-type window layer contacting a-Si:H to form heterojunction[25,55–59,64–68]. Similar to SWCNTs/c-Si heterojunction[16,37,53], SWCNTs/a-Si:H also form semiconductor/semiconductor or metal/semiconductor junction as shown in Figure 1a and 1b. Here, the incident photons are mainly absorbed in i-layer thus generating electron-hole pairs at the close proximity of the p/i

interface. The carriers (electrons and holes) drift across a-Si:H (n) or n-type contact like ITO or AZO or metals like In/Ga[26], Ti/Au[69,70], or Al[71] that forms an ohmic contact with the amorphous silicon, and a-Si:H (p) or SWCNTs due to the built-in-voltage created by the applied electric field. Electrons are collected across n-type a-Si:H, ITO or AZO and holes are collected at p-type a-Si:H or SWCNTs itself that can be used as a p-type transparent electrode as shown in Figure 1. Further, the front electrode made of Ag[72], Au/Cr[73,74], or Pt[50] contacts the SWCNT film for better transfer of holes to an external circuit. Similar process happens when the metallic SWCNT-film comes in contact with i-layer thus forming Schottky junction as shown in Figure 1b. The differences will be the magnitude of the reverse saturation current and its switching characteristics.

The complexity of the SWCNT film, in which semiconducting and metallic nanotubes co-exist leads to the uncertainty at the interface between SWCNTs and a-Si:H. Several individual nanotubes are present in a device, and each forms a heterojunction with the i-layer of a-Si:H. As SWCNTs exhibit semiconducting and/or metallic behavior, a p-i-n junction can be respectively expected for the former (Figure 1a) and a Schottky junction for the latter (Figure 1b).

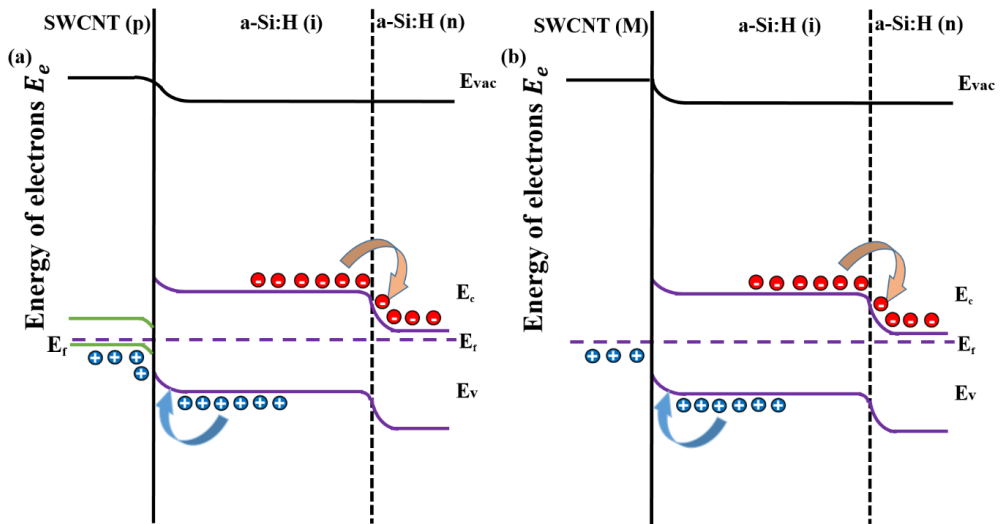


Figure 1. Illustration of (a) the SWCNTs film functioning as a p-type layer in semiconductor/semiconductor p-i-n junction; and (b) Schottky junction is formed by a metal/semiconductor interface.

2.2 SWCNTs as transparent electrodes

The first attempt to create a a-Si/CNT heterojunction was made by Schriver *et al.* using the carbon nanotube films as buckypaper and graphene in junctions with undoped a-Si thin films as shown in Figure 2a. The measured J-V characteristics of the buckypaper/a-Si heterojunction solar cell is as shown in Figure 2b[55]. The produced solar cells was air-stable without additional processing steps like doping, multilayer film deposition in high vacuum, or transparent conducting oxide deposition. In the subsequent year SWCNTs were sprayed on a-Si:H by Gobbo *et al.* to form Schottky barrier solar cells (Figure 2c) [56]. They measured the external quantum efficiency up to 35% at a wavelength of about 460 nm (Figure 2d) and indicated that for lower density SWCNT/a-Si:H heterojunction, nanotubes dominate the photocurrent generation, separation, and transport mechanism thereby splitting the electron-hole pair generation at the CNT-CNT or CNT-Si heterojunction. However, with increased density of SWCNT/a-Si:H heterojunction more electron-hole pairs are generated in a-Si:H. In the next year, Kim *et al.* used SWCNT films obtained by vacuum filtration through a mixed cellulose ester membrane as transparent electrodes on a a-Si:H n-i-p solar cell (Figure 3a)[64]. Despite their similar work functions, a Schottky barrier was formed at the SWCNTs/a-Si:H interface that resulted in an inoperable solar cell with a fill factor of 22% as shown in Figure 3b. In order to address this issue, gold nanodots were deposited at the p⁺ a-Si:H/SWCNTs interface (Figure 3a). The nanodots were found to be effective in eliminating the interfacial Schottky barrier thus allowing ohmic contact to form between the SWCNTs and p⁺ layer without any measurable impact on the J_{sc} . This approach led to achieving a respectable FF of 58% which is comparable to that of a a-Si:H p-i-n solar cell (FF of 62%) with conventional TCO (Figure 3c). In the same year, Khanal *et al.* used SWCNT films as electrodes to replace the p-layer and back contact in a-Si:H solar cell (Figure 3d)[75]. They varied the SWCNTs film thickness and inferred that the optical properties of the nanotubes affect the device performance than does the conductivity (Figure 3e). The cells were illuminated from each side (glass and SWCNTs), and a 25 nm thick SWCNTs film resulted in a PCE of 1.46% (Figure 3f). Funde *et al.* reported the first use of aerosol CVD synthesized SWCNT thin films as p-layer and transparent electrodes by a unique technique of dry-transfer in a-Si:H solar cells as in Figure 3g[57]. Further, the SWCNTs were doped with thionyl chloride (SOCl₂) that resulted in an improved PCE of 1.5% from 0.3% for pristine nanotubes (Figure 3h). They highlighted that there exists a substantial potential for further improvement as the parameters of the fabricated device were not optimized in terms of opto-electrical properties of SWCNTs,

thickness of nanotube films, and top metal contact. The studies on acid doping and SOCl_2 treatment of SWCNTs originated in SWCNTs/Si solar cells by Li *et al.*[76]. The doping shifts the Fermi level of SWCNTs below ν_1 , thus increasing the mobility and carrier density as in Figure 4a[16,77]. As a result, the S_{11} transition is suppressed in the semiconducting SWCNTs and further doping would suppress the S_{22} transition as well (Figure 4b), as observed by near-infrared absorption spectroscopy (Figure 4c).

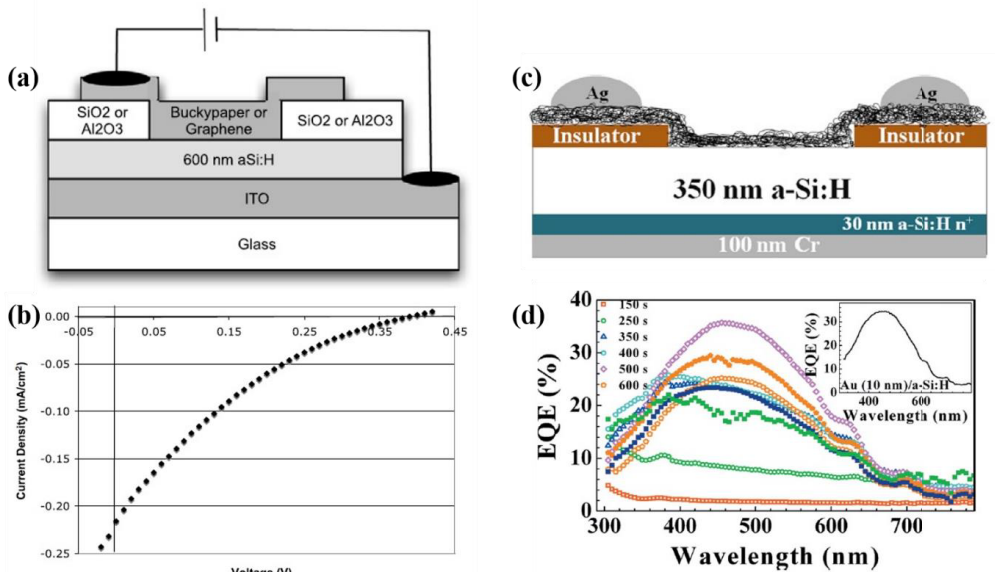


Figure 2. (a) A schematic of device structure. a-Si:H is PECVD deposited on patterned ITO substrates. Either SiO_2 or Al_2O_3 is deposited on top, and a window is patterned and etched. A carbon film is deposited over the window; (b) Illuminated J-V curves for buckypaper on a-Si:H cells[55]. Reproduced (adapted) with permission from (SOLID STATE COMMUNICATIONS 2010, 150, 561-563) with LICENSE NUMBER 4791270080232. Copyright (2010) Elsevier Ltd.; (c) A cross-sectional view of the device design of SWCNTs film as window layer on a-Si:H; and (d) EQE spectra of the SWCNT/a-Si:H device recorded as a function of the incident light wavelength for several SWCNT spraying times. In the inset the EQE spectrum of a 10 nm Au film covering the same a-Si:H device[56]. Reproduced (adapted) with permission from (APPLIED PHYSICS LETTERS 2011, 98, 183113) with LICENSE NUMBER 4791270287667. Copyright (2011) AMERICAN INSTITUTE OF PHYSICS.

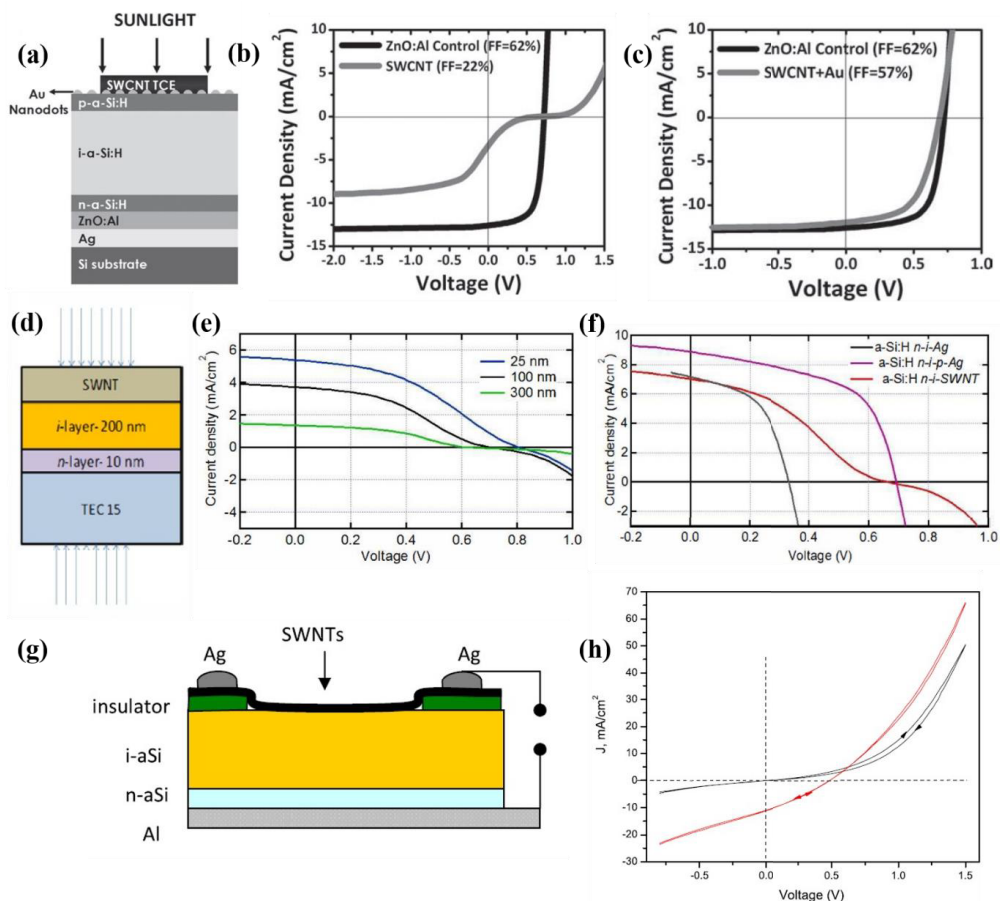


Figure 3. (a) The schematic of a-Si:H single junction solar cells with SWCNTs; (b) J-V curves of a-Si:H solar cells with SWCNTs without any interface treatment at the p + /SWCNT interface and a-Si:H solar cells with ZnO:Al without SWCNTs as a control sample; (c) J-V curves of a-Si:H solar cells with SWCNTs with gold nanodots at the p + /SWCNT interface and a-Si:H solar cells with ZnO:Al and without SWCNTs as a control sample[64]. Reproduced (adapted) with permission from (ADVANCED MATERIALS 2012, 24, 1899-1902) with LICENSE NUMBER 4791270600660. Copyright (2012) WILEY-VCH Verlag GmbH & Co. KGaA, Weinheim.; (d) Schematic of the aerosol CVD synthesized SWCNTs/a-Si:H device structure; and (e) J–V characteristics for forward and reverse scans at dark (black) and AM 1.5 illumination (red) for the HF-treated intrinsic a-Si:H and SOCl₂ doped SWCNTs film as p-type window layer[57]. Reprinted (adapted) with permission from (NANOTECHNOLOGY 27 (2016) 185401 (6PP)) with LICENSE ID 1023448-1. Copyright (2016) IOP Publishing Ltd.

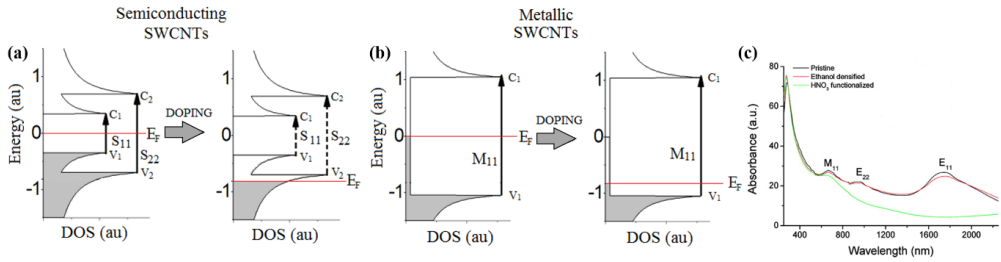


Figure 4. Density of states of pristine and doped (a) semiconducting; (b) metallic SWCNTs, respectively; and (c) absorbance spectra of pristine, ethanol densified, and HNO₃ functionalized SWCNTs film.

2.3 SWCNTs-PEDOT:PSS composite

Recently, it has been shown that both the environment and the substrate material influences the efficient usage of SWCNTs film[78,79]. The perpetual contact between the nanotubes film and the substrate material or the atmospheric medium impacts the interface properties that consequently effects net efficiency of the solar cell[71]. As an example, at the interface of SWCNTs/Si heterojunction solar cells there exists great profuse of nanotube-silicon junctions where SWCNTs are in physical contact with Si surface. However, within the SWCNT network many nanotubes overlap and suspend on each other without contacting the Si. As a result, the solar cell performance suffers due to the increased recombination at interface where bare Si surfaces are exposed to air[52,80]. To solve this problem, researchers have tried to mix conducting polymers with the SWCNT films to improve their junction density, uniformity, and conductivity[81,82]. Poly (3, 4-ethylenedioxythiophene):poly (styrenesulfonate) (PEDOT:PSS) is a well-researched and commonly used hole transport material, which has high conductivity, work-function, and transmittance[83]. Moreover, injecting PEDOT:PSS on SWCNTs film, the micro-pores are completely filled and surface roughness is decreased[24,59]. Researchers have therefore combined SWCNTs with PEDOT:PSS to further enhance the performance and form hybrid heterojunction PEDOT:PSS-SWCNTs/Si solar cells[84–89]. For example, Fan *et al.* developed an effective way of fabricating hybrid PEDOT:PSS/SWCNT/Si solar cells by placing a SWCNT network on the surface of a Si wafer and then spinning a PEDOT:PSS solution onto it[24].

In the subsequent year, our group reported the synergistic effect of SWCNTs and PEDOT:PSS as a composite p-type transparent electrode to be more effective in forming coupled continuous hybrid heterojunction with a-Si:H as shown in Figure 5a[58]. The

performance of the SWCNTs/a-Si:H, PEDOT:PSS/a-Si:H and SWCNTs-PEDOT:PSS/a-Si:H was compared (Figure 5b). It was found that SWCNTs-PEDOT:PSS composite film has better solar cell output performance with a PCE of 1.6%, FF of 54% and V_{oc} of 0.803 V when compared SWCNTs (PCE of 1.1%) and PEDOT:PSS (1.0%) alone. It was explained that by the introduction of PEDOT:PSS, the micropores of randomly oriented SWCNTs film is filled thereby forming continuous contact with underneath a-Si:H (Figure 5d). Although the FF and V_{oc} was improved when compared to all the previous reported SWCNT/a-Si:H devices, the J_{sc} was lower, owing to the increased absorption of incident photons in the p-type SWCNTs-PEDOT:PSS layer. These results suggest that we should choose the SWCNT films and optimize the SWCNTs-PEDOT:PSS composite. Following this, we reported a SWCNTs/a-Si:H heterojunction solar cell with a much improved PCE of 2.7% by optimizing the thickness of SWCNTs film in the SWCNTs-PEDOT:PSS composite used as p-type layer and transparent electrode (Figure 5c)[59]. The fabricated devices showed increased PCEs of 3.4% and V_{oc} of 0.9 V with incorporation of PMMA as an anti-reflection layer on top of the SWCNTs-PEDOT:PSS composite (Figure 5c). Moreover, a decrease in the sheet resistance of the SWCNT-PEDOT:PSS (composite) film and an increase in its work function was measured compared to the pristine SWCNT film. This can be attributed, for the fact that every single carbon atom are on the surface exposed to the environment. Therefore, any atom/molecule put on a SWCNT cause changes in their electronic structure and charge transfer between the atom/molecule and a nanotube. Therefore, when PEDOT:PSS is injected it filled micropores in the SWCNT film and, that the holes in the PEDOT:PSS patches can transfer to the interconnected SWCNT network consequently, doping the SWCNTs[24,90,91]. Although, a significant progress had been made in SWCNTs/a-Si:H heterojunction solar cell from initial PCE of less than 1% to 3.4%, yet this was very low and beyond the scope for practical applications. The challenge was to overcome the problems at the SWCNTs and a-Si:H interface, improve the p-type transparent electrode, and thereby improve the overall solar cell performance. The significant problems as indicated in the previous works was the large interface resistance, high Schottky barrier leading to band-offsets between a-Si:H and SWCNTs, and high series resistance of SWCNTs resulting in high carrier recombination.

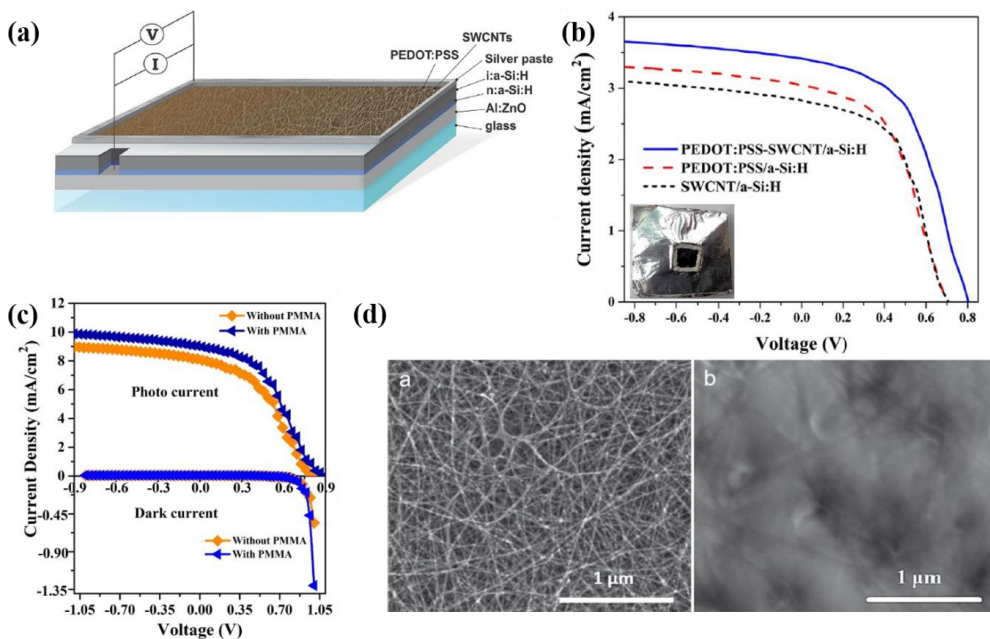


Figure 5. (a) Fabricated PEDOT:PSS-SWCNT/a-Si:H solar cell; (b) photo J–V characteristics of PEDOT:PSS-SWCNT/a-Si:H, PEDOT:PSS/a-Si:H and SWCNT/a-Si:H hybrid solar cells, with inset of a fabricated PEDOT:PSS-CNT/a-Si hybrid solar cell[58]. Reprinted (adapted) with permission from (PHYS. STATUS SOLIDI B 2018, 255, 1700557) with LICENSE NUMBER 4791281444516. Copyright (2017) WILEY - VCH Verlag GmbH & Co. KGaA, Weinheim.; (c) Characteristics of HSCs fabricated with 20 nm thick SWCNTs film sample: J–V curve comparison without Polymethylmethacrylate (PMMA) and with PMMA for photo and dark current response; and (d) Morphological SEM image of: (a) the randomly oriented pristine SWCNT films; (b) uniformly-coated composite film (PEDOT: PSS-SWCNT film[59]. Reprinted (adapted) with permission from (NANOTECHNOLOGY 29 (2018) 105404 (10PP)) with LICENSE ID 1023449-1. Copyright (2018) IOP Publishing Ltd.

2.4 SWCNTs-PEDOT:PSS-SWCNT fibers as novel transparent electrode

To solve the problems mentioned in the previous section, we proposed a rational design of a novel p-type transparent conductor developed using a multicomponent composite that combines the superior properties of SWCNTs with PEDOT:PSS, MoO₃ and SWCNT fibers into a single composite (Figure 6a)[25]. Various configurations were developed and examined as a p-type window layer and electrode in a-Si:H solar cells. A configuration of SWCNTs-

MoO₃-PEDOT:PSS/SWCNT fibers composite (p-type) measured a record equivalent sheet resistance (R_{sh}) of 17 Ω /sq with a transmittance of 90% at 550 nm[25,92]. Moreover, the developed p-type composite displayed a high degree of mechanical flexibility with $\leq 5\%$ change in resistance (Figure 6b). The solar cells made from the developed p-type composite electrode on a-Si:H absorber yielded an outstanding J_{sc} of 15.03 mA/cm² and record PCE up to 8.8% for SWCNTs/a-Si:H heterojunction solar cells (Figure 6c) which was an effective 18% improvement over a standard n-i-p configured solar cell (Figure 6d). Moreover, SWCNT fibers by itself can be used as replacement for traditional metal contacts due to its high conductivity and simple deposition process[25].

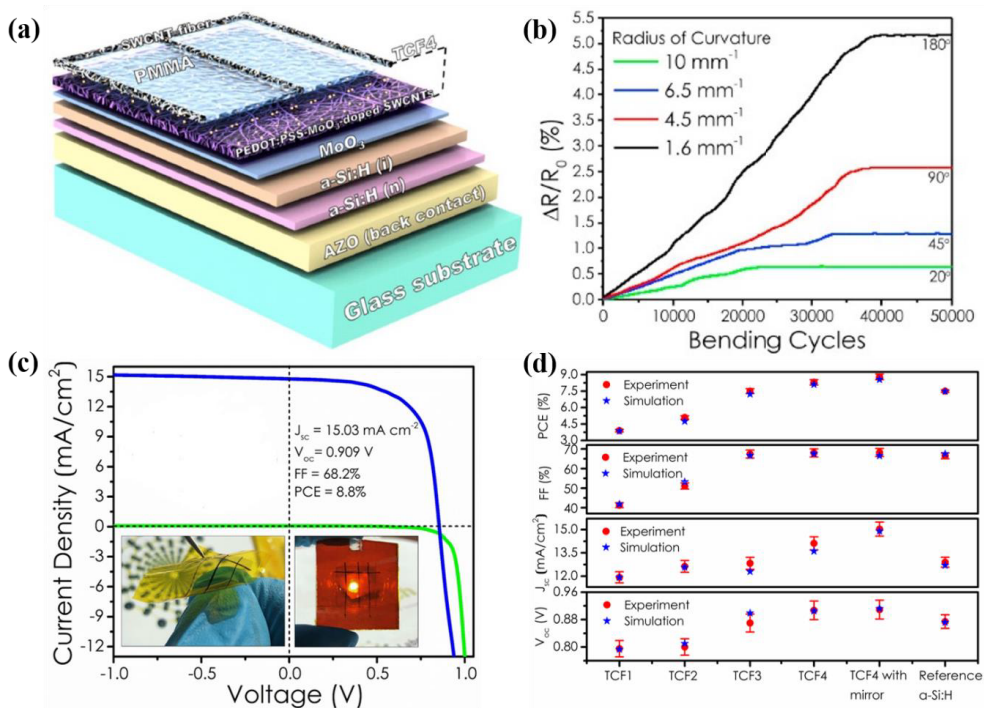


Figure 6. (a) Schematic of the device architecture with optimized TCF (SWCNTs-MoO₃-PEDOT:PSS/SWCNT fibers composite) as p-type window layer and front contact; (b) TCF resistance change during 50 000 bending cycles at angles of 20°, 45°, 90° and 180° with the radii of curvature from 10 to 1.6 in mm⁻¹; (c) J-V characteristics of TCF solar cell (inset shows (bottom-left) a photograph of TCF on a polyimide substrate, and (bottom-right) photograph of the fabricated solar cell on a-Si using developed TCF showing its transparency); and (d) comparison of J-V parameters of standard n-i-p configured a-Si:H solar cel with fabricated

solar cells using different TCFs[25]. Reproduced (adapted) with permission from (NANO ENERGY 2020, 67, 104183) with LICENSE NUMBER 4791271297717. Copyright (2020) Elsevier Ltd.

Solar cells based on SWCNTs as p-type transparent electrodes in a-Si:H have been studied to substitute standard p-type a-Si:H, transparent conductive oxide such as ITO and FTO, and front metal contacts. The PCEs on rigid structures have progressed steadily from 0.03% up to 8.80% as tabulated in Table 1. Moreover, the mechanical properties of SWCNTs and well-established a-Si:H are promising for future low-cost flexible and wearable solar cells.

Table 1. Reported SWCNTs/a-Si:H heterojunction solar cells.

Device	J_{sc} (mA/cm ²)	V_{oc} (V)	FF (%)	PCE (%)	SWCNTs treatment	a-Si treatment	Structures	Remarks	References
1	0.25	0.39	20.0	0.02	NA	NA	Buckypaper/a-Si:H (i)/ITO	First application of CNTs in a-Si solar cells.	[55]
2	0.30	0.50	19.0	0.03	NA	NA	Ag/SWCNT/a- Si:H(i)/a-Si:H(n)/Cr	SWCNTs transferred on a-Si.	[56]
3	6.47	0.68	34.0	1.46	NA	NA	SWCNTs/a-Si:H(i)/a- Si:H(n)/FTO	SWCNTs used as p-type electrodes in nip solar cell.	[75]
4	12.20	0.77	57.0	5.27	triethyloxonium hexachloroantimonate (OA) mixed with dichloroethane.	NA	SWCNTs/Au nanodots/a-Si:H(p)/a- Si:H(i)/a- Si:H(n)/Al:ZnO/Ag	SWCNTs are p-doped with triethyloxonium hexachloroantimonate (OA) mixed with dichloroethane and Au nanodots at SWCNTs and a-Si:H (p) interface.	[64]
5	11.02	0.48	29.0	1.51	SOCl ₂	HF	Ag/SWCNTs/a- Si:H(i)/a-Si:H(n)/Al	Dry transfer of SWCNTs film synthesized by aerosol CVD.	[57]
6	3.56	0.80	54.0	1.57	NA	HF	Ag paste/PEDOT:PSS- SWCNTs/a-Si:H(i)/a- Si:H(n)/Al:ZnO	PEDOT:PSS-SWCNTs as p-type composite.	[58]
7	8.99	0.90	41.8	3.40	NA	HF	PMMA/PEDOT:PSS- SWCNTs/a-Si:H(i)/a- Si:H(n)/Al:ZnO	PMMA as anti- reflection layer.	[59]
8	15.03	0.91	68.2	8.80	HAuCl ₄	HF	SWCNT fibers/PEDOT:PSS- MoO ₃ -SWCNTs/a- Si:H(i)/a- Si:H(n)/Al:ZnO	HAuCl ₄ doping of SWCNTs film and fibers.	[25]

3. Conclusions

Here the recent success in the application of SWCNTs in a-Si:H heterojunction solar cells has been reviewed. The unique structure and extraordinary opto-electrical properties of SWCNTs give them notable advantages for photovoltaic applications, and therefore the future direction is undoubtedly SWCNTs based p-type transparent electrodes. Notable progress has been made on the SWCNTs/a-Si:H heterojunction-based devices, however challenges remain in their practical use. For example, the working mechanism of SWCNTs in solar cells has not been fully clarified due to the statistical presence of both semiconducting and metallic nanotubes in a thin film. Also, the performance of SWCNTs based solar cells is determined by the structure and properties of SWCNTs, such as chirality, sheet resistance, and work function. For this, either pure semiconducting or metallic SWCNTs with high purity and quality are needed to fully understand the mechanism.

The fabrication and characterization of SWCNTs based solar cells has been limited to small active area. Large area solar cells are a big challenge. For large area fabrication and performance of SWCNTs based solar cells, a SWCNT film with high transparency and low sheet resistance is desired. Although, significant progress has been made in lowering the sheet resistance at a transmittance of 90% of pristine SWCNTs film, much needs to be done to replace ITO. One of the possible ways is to reduce the inter-tube junction resistance in the most commonly used randomly oriented SWCNTs film that is much higher than the intrinsic tube resistance and the electrical conductivity of SWCNTs film[93,94]. Recently, carbon-welding on tube-tube junction was proposed to convert inter-tube Schottky contacts into near-ohmic ones[95]. To further reduce the inter-tube junction resistance, SWCNT arrays or aligned SWCNTs is another alternative as previously shown in Si solar cells, but mainly with multi-walled nanotubes[96,97]. As SWCNTs have superior properties, an ideal case would be to make high quality aligned SWCNTs, whose opto-electrical properties are optimized. On the other hand, front contact fingers should be introduced in SWCNTs based solar cells, which can significantly enhance the FF. SWCNT strips/fibers have been used as front contacts, when the PCE increased to 6.52% from initial 3.97%[26]. More recently, our group used SWCNT fibers to increase the overall conductivity of SWCNTs as p-type transparent electrode, thereby improving the PCE of SWCNT/a-Si:H heterojunction solar cells[25]. Moreover, SWCNT fibers itself can be used to replace traditional metal contacts due to their high conductivity and

simple deposition process. Therefore, this is good way to increase the efficiency of solar cells, and also, reduce the sheet resistance of SWCNTs film.

The work-function of SWCNT films need to be improved for better separation and extraction of photo-generated carriers, i.e. the work-function of carbon nanotubes have to be fine-tuned in such a way that the energy levels match with Si. Moreover, the increased work function can increase the barrier height than can result in improved built-in voltage at the interface, thereby resulting in increased V_{oc} . Therefore, effective p-type doping needs to be found that are stable other than the existing acid based treatments with $SOCl_2$, HNO_3 , chlorosulfonic acid, $AuCl_3$, and $HAuCl_4$, which are unstable. This results in poor stability of the fabricated SWCNTs based solar cells.

The device architecture of SWCNTs/a-Si:H also needs to be further optimized. Only a few reports exists on the interface between SWCNTs as front electrode and Si[69,98,99], but none exists on the interface between Si and back electrode. Therefore, this needs further investigation for SWCNTs/Si and SWCNT/a-Si:H new type heterojunction solar cells.

Finally, flexible solar cells are becoming of high relevance to the development of flexible and wearable devices. SWCNTs have excellent flexibility and can be combined with Si thin films like a-Si:H to fabricate flexible SWCNTs/a-Si:H solar cells, respectively. It is envisaged that the SWCNT films are novel p-type transparent conductors in combination with the use of pure high quality semiconducting or metallic SWCNTs that are aligned with better passivation, improved doping stability of SWCNTs, light trapping schemes and nanostructuring can potentially improve future photovoltaic devices. Nevertheless, the applications of the novel p-type composite material are not limited to solar cells[25]. Rational design and room-temperature processing broaden the horizon for transparent and flexible electrode implementation in diverse applications in other fields of science and technology.

ACKNOWLEDGEMENT

P.M.R. and P.D.L. acknowledge the ASPIRE funded by Jane and Aatos Erkko foundation (project # 700056 T30404), Finland. This work was supported by the Ministry of Science and Higher Education of the Russian Federation (project no. FZSR-2020-0007 in the framework of the state assignment no. 075-03-2020-097/1). AGN acknowledges Russian Foundation for Basic Research (project No 18-29-19169). P.M.R thanks for the partial financial support from EDUFI Fellowship (# TM-19-11028) from Finnish National Agency for Education.

References

- [1] IEA. Renewables Information (2019 edition). IEA Stat 2019.
- [2] Green MA, Hishikawa Y, Dunlop ED, Levi DH, Hohl-Ebinger J, Ho-Baillie AWY. Solar cell efficiency tables (version 51). *Prog Photovoltaics Res Appl* 2018. <https://doi.org/10.1002/pip.2978>.
- [3] Yoshikawa K, Kawasaki H, Yoshida W, Irie T, Konishi K, Nakano K, et al. Silicon heterojunction solar cell with interdigitated back contacts for a photoconversion efficiency over 26%. *Nat Energy* 2017. <https://doi.org/10.1038/nenergy.2017.32>.
- [4] Stuckelberger M, Biron R, Wyrsh N, Haug FJ, Ballif C. Review: Progress in solar cells from hydrogenated amorphous silicon. *Renew Sustain Energy Rev* 2017. <https://doi.org/10.1016/j.rser.2016.11.190>.
- [5] Lewis NS. Toward cost-effective solar energy use. *Science* (80-) 2007. <https://doi.org/10.1126/science.1137014>.
- [6] Shah AV. Thin-film silicon solar cells. 2010. <https://doi.org/10.1201/b16327>.
- [7] Gerling LG, Mahato S, Voz C, Alcubilla R, Puigdollers J. Characterization of transition metal oxide/silicon heterojunctions for solar cell applications. *Appl Sci* 2015. <https://doi.org/10.3390/app5040695>.
- [8] Gerling LG, Mahato S, Morales-Vilches A, Masmijtja G, Ortega P, Voz C, et al. Transition metal oxides as hole-selective contacts in silicon heterojunctions solar cells. *Sol Energy Mater Sol Cells* 2016. <https://doi.org/10.1016/j.solmat.2015.08.028>.
- [9] Holman ZC, Descoeudres A, Barraud L, Fernandez FZ, Seif JP, De Wolf S, et al. Current losses at the front of silicon heterojunction solar cells. *IEEE J Photovoltaics* 2012. <https://doi.org/10.1109/JPHOTOV.2011.2174967>.
- [10] Choi D, Yoon H, Kim KH, Um HD, Seo K. ITO-free carrier-selective contact for crystalline silicon solar cells. *J Mater Chem A* 2019. <https://doi.org/10.1039/c8ta11220g>.
- [11] Han J, Yuan S, Liu L, Qiu X, Gong H, Yang X, et al. Fully indium-free flexible Ag nanowires/ZnO:F composite transparent conductive electrodes with high haze. *J Mater Chem A* 2015. <https://doi.org/10.1039/c4ta05728g>.
- [12] Inagaki M, Radovic LR. Nanocarbons [6]. *Carbon N Y* 2002. [https://doi.org/10.1016/S0008-6223\(02\)00204-X](https://doi.org/10.1016/S0008-6223(02)00204-X).
- [13] Avouris P, Freitag M, Perebeinos V. Carbon-nanotube photonics and optoelectronics. *Nat Photonics* 2008. <https://doi.org/10.1038/nphoton.2008.94>.
- [14] Jariwala D, Sangwan VK, Lauhon LJ, Marks TJ, Hersam MC. Carbon nanomaterials for electronics, optoelectronics, photovoltaics, and sensing. *Chem Soc Rev* 2013. <https://doi.org/10.1039/c2cs35335k>.
- [15] Avouris P, Chen Z, Perebeinos V. Carbon-based electronics. *Nat Nanotechnol* 2007. <https://doi.org/10.1038/nnano.2007.300>.
- [16] Jeon I, Matsuo Y, Maruyama S. Single-Walled Carbon Nanotubes in Solar Cells. *Top Curr Chem* 2018. <https://doi.org/10.1007/s41061-017-0181-0>.
- [17] Jeon I, Xiang R, Shawky A, Matsuo Y, Maruyama S. Single-Walled Carbon Nanotubes in Emerging Solar Cells: Synthesis and Electrode Applications. *Adv Energy Mater* 2019. <https://doi.org/10.1002/aenm.201801312>.
- [18] Proctor JE, Armada DAM, Vijayaraghavan A. An introduction to graphene and carbon nanotubes. 2017. <https://doi.org/10.1201/9781315368191>.
- [19] Iijima S, Ichihashi T. Single-shell carbon nanotubes of 1-nm diameter. *Nature* 1993. <https://doi.org/10.1038/363603a0>.
- [20] Arnold MS, Green AA, Hulvat JF, Stupp SI, Hersam MC. Sorting carbon nanotubes

- by electronic structure using density differentiation. *Nat Nanotechnol* 2006. <https://doi.org/10.1038/nnano.2006.52>.
- [21] Carbon nanotubes: Advanced topics in the synthesis, structure, properties and applications. *Mater Today* 2008. [https://doi.org/10.1016/s1369-7021\(08\)70021-x](https://doi.org/10.1016/s1369-7021(08)70021-x).
- [22] Saito R, Dresselhaus G, Dresselhaus MS. *Physical Properties of Carbon Nanotubes*. 1998. <https://doi.org/10.1142/p080>.
- [23] Wang F, Kozawa D, Miyauchi Y, Hiraoka K, Mouri S, Ohno Y, et al. Considerably improved photovoltaic performance of carbon nanotube-based solar cells using metal oxide layers. *Nat Commun* 2015. <https://doi.org/10.1038/ncomms7305>.
- [24] Fan Q, Zhang Q, Zhou W, Xia X, Yang F, Zhang N, et al. Novel approach to enhance efficiency of hybrid silicon-based solar cells via synergistic effects of polymer and carbon nanotube composite film. *Nano Energy* 2017. <https://doi.org/10.1016/j.nanoen.2017.02.003>.
- [25] Rajanna PM, Meddeb H, Sergeev O, Tsapenko AP, Bereznev S, Vehse M, et al. Rational design of highly efficient flexible and transparent p-type composite electrode based on single-walled carbon nanotubes. *Nano Energy* 2019. <https://doi.org/10.1016/j.nanoen.2019.104183>.
- [26] Xu W, Wu S, Li X, Zou M, Yang L, Zhang Z, et al. High-Efficiency Large-Area Carbon Nanotube-Silicon Solar Cells. *Adv Energy Mater* 2016. <https://doi.org/10.1002/aenm.201600095>.
- [27] Tune DD, Mallik N, Fornasier H, Flavel BS. Breakthrough Carbon Nanotube–Silicon Heterojunction Solar Cells. *Adv Energy Mater* 2020. <https://doi.org/10.1002/aenm.201903261>.
- [28] Qian Y, Jeon I, Ho YL, Lee C, Jeong S, Delacou C, et al. Multifunctional Effect of p-Doping, Antireflection, and Encapsulation by Polymeric Acid for High Efficiency and Stable Carbon Nanotube-Based Silicon Solar Cells. *Adv Energy Mater* 2020. <https://doi.org/10.1002/aenm.201902389>.
- [29] Bindl DJ, Safron NS, Arnold MS. Dissociating excitons photogenerated in semiconducting carbon nanotubes at polymeric photovoltaic heterojunction interfaces. *ACS Nano* 2010. <https://doi.org/10.1021/nn1012397>.
- [30] Arnold MS, Zimmerman JD, Renshaw CK, Xu X, Lunt RR, Austin CM, et al. Broad spectral response using carbon nanotube/organic semiconductor/C 60 photodetectors. *Nano Lett* 2009. <https://doi.org/10.1021/nl901637u>.
- [31] Bindl DJ, Wu MY, Prehn FC, Arnold MS. Efficiently harvesting excitons from electronic type-controlled semiconducting carbon nanotube films. *Nano Lett* 2011. <https://doi.org/10.1021/nl1031343>.
- [32] Ramuz MP, Vosgueritchian M, Wei P, Wang C, Gao Y, Wu Y, et al. Evaluation of solution-processable carbon-based electrodes for all-carbon solar cells. *ACS Nano* 2012. <https://doi.org/10.1021/nn304410w>.
- [33] Wang H, Koleilat GI, Liu P, Jiménez-Osés G, Lai YC, Vosgueritchian M, et al. High-yield sorting of small-diameter carbon nanotubes for solar cells and transistors. *ACS Nano* 2014. <https://doi.org/10.1021/nn406256y>.
- [34] Wu Z, Chen Z, Du X, Logan JM, Sippel J, Nikolou M, et al. Transparent, conductive carbon nanotube films. *Science* (80-) 2004. <https://doi.org/10.1126/science.1101243>.
- [35] Lee YH, Kim SG, Tománek D. Catalytic growth of single-wall carbon nanotubes: An Ab initio study. *Phys Rev Lett* 1997. <https://doi.org/10.1103/PhysRevLett.78.2393>.
- [36] Barnes TM, Wu X, Zhou J, Duda A, Van De Lagemaat J, Coutts TJ, et al. Single-wall carbon nanotube networks as a transparent back contact in CdTe solar cells. *Appl Phys Lett* 2007. <https://doi.org/10.1063/1.2748078>.
- [37] Tune DD, Flavel BS, Krupke R, Shapter JG. Carbon nanotube-silicon solar cells. *Adv*

- Energy Mater 2012. <https://doi.org/10.1002/aenm.201200249>.
- [38] Tune DD, Flavel BS. Advances in Carbon Nanotube–Silicon Heterojunction Solar Cells. *Adv Energy Mater* 2018. <https://doi.org/10.1002/aenm.201703241>.
- [39] Jung Y, Li X, Rajan NK, Taylor AD, Reed MA. Record high efficiency single-walled carbon nanotube/silicon p - N junction solar cells. *Nano Lett* 2013. <https://doi.org/10.1021/nl3035652>.
- [40] Ellmer K. Past achievements and future challenges in the development of optically transparent electrodes. *Nat Photonics* 2012. <https://doi.org/10.1038/nphoton.2012.282>.
- [41] Aitola K, Kaskela A, Halme J, Ruiz V, Nasibulin AG, Kauppinen EI, et al. Single-Walled Carbon Nanotube Thin-Film Counter Electrodes for Indium Tin Oxide-Free Plastic Dye Solar Cells. *J Electrochem Soc* 2010. <https://doi.org/10.1149/1.3500367>.
- [42] Lee JM, Lim J, Lee N, Park H II, Lee KE, Jeon T, et al. Synergistic concurrent enhancement of charge generation, dissociation, and transport in organic solar cells with plasmonic metal-carbon nanotube hybrids. *Adv Mater* 2015. <https://doi.org/10.1002/adma.201404248>.
- [43] Lee JM, Park JS, Lee SH, Kim H, Yoo S, Kim SO. Selective electron- or hole-transport enhancement in bulk-heterojunction organic solar cells with N- or B-doped carbon nanotubes. *Adv Mater* 2011. <https://doi.org/10.1002/adma.201003296>.
- [44] Ahn N, Jeon I, Yoon J, Kauppinen EI, Matsuo Y, Maruyama S, et al. Carbon-sandwiched perovskite solar cell. *J Mater Chem A* 2018. <https://doi.org/10.1039/c7ta09174e>.
- [45] Seo S, Jeon I, Xiang R, Lee C, Zhang H, Tanaka T, et al. Semiconducting carbon nanotubes as crystal growth templates and grain bridges in perovskite solar cells. *J Mater Chem A* 2019. <https://doi.org/10.1039/c9ta02629k>.
- [46] Ihly R, Dowgiallo AM, Yang M, Schulz P, Stanton NJ, Reid OG, et al. Efficient charge extraction and slow recombination in organic-inorganic perovskites capped with semiconducting single-walled carbon nanotubes. *Energy Environ Sci* 2016. <https://doi.org/10.1039/c5ee03806e>.
- [47] Zhang Y, Tan L, Fu Q, Chen L, Ji T, Hu X, et al. Enhancing the grain size of organic halide perovskites by sulfonate-carbon nanotube incorporation in high performance perovskite solar cells. *Chem Commun* 2016. <https://doi.org/10.1039/c6cc00268d>.
- [48] Aitola K, Sveinbjörnsson K, Correa-Baena JP, Kaskela A, Abate A, Tian Y, et al. Carbon nanotube-based hybrid hole-transporting material and selective contact for high efficiency perovskite solar cells. *Energy Environ Sci* 2016. <https://doi.org/10.1039/c5ee03394b>.
- [49] Nasibulin AG, Kaskela A, Mustonen K, Anisimov AS, Ruiz V, Kivistö S, et al. Multifunctional free-standing single-walled carbon nanotube films. *ACS Nano* 2011. <https://doi.org/10.1021/nn200338r>.
- [50] Cui K, Anisimov AS, Chiba T, Fujii S, Kataura H, Nasibulin AG, et al. Air-stable high-efficiency solar cells with dry-transferred single-walled carbon nanotube films. *J Mater Chem A* 2014. <https://doi.org/10.1039/c4ta01353k>.
- [51] Shi E, Zhang L, Li Z, Li P, Shang Y, Jia Y, et al. TiO₂-coated carbon nanotube-silicon solar cells with efficiency of 15%. *Sci Rep* 2012. <https://doi.org/10.1038/srep00884>.
- [52] Jia Y, Wei J, Wang K, Cao A, Shu Q, Gui X, et al. Nanotube-silicon heterojunction solar cells. *Adv Mater* 2008. <https://doi.org/10.1002/adma.200801810>.
- [53] Hu X, Hou P, Liu C, Cheng H. Carbon nanotube/silicon heterojunctions for photovoltaic applications. *Nano Mater Sci* 2019. <https://doi.org/10.1016/j.nanoms.2019.03.001>.
- [54] Li X, Lv Z, Zhu H. Carbon/Silicon Heterojunction Solar Cells: State of the Art and Prospects. *Adv Mater* 2015. <https://doi.org/10.1002/adma.201502999>.

- [55] Schriver M, Regan W, Loster M, Zettl A. Carbon nanostructure-aSi:H photovoltaic cells with high open-circuit voltage fabricated without dopants. *Solid State Commun* 2010;150:561–3. <https://doi.org/10.1016/j.ssc.2010.01.013>.
- [56] Del Gobbo S, Castrucci P, Scarselli M, Camilli L, De Crescenzi M, Mariucci L, et al. Carbon nanotube semitransparent electrodes for amorphous silicon based photovoltaic devices. *Appl Phys Lett* 2011;98:1–4. <https://doi.org/10.1063/1.3588352>.
- [57] Funde AM, Nasibulin AG, Syed HG, Anisimov AS, Tsapenko A, Lund P, et al. Carbon nanotube-amorphous silicon hybrid solar cell with improved conversion efficiency. *Nanotechnology* 2016. <https://doi.org/10.1088/0957-4484/27/18/185401>.
- [58] Alekseeva AK, Rajanna PM, Anisimov AS, Sergeev O, Bereznev S, Nasibulin AG. Synergistic Effect of Single-Walled Carbon Nanotubes and PEDOT:PSS in Thin Film Amorphous Silicon Hybrid Solar Cell. *Phys Status Solidi Basic Res* 2018;255. <https://doi.org/10.1002/pssb.201700557>.
- [59] Rajanna PM, Gilshteyn EP, Yagafarov T, Alekseeva AK, Anisimov AS, Neumüller A, et al. Enhanced efficiency of hybrid amorphous silicon solar cells based on single-walled carbon nanotubes and polymer composite thin film. *Nanotechnology* 2018;29. <https://doi.org/10.1088/1361-6528/aaa647>.
- [60] Li Z, Kunets VP, Saini V, Xu Y, Dervishi E, Salamo GJ, et al. Light-harvesting using high density p-type single wall carbon nanotube/n-type silicon heterojunctions. *ACS Nano* 2009. <https://doi.org/10.1021/nn900197h>.
- [61] Kozawa D, Hiraoka K, Miyauchi Y, Mouri S, Matsuda K. Analysis of the photovoltaic properties of single-walled carbon nanotube/silicon heterojunction solar cells. *Appl Phys Express* 2012. <https://doi.org/10.1143/APEX.5.042304>.
- [62] Schropp REI, Zeman M. Amorphous and Microcrystalline Silicon Solar Cells: Modeling, Materials and Device Technology. 1998. <https://doi.org/10.1007/978-1-4615-5631-2>.
- [63] Street RA. Hydrogenated Amorphous Silicon. 1991. <https://doi.org/10.1017/cbo9780511525247>.
- [64] Kim J, Hong AJ, Chandra B, Tulevski GS, Sadana DK. Engineering of contact resistance between transparent single-walled carbon nanotube films and a-Si:H single junction solar cells by gold nanodots. *Adv Mater* 2012. <https://doi.org/10.1002/adma.201104677>.
- [65] Zhou H, Colli A, Butler T, Rupesinghe N, Mumtaz A, Amaratunga G, et al. Carbon nanotube arrays for optical design of amorphous silicon solar cells. *Int J Mater Form* 2008. <https://doi.org/10.1007/s12289-008-0368-6>.
- [66] Zhou H, Colli A, Ahnood A, Yang Y, Rupesinghe N, Butler T, et al. Arrays of parallel connected coaxial multiwall-carbonnanotube-amorphous- silicon solar cells. *Adv Mater* 2009. <https://doi.org/10.1002/adma.200901094>.
- [67] Tu WC, Chang YT, Wang HP, Yang CH, Huang CT, He JH, et al. Improved light scattering and surface plasmon tuning in amorphous silicon solar cells by double-walled carbon nanotubes. *Sol Energy Mater Sol Cells* 2012. <https://doi.org/10.1016/j.solmat.2012.01.038>.
- [68] Zhou H, Tao F, Hiralal P, Ahnood A, Unalan HE, Nathan A, et al. Periodic Nanopillar N-I-P Amorphous Si Photovoltaic Cells Using Carbon Nanotube Scaffolds. *IEEE Trans Nanotechnol* 2014. <https://doi.org/10.1109/TNANO.2014.2343256>.
- [69] Jia Y, Cao A, Kang F, Li P, Gui X, Zhang L, et al. Strong and reversible modulation of carbon nanotube-silicon heterojunction solar cells by an interfacial oxide layer. *Phys Chem Chem Phys* 2012. <https://doi.org/10.1039/c2cp23639g>.
- [70] Jia Y, Li P, Gui X, Wei J, Wang K, Zhu H, et al. Encapsulated carbon nanotube-oxide-silicon solar cells with stable 10% efficiency. *Appl Phys Lett* 2011.

- <https://doi.org/10.1063/1.3573829>.
- [71] Li X, Jung Y, Sakimoto K, Goh TH, Reed MA, Taylor AD. Improved efficiency of smooth and aligned single walled carbon nanotube/silicon hybrid solar cells. *Energy Environ Sci* 2013. <https://doi.org/10.1039/c2ee23716d>.
- [72] Xu W, Deng B, Shi E, Wu S, Zou M, Yang L, et al. Comparison of Nanocarbon-Silicon Solar Cells with Nanotube-Si or Graphene-Si Contact. *ACS Appl Mater Interfaces* 2015. <https://doi.org/10.1021/acsami.5b03699>.
- [73] Yu L, Grace T, Jazi MD, Shearer C, Shapter J. Optimization of the Metal Front Contact Design for Single-Walled Carbon Nanotube-Silicon Heterojunction Solar Cells. *Sol RRL* 2017. <https://doi.org/10.1002/solr.201600026>.
- [74] De Nicola F, Salvato M, Cirillo C, Crivellari M, Boscardin M, Passacantando M, et al. 100% internal quantum efficiency in polychiral single-walled carbon nanotube bulk heterojunction/silicon solar cells. *Carbon N Y* 2017. <https://doi.org/10.1016/j.carbon.2016.12.050>.
- [75] Khanal RR, Philips AB, Huang Z, Dahal LR, Podraza NJ, Collins RW, et al. Single wall carbon nanotube electrodes for hydrogenated amorphous silicon solar cells. *Conf. Rec. IEEE Photovolt. Spec. Conf.*, 2012. <https://doi.org/10.1109/PVSC.2012.6317568>.
- [76] Li Z, Kunets VP, Saini V, Xu Y, Dervishi E, Salamo GJ, et al. SOC12 enhanced photovoltaic conversion of single wall carbon nanotube/ n -silicon heterojunctions. *Appl Phys Lett* 2008. <https://doi.org/10.1063/1.3050465>.
- [77] Blackburn JL, Barnes TM, Beard MC, Kim YH, Tenent RC, McDonald TJ, et al. Transparent conductive single-walled carbon nanotube networks with precisely tunable ratios of semiconducting and metallic nanotubes. *ACS Nano* 2008. <https://doi.org/10.1021/nn800200d>.
- [78] Li W, Li Y, Sheng M, Cui S, Wang Z, Zhang X, et al. Enhanced Adhesion of Carbon Nanotubes by Dopamine Modification. *Langmuir* 2019. <https://doi.org/10.1021/acs.langmuir.9b00192>.
- [79] Rajanna PP, Luchkin S, Larionov K V., Grebenko A, Popov ZI, Sorokin PB, et al. Adhesion of Single-Walled Carbon Nanotube Thin Films with Different Materials. *J Phys Chem Lett* 2020. <https://doi.org/10.1021/acs.jpcclett.9b03552>.
- [80] Jia Y, Cao A, Bai X, Li Z, Zhang L, Guo N, et al. Achieving high efficiency silicon-carbon nanotube heterojunction solar cells by acid doping. *Nano Lett* 2011. <https://doi.org/10.1021/nl2002632>.
- [81] Singh I, Bhatnagar PK, Mathur PC, Kaur I, Bharadwaj LM, Pandey R. Optical and electrical characterization of conducting polymer-single walled carbon nanotube composite films. *Carbon N Y* 2008. <https://doi.org/10.1016/j.carbon.2008.04.013>.
- [82] Lin H, Li L, Ren J, Cai Z, Qiu L, Yang Z, et al. Conducting polymer composite film incorporated with aligned carbon nanotubes for transparent, flexible and efficient supercapacitor. *Sci Rep* 2013. <https://doi.org/10.1038/srep01353>.
- [83] Fan X, Nie W, Tsai H, Wang N, Huang H, Cheng Y, et al. PEDOT:PSS for Flexible and Stretchable Electronics: Modifications, Strategies, and Applications. *Adv Sci* 2019. <https://doi.org/10.1002/advs.201900813>.
- [84] Kymakis E, Klapsis G, Koudoumas E, Stratakis E, Kornilios N, Vidakis N, et al. Carbon nanotube/PEDOT:PSS electrodes for organic photovoltaics. *EPJ Appl Phys* 2006. <https://doi.org/10.1051/epjap:2006148>.
- [85] Fan B, Mei X, Sun K, Ouyang J. Conducting polymer/carbon nanotube composite as counter electrode of dye-sensitized solar cells. *Appl Phys Lett* 2008. <https://doi.org/10.1063/1.2996270>.
- [86] He J, Gao P, Ling Z, Ding L, Yang Z, Ye J, et al. High-Efficiency Silicon/Organic Heterojunction Solar Cells with Improved Junction Quality and Interface Passivation.

- ACS Nano 2016. <https://doi.org/10.1021/acsnano.6b07511>.
- [87] He J, Gao P, Yang Z, Yu J, Yu W, Zhang Y, et al. Silicon/Organic Hybrid Solar Cells with 16.2% Efficiency and Improved Stability by Formation of Conformal Heterojunction Coating and Moisture-Resistant Capping Layer. *Adv Mater* 2017. <https://doi.org/10.1002/adma.201606321>.
- [88] Thomas JP, Rahman MA, Srivastava S, Kang JS, McGillivray D, Abd-Ellah M, et al. Highly Conducting Hybrid Silver-Nanowire-Embedded Poly(3,4-ethylenedioxythiophene):Poly(styrenesulfonate) for High-Efficiency Planar Silicon/Organic Heterojunction Solar Cells. *ACS Nano* 2018;12:9495–503. <https://doi.org/10.1021/acsnano.8b04848>.
- [89] Liu Y, Zhang J, Wu H, Cui W, Wang R, Ding K, et al. Low-temperature synthesis TiO_x passivation layer for organic-silicon heterojunction solar cell with a high open-circuit voltage. *Nano Energy* 2017. <https://doi.org/10.1016/j.nanoen.2017.02.024>.
- [90] Ki KK, Jung JB, Hyeon KP, Soo MK, Geng HZ, Kyung AP, et al. Fermi level engineering of single-walled carbon nanotubes by AuCl₃ doping. *J Am Chem Soc* 2008. <https://doi.org/10.1021/ja8038689>.
- [91] Kim KK, Yoon SM, Park HK, Shin HJ, Kim SM, Bae JJ, et al. Doping strategy of carbon nanotubes with redox chemistry. *New J Chem* 2010. <https://doi.org/10.1039/c0nj00138d>.
- [92] Kaskela A, Nasibulin AG, Timmermans MY, Aitchison B, Papadimitratos A, Tian Y, et al. Aerosol-synthesized SWCNT networks with tunable conductivity and transparency by a dry transfer technique. *Nano Lett* 2010. <https://doi.org/10.1021/nl101680s>.
- [93] Fuhrer MS, Nygård J, Shih L, Forero M, Yoon YG, Mazzoni MSC, et al. Crossed nanotube junctions. *Science* (80-) 2000. <https://doi.org/10.1126/science.288.5465.494>.
- [94] Nirmalraj PN, Lyons PE, De S, Coleman JN, Boland JJ. Electrical connectivity in single-walled carbon nanotube networks. *Nano Lett* 2009. <https://doi.org/10.1021/nl9020914>.
- [95] Jiang S, Hou PX, Chen ML, Wang BW, Sun DM, Tang DM, et al. Ultrahigh-performance transparent conductive films of carbon-welded isolated single-wall carbon nanotubes. *Sci Adv* 2018. <https://doi.org/10.1126/sciadv.aap9264>.
- [96] Di J, Yong Z, Zheng X, Sun B, Li Q. Aligned carbon nanotubes for high-efficiency Schottky solar cells. *Small* 2013. <https://doi.org/10.1002/sml.201202995>.
- [97] Li R, Li H, Zou J, Zhang X, Li Q. Transport behaviors of photo-carriers across the aligned carbon nanotubes and silicon interface. *Nanoscale* 2014. <https://doi.org/10.1039/c4nr03433c>.
- [98] Yu L, Batmunkh M, Grace T, Dadkhah M, Shearer C, Shapter J. Application of a hole transporting organic interlayer in graphene oxide/single walled carbon nanotube-silicon heterojunction solar cells. *J Mater Chem A* 2017. <https://doi.org/10.1039/c7ta01782k>.
- [99] Tune DD, Flavel BS, Quinton JS, Ellis A V., Shapter JG. Single-walled carbon nanotube/polyaniline/n-silicon solar cells: Fabrication, characterization, and performance measurements. *ChemSusChem* 2013. <https://doi.org/10.1002/cssc.201200600>.

Most of the daily encountered optical and electronic devices constitute of transparent conductors. However, all the present available transparent conductors are n-type semiconductors, thus restricting technological advancement. The emergence of single-walled carbon nanotubes as p-type transparent conductors has been promising. Its further development will tremendously be instrumental for various opto-electronics and energy technologies. This work presents the development of state-of-the-art p-type transparent conductor using thin multicomponent layers and the introduction of carbon nanotube fibers. The newly developed conductor is certainly revolutionary for various single-walled carbon nanotubes application as shown in the fabricated hybrid heterojunction solar cells. This will open new avenues for its application in widespread technologies as in optoelectronics, photonics and energy.



ISBN 978-952-60-3892-6 (printed)

ISBN 978-952-60-3893-3 (pdf)

ISSN 1799-4934 (printed)

ISSN 1799-4942 (pdf)

Aalto University
School of Science
Department of Applied Physics
www.aalto.fi

**BUSINESS +
ECONOMY**

**ART +
DESIGN +
ARCHITECTURE**

**SCIENCE +
TECHNOLOGY**

CROSSOVER

**DOCTORAL
DISSERTATIONS**